UNIVERSIDAD DE VALENCIA
Departamento de Física Aplicada y Electromagnetismo

VNIVERSITAT DE VALÈNCIA

PhD Thesis

Characterization of Magnetic-Plasmonic Compounds by means of Raman Spectroscopy

Defended by María José Recio Carretero
PhD Program Nanociencia y Nanotecnología

Directed by:
Andrés Cantarero Sáez
Josep Canet Ferrer

Valencia, September 2017

Prof. Andrés Cantarero Sáez, Catedrático del Departamento de Física Aplicada de la Universidad de Valencia y Dr. Josep Canet Ferrer del ICFO-Institut de ciéncies Fotòniques (Barcelona Institute of Science and Technology), informan que:

María José Recio Carretero, licenciada en Química, ha realizado en el Instituto de Ciencia Molecular (ICMol) de Valencia, bajo su dirección, el trabajo descrito en la presente Memoria que lleva por título "Characterization of Magnetic-Plasmonic Compounds by means of Raman Spectroscopy" y que presenta para optar al grado de Doctor por la Universidad de Valencia.

Valencia, septiembre de 2017

Fdo. Andrés Cantarero Sáez

Fdo. Josep Canet Ferrer

A mis padres, a Luis y a Rafa

It's a long way to the top
if you wanna rock'n roll
(AC/DC)

Contents

List of Figures

List of Tables

Chapter 1

Introduction

This manuscript discussed the application of Raman spectroscopy [1] as a complementary characterization of new nanomaterials. The advantages come in the one hand from the intrinsic capabilities of the Raman technique, which offer the vibrational signatures of solid and molecular compound, and on the other hand, on the signal increase of those modes via Surface Enhancement Raman Scattering (SERS) spectroscopy. This have been studied in many experiments from different points of view, and at the end, the work described in the next pages would consist of a selection of them. The point is that we focused just in those cases where we believe the Raman characterization really offsets an advantage with respect to other characterization techniques. Then, even the reader can identify different objectives during the characterization of magnetic NPs, magnetic-plasmonic composites, spin crossover compounds, or nanowires; the common point is that all this materials have demanded Raman measurements to complete their characterization. In order to make the manuscript easier to read we have describe the different materials in separated Chapters. In this way we could emphasize on the advantages of Raman spectroscopy for any particular case, and offer a customized introduction in any case.
Fundamentals and experimental techniques of characterization: This chapter consists of a description of the experimental technique employed on the characterization of the samples. Synthesis, structural and magnetic characterization of iron oxide nanoparticles: this Chapter describes the magnetite nanoparticles the synthesis and characterization of the iron oxide NP to be used as a reference in further Chapters of the Thesis. Iron oxide can be found in many phases, including 16 pure oxides (e.g., FeO, Fe_3O_4), 5 polymorphs of FeOOH (e.g., α-FeOOH, γ-FeOOH) and 4 different crystal structures for the Fe_2O_3 (e.g., α-Fe_2O_3, γ-Fe_2O_3). This enables a wide range of properties (optical, electronic and magnetic) with potential application in catalysis, magnetic recording, pigment fabrication, functional coatings, gas sensors, lubrications, and biomedicine (e.g., magnetic resonance imaging, drug delivery and therapy). This rich phenomenology grows up at the nanoscale with the quantum confinement effects and the observation of single domain magnets. In this sense, any improvement in the structural and magnetic

characterization can be considered a valuable advance. Here, we propose Raman spectroscopy as a complementary tool for structural characterization. For example, Raman spectra can clearly distinguish and sometimes quantify the presence of magnetite and maghemite from a heterogeneous. Notice, that this phases are particularly hard to distinguish by the well-established electron diffraction or X-ray diffraction. It also allow identifying the presence of Fe^{2+} or Fe^{3+} atoms in a single crystal. This may offer relevant information to complete magnetic characterization via SQUID. We can point out other advantages, for example, the information can be acquired in few seconds, as a difference to magnetic characterization that might require several hours. Microanalysis methods require tenths of milligrams of material to obtain a worth result; however, by Raman we can easily observe composition from single crystals or NP monolayers. Magnetite combined with gold NPs: In this Chapter we take advantage of our recently acquired experience on magnetite NPs to study hybrid magnetite-gold systems. This is considered a multifunctional platform. On the one hand, gold supports localized surface plasmon resonances and gets on very well with amine/thyol terminal groups. On the other hand, magnetite NPs enables the response in front of external stimuli (micro-frequencies) and allow manipulation via magnetic fields. Many approaches can be found in literature, but we focus on three of them: core-shell, dumbbell-like dimer and cross-linked nanoparticles; Fe@Au, Fe(Au) and Fe-Au respectively. They respectively correspond to the cases of: embedded NPs, NPs in touch or NPs separated a short distance. Affording such different cases we want to offer a complete overview about the possibilities offered by magnetite-gold composites. We focus on the magnetic characterization looking for the possible impact of the gold cluster on the magnetic capabilities of the system. Plasmonic effects are briefly discussed through the description of the electrical field distribution in the gold NP surroundings. This will be enough for the understanding of the Raman measurement. The readers with interest on a deep description of the plasmonic properties are referred to literature. In general we have observed the reduction of the magnetic capabilities in those heterostructures due to the effects plasmonic constituents. This effect is more important in the case of the core-shell system, probably because the magnetic cluster is completely surrounded by the plasmonic shell. As a result, the dumbbell structure is presented as a clear alternative to substitute the core-shell in that applications where the presence of gold could limit the magnetic properties. Finally, comparison with the linked NP pairs offer a complete overview about the phenomena. Importantly, the description of Fe-Au would also apply for larger composites whose magnetic and plasmonic properties can be predicted based in our discussion. Raman spectroscopy for the study of Spin-Crossover in Fe^{2+} complexes: This Chapter describes the Spin-crossover

(SCO) phenomenon and the study of spin crossover nanoparticles of different nature. Few years ago these systems were proposed as switchable molecules where the switching process is induced by external perturbations as a temperature variations, induced pressure or light irradiation. The switching effect is accompanied by changes in the properties of the molecules (magnetism, structural changes, color), therefore applications of this materials as temperature or pressure sensors is straightforward. From the technological point of view, the potential application of SCO materials determines the SCO dynamics. That is, while some complexes exhibit abrupt crossover transitions, other ones present certain thermal (or pressure) hysteresis. Then, the characterization of the spin state results of great interest. The point is that magnetic measurements required are really time consuming and they require huge amounts of material for characterizing any sample. This is an important constraint in a research lab since most times we just can obtain few milligram of product during the development of procedures. This also applies to the SCO systems studied in Chapter 5. They consist of two different families of iron compounds: i) $Fe(Htrz)(trz)(ClO_4)$ and $[Fe(Htrz)_2(NH_2trz)](BF_4)$ ii) $[Fe_3^{3+}(\mu_3\text{-}O)(H_2O)_3[Fe^{2+}(bppCOOH)(bppCOO)]_6(ClO_4)_{13}\cdot((CH_3)_2CO)_6]\cdot$(solvate) complex. From the structural point of view both families have got a common point. As most SCO compounds, the metal-to-ligand bond distance varies considerably when the complex shifts from the High Spin state to the Low Spin state. Of course, this affects the energy of the vibrational modes in the metal surroundings. As a result, Raman spectroscopy can be used to identify the predominant spin state in a given SCO complex, and the spin crossover can be monitored by consecutive acquisition of Raman spectra. As an advantage, this method does not require further sample preparation and it spends minor sample amount as demonstrated by characterization of single crystal and NP monolayers. In further experiments, our Raman set-up might be employed to study SCO systems exposed to external stimuli. Surface-enhanced Raman Scattering in III-V nanowires functionalized by gold nanoparticles: the optical excitation of plasmons can enhance the electrical field near the particle surface. This phenomenon has relevant applications such as surface-enhanced Raman scattering (SERS) [2]. In addition, due to the strong sensitivity of the plasmon resonance, the environment can be exploited for sensing [3]. This explains the wide range of tunable plasmonic nanoparticles that can be found in literature, were the plasmon resonance can be tuned with the available laser light sources [4]. But also because of all the potential applications that the researchers are continuously developing through the formulation of new NPs. During the stay at the bionanoplasmonics group lead by Prof. Liz-Marzàn in CIC biomaGUNE (Donosti) gold nanostars and nanorods were synthesised. Based in the seed-mediated method, different synthetic routes have been developed to ob-

tain gold nanostars of different sizes, characterizing the resulting materials and proposing functionalization strategies for improving bio-compatibility [5]. From the optical point of view the nanostars are highly anisotropic and strongly dependent on the size of the protruding star-tips, as required for SERS applications. For this reason, we paid attention to this particular system, in our case to be applied on characterization solid state systems. On the one hand semiconductor nanowires results on an interesting system for fundamental study. Nowadays technology allow the growth of defect-free nanowires with very low doping level (if desired) and controlled surface states. On the other hand, strong carrier confinement and high surface-to-volume ratio (in comparison to thin films) enables a rich phenomenology with quite particular exciton dynamics. In this sense, comparison between bulk and nanostructured materials results of fundamental interest. In this way, Raman spectroscopy results essential, since this technique offers information about the crystal quality, orientation, composition and strain [6]. The functionalization of semiconductor nanowires with nanostars have been relatively easy, given the previous effort of researchers on the functionalization of other surfaces. Here we are going to demonstrate the potential of nanostars for the characterization of semiconductors, since we can easy observe weak Raman peaks via SERS. But notice that these would be preliminary results. In further experiments we will work on the optimization of the procedures to improve the reproducibility of the results.

Bibliography

[1] Raman, C.V. *A new radiation.* Indian J. Phys., 2 387, (1928).

[2] Schatz, G.C. and van Duyne, R. P. *Electromagnetic mechanism of surface-enhanced spectroscopy. In Handbook of Vibrational Spectroscopy.* Chalmers, J.M., Griffiths, P.R., Eds., John Wiley: Chichester, 2002,1-16, (2002).

[3] Sun, Y. and Xia, Y. *Increased Sensitivity of Surface Plasmon Resonance of Gold Nanoshells Compared to That of Gold Solid Colloids in Response to Environmental Changes.* Anal. Chem., 2002, 74, 5297-5305, (2002).

[4] Murphy, C.J., Sau, T.K.,Gole,A. M., Orendorff, C.J., Gao, J., Gou, L., Hunyadi, S.E. and Li, T. *Anisotropic Metal Nanoparticles: Synthesis, Assembly, and Optical Applications.* J. Phys. Chem. B 109(29), 13857-13870, (2005).

[5] Nehl, C. L., Liao, H. and Hafner, J. H. *Optical Properties of Star-Shaped Gold Nanoparticles.* Nano Lett. 6, 683-688, (2006).

[6] Pauzauskie, P. J. and Yang, P. *Nanowire Photonics.* Materials Today, 9, 36, (2006).

Chapter 2

Fundamentals and experimental section

In this chapter, the different experimental techniques employed to characterize the optical, electronic and magnetic properties of our samples are described. The theoretical background is focused on the light-matter interaction which is key to understand our discussion.

2.1 Raman spectroscopy

Although most of the light travelling through a medium is either transmitted or absorbed following the standard laws of reflection and refraction, a minor fraction is scattered in all directions by inhomogeneities inside the medium. At the inhomogeneities such as dislocations in a crystal scatter the light ellastically, i. e., without frequency change. Inelastic scattering arising from, fluctuations in the density of the medium are associated with atomic vibrations is called Raman scattering [1]. Nowadays, Raman spectroscopy is considered a standard nondestructive contactless characterization technique that allows to investigate the structural, optical and electronic properties of a material. Particularly, the technique is based on the inelastic scattering process of optical phonons during irradiation of materials. Similar techniques originating from the elastic scattering processes and inelastic scattering of acoustic phonons are referred to as *Rayleigh scattering* and *Brillouin scattering*, respectively.

2.1.1 Theoretical aspects

In this section we will first present a macroscopic theory of Raman scattering by phonon in solids. The rest of the Section is a description of the Raman setup used to perform our experiments.
Raman scattering is considered an inelastic process since the "re-emitted" photon changes in energy. However, the energy and the momentum is conserved after

generation or annihilation of phonons. Then, the following energy and quasi-momentum conservation laws hold:

$$\hbar\omega_S = \hbar\omega_L \mp \hbar\omega_p \tag{2.1}$$

giving the energy conservation, and

$$\hbar k_S = \hbar k_L \mp \hbar k_p \tag{2.2}$$

corresponding to the wave number conservation. Here, the indices denominate the scattered (S) and the incident laser (L) light as well as the phonon (p) energy and momentum, respectively. The minus sign stands for those scattering processes in which phonon is generated (*Stokes process*), whereas an annihilation of a phonon is described by the plus sign (*anti-Stokes process*). The two conservation laws state that only a certain combination of energy and momentum can be transferred to the sample. Assuming visible lasers as radiation sources, k_L is in the order of 10^6 cm^{-1}. Hence, for first-order scattering by optical phonons the energy transfer $\hbar\omega_p$ (also referred to as *Raman frequency* or *Raman shift*) is almost independent of the incident energy $\hbar\omega_L$ since the phonon dispersion can be neglected near the center if the Brillouin zone. In this sense, first-order Raman scattering is sensitive to phonons at the Γ point of the Brillouin zone.
In non-linear optics, the Raman scattering is described by means of the polarizability of an infinite medium with electric susceptibility $\chi(\omega_L)$ at laser frequency ω_L. In general, χ is a second order tensor, but for simplicity the medium is assumed to be isotropic such that χ can be represented by a scalar. When a plane electromagnetic wave

$$E(t) = E_L e^{-i\omega_L t} \tag{2.3}$$

exits this medium, a sinusoidal polarization will be induced:

$$P = \chi(\omega_L) E_L e^{-i\omega_L t} \tag{2.4}$$

In general, the characteristic frequencies ω_L, which determine χ, are much larger than ω_p, $\chi(\omega_L)$ can be expanded in power series of the phonon displacement Q. This is known as the quasi-statistic or adiabatic approximation [2]. Assuming a plane wave for $Q(t) = Q_{0e^{i\omega_p t}}$ and keeping only the first order terms, results in

$$\chi(\omega_L, Q(t)) = \chi(\omega_L) + \left(\frac{d\chi(\omega_L)}{dQ}\right) Q(t) \tag{2.5}$$

The first term on the right hand side denotes de susceptibility of the medium with no fluctuations, whereas the second term represents an oscillating susceptibility induced by the lattice wave $Q(t)$. Substituting Eq. 2.5 into Eq. 2.4, the induced polarization can be expressed as

$$P = \chi(\omega_L) E_L e^{-i\omega_L t} + \left(\frac{d\chi(\omega_L)}{dQ}\right) E_L e^{-(i\omega_L \mp \omega_p)t} Q_0 \tag{2.6}$$

In this equation, the first term corresponds to the polarization vibrating in phase with the incident light, i.e. the term is responsible for elastic light scattering. The second term denotes a polarization varying with $(\omega_L \mp \omega_p)t$, an induced oscillation which generates dipole radiation at the Stokes and anti-Stokes frequencies[1].
So far, χ and $d\chi/dQ$ have handled as scalars, but in general they are tensors. If one assumes thar Q is the vector displacement of a given atom induced by the phonon an $\widehat{Q} = Q/|Q|$ is a unit vector parallel to the phonon displacement, then one can define a second rank tensor [2].

$$R = (d\chi/dQ)\widehat{Q} \tag{2.7}$$

Indeed, R is known as the *Raman tensor*. The intensity of the scattered radiation can be calculated from the time-averaged power radiated by the induced polarizations (second term on the right hand side of Eq. 2.6) into the solid angle. This scattered intensity I_S is proportional to [2].

$$I_S \propto \omega_S^4 \left|\widehat{e}_L\right| \widehat{e}_S \tag{2.8}$$

where $\widehat{e}_L$ and $\widehat{e}_S$ denote the polarization of the incident and scattered radiation, respectively. It is worth nothing that Eq. 2.8 the scattered intensity is dependent on the fourth power of ω_S. By measuring the dependence of the scattered intensity on the incident and scattered polarizations, one can deduce the symmetry of the Raman tensor and, hence, the symmetry of the corresponding Raman-active

[1]The expression to higher terms in Eq. 2.5 induces polarizations at higher frequencies giving rise to second order Raman scattering or Raman overtones. Actually, the Stokes terms must be multiplied by a factor $n_p + 1$ and the anti-Stokes by n_p. These factors can only be obtained from a quantum-mechanical treatment of the light scattering process.

phonon. Thus, Raman scattering gives information about the frequency and symmetry of the zone-center phonon modes.

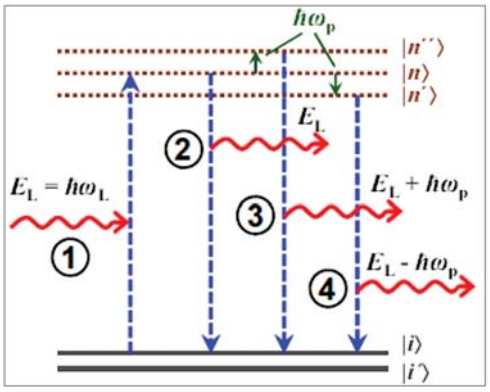

Figure 2.1: Energy level diagram for a Raman process. In a first step (1), the system in the ground state $|i\rangle$ is excited to an intermediate state $|n\rangle$ under absorption of a photon with energy $\hbar\omega_L$. An electron hole pair is generated which recombines (2) with emission of a photon (Rayleigh). In the Raman scattering process the electron-hole pair (1) is scattered to another state $|n''\rangle$ (3) or $|n'\rangle$ (4) under annihilation (Stokes) of a phonon with energy $\hbar\omega_p$. Subsequent recombination from the excited states leads to the emission of the scattered photon. Figure extracted from [3].

The Raman tensor is taken an a symmetric tensor since χ is a symmetric tensor[2]. The symmetry requirement involves that for certain choices of scattering geometries and polarizations, $\widehat{e}_L$ and $\widehat{e}_S$, the scattering radiation vanishes (so-called Raman selection rules).

Raman scattering can be also illustrated by means of a quantum mechanics picture, see Fig. 2.1. The three different steps can be distinguished. Firstly, an incident photon excites the material from the initial state $|i\rangle$ into an intermediate state $|n\rangle$ by creation of an electron-hole pair (1). Secondly, the electron-hole pair is scattered to another state $|n'\rangle$ by generation of a phonon. Finally, the electron-hole pair in the state $|n'\rangle$ recombine radioactively state under emission of the Stokes scattered photon (4). If in the process an electron-hole $(e-h)$ pair gets scattered to the state $|n''\rangle$ by annihilation of a phonon (3), the photon of the scattered light increases its energy the proper the same amount to accomplish the conservation rule is emitted and an anti-Stokes process appears. In the following, only Stokes processes are taken into account[3] for simplicity.

$$(I_S/I_{AS}) = [(\omega_L + \omega_p)/(\omega_L - \omega_p)]^4 e^{-\hbar\omega_p/(k_B T)} \tag{2.9}$$

[2]This is only correct if one can neglect the slight difference in frequency between incident and scattered radiation. Within this aproximation, antisymmetric components in the Raman tensor can be introduced only by magnetic fields [2]. Since most semiconductors are nonmagnetic, one can assume that the Raman tensor is symmetric.

[3]see references for more details

The scattering probability can be calculated with third-order perturbation theory [2]. Here, only the mentioned Raman Stokes process included[4]. The probability $\mathrm{P}_{ph}(\omega)$ for scattering a system from the initial state to the final state can be derived, as usual, via the Fermi Golden Rule and is given by [2].

$$\begin{aligned} P_{ph}[\omega_S] &= \left(\frac{2\pi}{\hbar}\right) \left| \sum_{n,n'} \frac{\langle i|H_{eR}(\omega_L)|n'\rangle \langle n'|H_{eL}(\omega_p)|n\rangle \langle n|H_{eR}(\omega_S)|i\rangle}{[\hbar\omega_L - (E_n - E_i)]\,[\hbar\omega_L - \hbar\omega_p - (E_{n'} - E_i)]} \right|^2 \\ &\times \ \delta\left[\hbar\omega_L - \hbar\omega_p - \hbar\omega_S\right] \end{aligned} \tag{2.10}$$

where H_{eR} and H_{eL} denote the interaction Hamiltonian between electron and photon (radiation) and between electron an phonon (lattice) according to the three steps of Stokes scattering. Other information about the medium, such as the electronic transitions, can be deduced from Eq. 2.10. One way to achieve this is by tuning the incident laser to resonate with a strong electronic interband transition. This is known as *resonant Raman scattering*. If $|a\rangle$ and $|b\rangle$ are real discrete intermediate state with finite lifetime τ_a and τ_b, and transition energies E_a and E_b the Raman scattering probability for a given phonon mode in the vicinity of E_a and E_b can be written as [2],

$$P_{ph}[\omega_S] \approx \left(\frac{2\pi}{\hbar}\right) \left| \frac{\langle i\,|H_{eR}|\,a\rangle \langle a\,|H_{eL}|\,a\rangle \langle a\,|H_{eR}|\,i\rangle}{(E_a - \hbar\omega_L - i\Gamma_a)\,(E_a - \hbar\omega_S - i\Gamma_a)} \right|^2 \tag{2.11}$$

where $\Gamma_a(\Gamma_b)$ is the energy broadening related to the lifetime transition $\tau_a(\Gamma_b)$ by $\Gamma_a = \hbar/\tau_a(\Gamma_b = \hbar/\tau_b)$. Thus, a resonance enhancement can be observed when the incident ($\hbar\omega_L$) or scattered light energy ($\hbar\omega_S$) is close to E_a. In the case of a double resonance where the incident and scattered light are in resonance with different transitions, both denominators are small simultaneously leading to a strong enhancement to the Raman intensity. When $\hbar\omega_L = E_a$ coincides with an electronic transition, we have *incoming resonance* while if $\hbar\omega_S = E_a$ comes from an electronic transition we say that we have *outgoing resonance*.

2.1.2 Experimental set up

The common problems of Raman detection are the low intensity of the Raman scattering and the presence of the brighter Rayleight signal very close in energy.

[4]Further Raman processes, usually ilustrated by Feynman diagrams, leading to the same final state, are not taken into account and can be found elsewhere [2].

The first problem can be resolved by using lasers which can provide monochromatic light of high intensities, whereas in the second case double or triple monochromator or Notch/Edge filters can be used to separate the strong Rayleigh scattered light from the relatively weak Raman signal. In that case, working in the backscattering configuration results very convenient in non transparent samples, see Fig. 2.2. In our set-up the scattered light was dispersed by a Jobin Yvon T64000 spectrometer and detected with a liquid-nitrogen-cooled charge coupled device (CCD), JVC model TK-C701EG, which is used for localizing visually the lase spot on the sample surface. Different objectives can be used, 100×, 50×, 20×, 10×, 5×, some of them working with long working distance (LWD). The backscattered light is collected again by the same objective and driven to the input slit of the spectrometer. After dispersion, the light is detected by a CCD camera Jovin Yvon model CCD-3000V refrigerated by liquid nitrogen. The monochromator slit is arranged so that the system has a spectral resolution around 1.0 cm^{-1}.

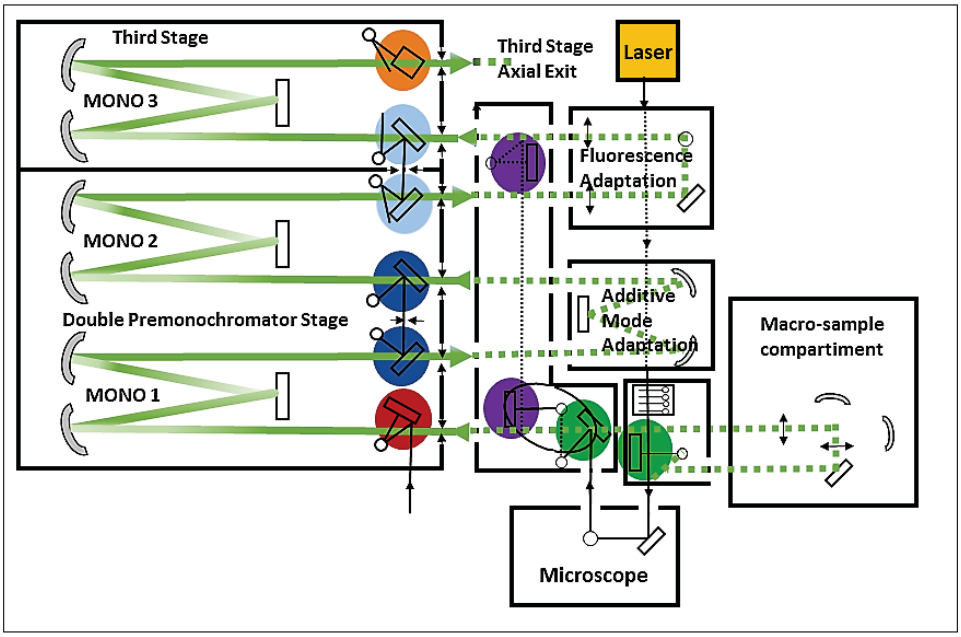

Figure 2.2: Schematic experimental of a triple stage Raman spectrometer Horiba T64000 (adapted from Horiba).

2.2 Transmission electron microscopy (TEM)

TEM is a microscopy technique that uses a beam of electrons which is shone through a specimen to form an image. Operating on the same basic principles as

the light microscope, the transmission electron microscope (TEM) uses electrons instead of light. Since TEM uses electrons their much lower wavelength makes it possible to get great resolution, thousand times better than with a light microscope [4].
Basically, a high energy beam of electrons is transmitted through a very thin sample, and the interactions between the electrons and the atoms can be used to observe several features such as the crystal structure and features in the structure (like dislocations and grain boundaries). Chemical analysis can also be done by means of electron diffraction techniques. TEM can be used to study the growth of layers, their composition and defects in semiconductors. High resolution can be used to analyze the quality, shape, size and density of quantum wells, wires and dots.

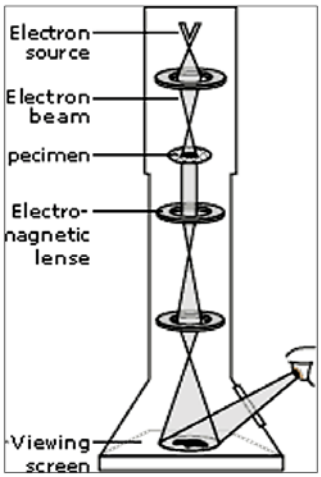

Figure 2.3: Schematic of TEM microscopy. Figure extracted from [5].

In Fig. 2.3 the most important sections of TEM are described:

- Illumination system. It transfers electrons from the gun to the specimen giving either a broad beam or a focused beam. In the ray-diagram, the parts above the specimen belong to illumination system.
- The objective lens and stage. This combination is the most important part of TEM.
- The TEM imaging system. Physically, it includes the intermediate lens and projector lens.

The diffraction pattern and image are formed at the back focus plane and image plane of the objective lens. If we take the back focus plane as the objective plane of

the intermediate lens and projector lens, we will obtain the diffraction pattern on the screen. It is usually said that the TEM works in diffraction mode. If we take the image plane of the objective lens as the objective plane of the intermediate lens and projector lens, we will form image on the screen. This is an image of the reciprocal lattice of the solid, which can be Fourier transformed to an image in the real space.

2.3 Scanning electron microscope (SEM)

The operation scheme is depicted in Fig. 2.4.

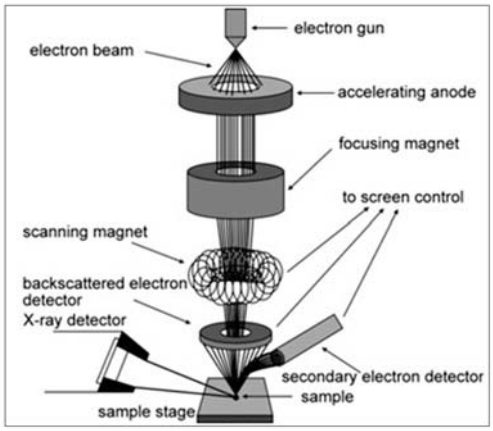

Figure 2.4: Schematic of SEM microscopy. Figure extracted from [6].

Primary electrons are focused into a small-diameter electron probe that is scanned across the specimen by means of electron lenses. These lenses are able to control the beam by means of electromagnetic fields, which applied on the right making use of the fact that electrostatic or magnetic fields, applied at right angles to the beam, can be used to change its direction. By scanning simultaneously in two perpendicular directions, a square or rectangular area of specimen (raster mode) can be covered and an image of this area can be formed by collecting secondary electrons from each point on the specimen.
A modern SEM provides an image resolution typically between 1 nm and 10 nm, not as good as the TEM but much superior to the light microscope. In addition, SEM images have a relatively large depth of focus: specimen features that are displaced from the plane of focus appear almost sharply in-focus. As we shall see, this characteristic results from the fact that electrons in the SEM (or the

TEM) travel very close to the optic axis, a requirement for obtaining good image resolution [4].

2.4 Superconducting quantum interference device (SQUID)

A Superconducting Quantum Interference Device (SQUID) is a very sensitive magnetometer used to measure extremely subtle magnetic fields, based on superconducting loops containing Josephson junctions[5] [7]. The SQUID combines the physical phenomena of flux quantization and Josephson tunnelling. The flux contained in a closed superconducting loop is quantized in units of the flux quantum $\Phi_0 = h/2e = 2.07 \times 10^{-15}$ Wb. Here h is the Planck's constant, and e is the electron charge. Flux quantization arises from the fact that the macroscopic wave function [7]

$$\Psi(\vec{r}, t) = |\Psi(\vec{r}, t)| \exp[i\varphi(\vec{r}, t)] \tag{2.12}$$

must be single-valued in going once around a superconducting loop. In the absence of applied fields or currents, the phase $\varphi(\vec{r}, t)$ takes the same value throughout the superconductor for all Cooper pairs, which have charge $2e$. In the case of a loop threaded by a magnetic flux, however, the phase around the loop changes by $2\pi n$, where n is the number of enclosed flux quanta.

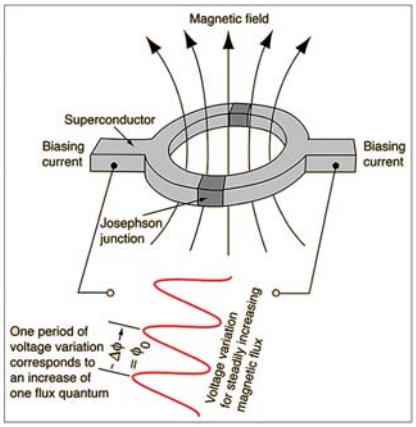

Figure 2.5: Schematic of SQUID magnetometer. Figure extracted from [8].

[5] A Josephson junction is made by sandwiching a thin layer of a nonsuperconducting material between two layers of a superconducting material.

2.5 X-ray diffraction Spectroscopy (XRD)

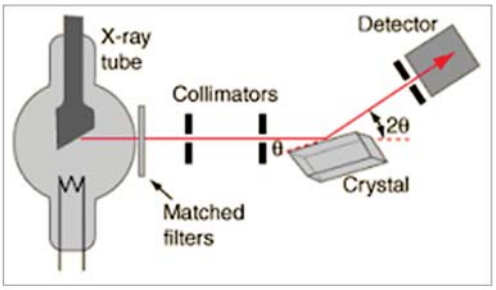

Figure 2.6: Schematic of X-ray diffraction. Figure extracted from [9].

X-ray diffraction (XRD) is a versatile, standard nondestructive contactless characterization technique that allows to investigate the crystal structure of materials in a long range order [10]. The basic principle of XRD is that crystalline materials under monochromatic X-ray irradiation produce typical patterns of reflected X-ray peaks. This was explained by modeling the crystal as a set of discrete parallel planes separated by a constant parameter d, as it is depicted in Fig. 2.7.

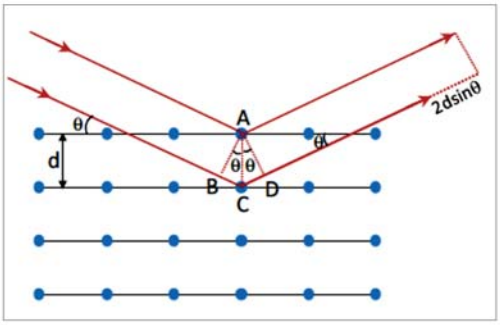

Figure 2.7: Schematic of a Bragg reflection from planes separated by a distance d. Incident and reflected rays are shown for the two neighbouring planes. Figure extracted from [9].

It was suggested that the incident X-ray radiation would produce a Bragg peak if X-rays are specularly reflected by the ions in one plane, i.e. the angle of incidence has to be equal to that of reflection and the reflected X-rays from successive planes interfere. The interference is constructive when the phase shift is a multiple of 2π; this condition can be expressed by Bragg's law:

$$n\lambda = 2d_{hkl}\sin(\theta) \tag{2.13}$$

where n is an integer representing the order of reflection, θ is the angle of incidence (equal to that of reflexion) and λ is the wavelength of the incident radiation. XRD

gives direct information on the $d-$spacing between planes, therefore any change in the crystal sequence or structure can be directly observed.

Bibliography

[1] Raman, C.V. *A new radiation.*, Indian J. Phys., 2 387, (1928).

[2] Cardona, M. and Yu, P. *Fundamentals of Semiconductors. Physics and Materials Properties.* Springer Science & Business Media, (2010).

[3] Moeller, M. *Optical properties of III-V nanowires and their application for charge transport and single-photon emission (PHD thesis)* Universidad de Valencia, (2012).

[4] Egerton, R.F. *Physical Principles of Electron Microscopy An Introduction to TEM, SEM, and AEM: Chapter 3. The Transmission Electron Microscope.* Springer-Verlag US, 57-92, (2005).

[5] `http://www.nobelprize.org/educational/physics/microscopes/tem/`

[6] `http://www.technoorg.hu/news-and-events/articles/high-resolution-scanning-electron-microscopy-1/`

[7] Clarke, J. and Braginski, A.I.,Gole,A. M., Orendorff, C.J., Gao, J., Gou, L.. Hunyadi, S.E. and Li, T. *The SQUID Handbook Vol. I Fundamentals and Technology of SQUIDs and SQUID Systems.* Wiley, (2006).

[8] `http://hyperphysics.phy-astr.gsu.edu/hbase/Solids/Squid.html`

[9] `http://hyperphysics.phy-astr.gsu.edu/hbase/quantum/bragg.html`

[10] Bunaciu, A.A., Udristioiu, E.G., and Aboul-Enein, H. Y. *X-RayDiffraction: Instrumentation and Applications, Critical Reviews in Analytical Chemistry.* Critical Reviews in Analytical Chemistry, 45(4), (2015)

Chapter 3

Synthesis, structural and magnetic characterization of Fe_3O_4 NPs

Because of their magnetic properties and Raman signature iron oxides are representative of most iron materials, for this reason in the present Chapter we describe how to deal with such kind of compounds. To do so, the magnetic and structural properties of magnetite nanoparticles and nanoparticle aggregates are characterized to become a reference in further Chapters. Importantly we found in the Raman spectroscopy an essential tool for completing the characterization of those materials. We show how Raman measurements reveal relevant information about crystallinity and stoichiometry with a minor time and material consumption.

3.1 Introduction

Iron oxides are common compounds in nature and easily synthesized in a laboratory, with 16 different cristalline phases (plus hydroxides) well-known [1]. Depending on the crystalline quality the resulting compounds can exhibit ferrimagnetism, paramagnetism or antiferromagnetism. This enables an ideal scenario for developing multidisciplinary research with application in different fields. Among all the options available here we focus on magnetite since is one of the most studied compounds. This way we can take advantage of the previous reseach to settle magnetite NPs as a reference in the discussion of our magnetic compounds [2, 3].

3.1.1 Crystal structure

Magnetite is a member of the spinel family which structure follows an inverse spinel pattern with formula $(B^{3+})^{tet}(A^{2+}B^{3+})^{oct}O_4$. In this structure all the A^{2+} ions occupy octahedral voids, while half of B^{3+} ions occupy the tetrahedral ones. In the inverse spinel structure the divalent ions site on the octahedral sites (B sites) while the trivalent ions are equally distributed in octahedral (B) and tetrahedral (A) ones. In case of magnetite, the tetrahedral and octahedral interstices are filled by trivalent Fe^{3+} ions and half of the octahedral sites are occupied by

divalent Fe^{2+} ions. This means there are $8Fe^{2+}$ at octahedral sites, $8Fe^{3+}$ at the octahedral sites and $8Fe^{3+}$ at the tetrahedral sites. The formula unit can be written as $Fe_8^{3+}[Fe_8^{2+}Fe_8^{3+}]O_{32}^{2-}$. Fig. 3.1 shows the arrangement of octahedron and tetrahedron in the inverse spinel structure.

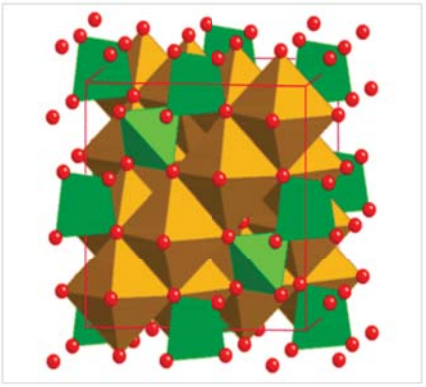

Figure 3.1: Magnetite has an inverse spinel structure. Octahedral and tetrahedral sites are represented in green and orange respectivelly. Figure extracted from [4].

Then, in the ideal case magnetite would present a ratio of $Fe^{2+}/Fe^{3+} = 0.5$. Eventually, we can find a lack of Fe^{3+} cations at the octahedral sites and other divalent ions, like Mn^{2+} or Zn^{2+}, can replace Fe^{2+}. The cubic spinel structured MFe_2O_4, or $MO{\cdot}Fe_2O_3$, represents a well-known and important class of iron oxide materials where oxygen forms a fcc close packing (Fig. 3.2), and M^{2+} and Fe^{3+} occupy either tetrahedral or octahedral interstitial sites [6].

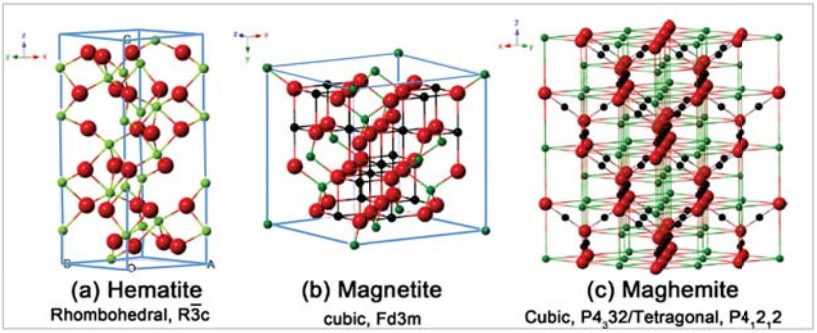

Figure 3.2: Crystal structure and crystallographic data of the a)hematite, b) magnetite and c) maghemite (atoms in black correspond to Fe^{2+}, the green ones is Fe^{3+} while the O^{2-} atoms are depicted in red. Figure extracted from [5].

Magnetic configurations of MFe_2O_4 can be adjusted, gradually losing chemical identity of Fe^{2+} to provide great number of magnetic properties. At the nano-

metric scale, MFe_2O_4 materials have been frequently chosen systems for studies of nanomagnetism due to this versatility, and furthermore have shown great potential for technological applications such as information storage and electronic devices to medical diagnostics. Also dispersions of Fe_3O_4 nanoparticles have been proposed for biomolecule tagging, imaging, sensing, and magnetic separation [7]. Given the versatility and great potential for application of inverse spinel iron oxides, our studies on magnetite NPs would be of interest for researchers in those fields, an a good reference for discussion on the properties of the iron compounds.

3.1.2 Few tips about magnetism

The applications of iron oxides mostly rely on their magnetic properties, so it is essential to study their magnetism and how it may affect other functionalities. Here we are going to discuss about general information that we can collect from magnetic measurements, for more details about the properties of magnetic materials see [9]. Probably the most clear signature of magnetic ordering is the hysteresis loop, i.e. M(H) curve, like the one in Fig. 3.3.

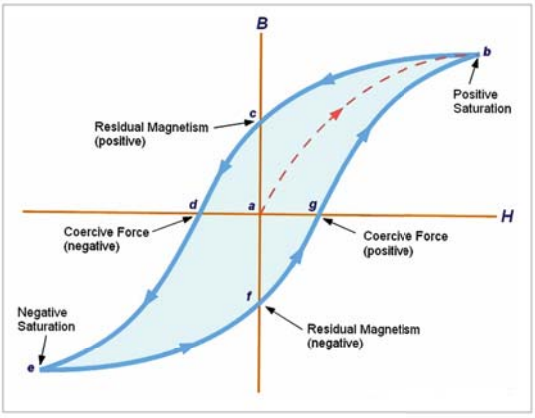

Figure 3.3: Scheme of a representative hysteresys loop. Figure extracted from [8].

In the hysteresis loop corresponding to an ordered magnetic material we can find few representative points labeled from "a" to "g" in the figure below. a) would be the magnetization at the initial point, before to apply magnetic field. b) and e) are the saturation magnetization points; c) and f) are the remanent or residual fields; and d) and g) are the coercivity points, which are representative of the coercivity field. The hysteresis loop of any magnetic material can be experimentally acquired from that curve, with those data, we can estimate $M_S = b - e/2$; $M_R = c - f/2$ and $H_C = g - d/2$. This magnitudes are of common use for de-

scription of the magnetic behavior. The coercivity of a magnetic material can be defined as the amplitude of the magnetic field which must be applied for reducing the magnetization of a ferromagnetic material to zero (after being saturated). In a similar way, the remanence field comes from the residual magnetism observed in an ordered medium after the external magnetic field is removed; while the saturation occurs when the increase of the magnetic field does not affect magnetization any more. The ratio between these parameters will give the first insights about the magnetic properties of our samples, since it reveals the relationship between the external field an the magnetization.
For example, wide and square $M(H)$ loops are representative of hard magnetic materials. In contrast, soft magnets present smoother loops. Both kind of magnets are illustrated in Fig. 3.4. In that scheme we can also see how the magnetic response is mainly determined by the material magnetization, but still the magnetic domain size may play an important role [9, 10].

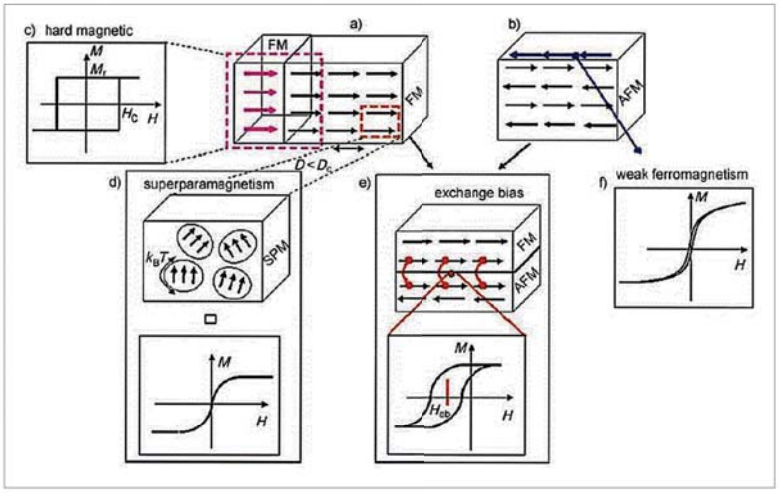

Figure 3.4: Diagram of different spin arrangements in magnetic nanoparticles: a) Ferromagnetism (FM), b) Antiferromagnetism (AFM), D = diameter, D_c = critical diameter, c) a combination of two different ferromagnetic phases in permanent magnets, which are materials with high remanence magnetization (M_R) and high coercively (H_C), d) Superparamagnetism (SPM), e) the interaction at the interface between a ferromagnet and antiferromagnet producing an exchange bias effect, and f) pure anti-ferromagnetic nanoparticles with superparamagnetic relaxation arising from uncompensated surface spins. Figure extracted from [11].

In the case of materials presenting magnetic hysteresis we might expect certain spontaneous magnetization arising from the alignment of the individual magnetic moments from each domain, while this spontaneous magnetization would be negligible in case of paramagnetic (or superparamagnetic) materials. Then, the spontaneous magnetization will be related with the magnetic ordering for the first kind of materials. Even for soft magnets the ordered states are usually

more energetically stable at very low temperatures, the magnetic order is usually prevented at room temperature because of the increase of the thermal energy in the lattice. We will come back to this in the next Chapter for the description of superparamagnetic NPs. Here we just introduce in the relation between the temperature and the ordering and its consequences for soft magnets. To do so, we can define the Curie Temperature (T_C) as the temperature where the thermal energy abruptly destroy the magnetic ordering.
Then, we can imagine a system weakly magnetized (close to its spontaneous magnetization), quite below the Curie temperature and in the presence of a weak magnetic field, this is quite below M_S. In this conditions we will find a linear relation between the magnetization and the external magnetic field, $\chi = M/H$. In this particular conditions, the evolution of the susceptibility with the temperature will present really different behavior in the case of paramagnetic or ferromagnetic materials.
In the case of paramagnets the Curie law states that the material magnetization, and then the susceptibility is inversely proportional to the temperature. We are not going to this in deep discussion, just to mention that in the solid state this thermal dependence has to do with the energy splitting of the external "*d*" bands and their irregular filling. Because of that, when increasing temperature, the magnetic susceptibility of paramagnetic materials decreases following $1/T$ law. In the case of ferromagnets the behavior is pretty similar. Even we can observe similar trend , at low temperature the M vs T plot does not follow a $1/T$ curve. In addition, when thermal energy overcomes the exchange interaction among magnetic domains it produces a randomizing effect on the orientation of the domains. This occurs at the Curie temperature (T_C) and the result is suppression of the magnetization above this temperature. As a result, we can distinguish between ferro and paramagnets by looking for the corresponding signatures at the $M(T)$ plot.

3.2 Experimental section

3.2.1 Synthesis

The experimental synthesis followed is the method developed by Sun et al. [12]. The procedure allows to range NP sizes from 4 to 20 nm in diameter. In brief, the NPs have been synthesized producing coprecipitated ferrous (Fe^{2+}) and ferric (Fe^{3+}) ions in a base, (usually NaOH or $NH_3{\cdot}H_2O$), in an aqueous solution; by thermal decomposition of alkaline solution of (Fe^{3+}) chelate in the presence of

hydrazine; by sonochemical decomposition of hydrolyzed (Fe^{2+}) salt followed by thermal treatment.

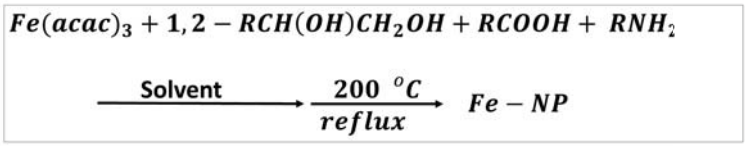

Figure 3.5: Synthesis of magnetite seeds.

This synthesis was accomplished in high-temperature (200°C). The reaction of Fe^{2+} acetylacetonate, $Fe(acac)_3$, in phenyl ether with the presence of alcohol, oleic acid and oleylamine to make monodisperse nanoparticles as seeds were used.

Synthesis of 6 nm magnetite Seeds

A solution of 6 nm Fe_3O_4 NP have been prepared to be used as a nucleation seeds on further processes. The seeds were obtained by mixing $Fe(acac)_3$ (2 mmol) in phenyl ether (20 mL) with 1,2-hexadecanediol (10 mmol), oleic (6 mmol) and oleylamina (6 mmol) under nitrogen and was heated to reflux for 30 min. After cooled to room temperature, the dark-brown mixture was treated with ethanol under air, and a dark-brown material was precipitated from the solution. The product was dissolved in hexane in the presence of oleic acid and oleyamine and reprecipitated with ethanol giving magnetite NPs with an average diameter of 6 nm.

Synthesis of 8 to 12 nm magnetite: regrowth on NP seeds

A seed-mediated growth method was used for the synthesis of larger magnetite nanoparticles [13]. In this process, few milligrams of 6nm Fe_3O_4 NPs have been mixed again with precursors and the mixture was heated to reflux for 30 min. By varying the weight ratio between the seeds and the precursors, the size of the resulting magnetite NPs could be controlled. The result was a black-brown hexane dispersion of 8 nm Fe_3O_4 nanoparticles. In an analogue way, 80 mg of 8 nm Fe_3O_4 were mixed with $Fe(acac)_3$ (2 mmol) and the glycol (10 mmol) led to 10 nm Fe_3O_4. Repeating the process on the 10 nm NP the size was increased in diameter up to 12 nm.

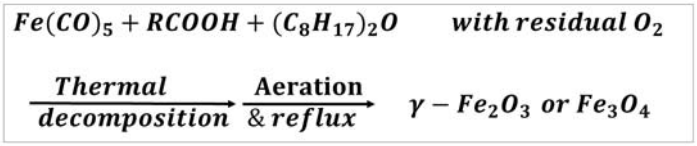

Figure 3.6: The ferrimagnetic 20-nm Fe_3O_4 nanoparticles prepared by thermal decomposition of $Fe(CO)_5$ in the presence of residual oxygen of the system.

Synthesis of magnetited NPs of 20 nm

According to [14], 20-nm $Fe_3\ O_4$ nanoparticles have been synthesized under nitrogen atmosphere. $Fe(CO)_5$ was injected into a mixture containing octyl-ether and oleic acid (1:3 molar ratios) at 100°C. The resulting mixture was slowly heated and kept on reflux for 2 h. During reflux, the yellow orange mixture changed to colorless, and latter to dark-brown. This solution was cooled to room temperature. The solution was treated with excess ethanol and separated by centrifugation.

3.3 Results and discussion

In the next, structural, magnetic and optical characterization of magnetite NPs will be show in detail. This will simplify the discussion of more complex systems on the next sections such as hybrid magnetite-gold composites or molecular iron compounds. Magnetic and Raman measurements have been carried out in NP powders and dried from organic solution with an excess of surfactant. In the next we show results from three different samples: sample A corresponding seed magnetite NPs of about 6 nm in diameter; sample B magnetite NPs of about 12 nm in diameter growth by the seed-mediated method; and sample C, magnetite NPs of about 20 nm in diameter growth by thermal decomposition of $Fe(CO)_5$.

3.3.1 Structural characterization

Counting statistics based on transmission electron microscopy micrographs is a well established technique for estimating the size distribution of NPs in solution. As an example, in Fig. 3.7 a) we show two representative images corresponding to the Sample A, Sample B and Sample C. Based on these kind of images the average diameter can be found from an ensemble of about 40 NPs, in our case the average is done among more than 60 from each image. It is worth to note we carried out this counting statistics in all the samples we have studied, from that we have established a quick check list about the synthesis success. On the one hand, TEM images also give insights about the crystallinity and stoichiometry of

the NPs. On the other hand, deviations from the expected NP size are usually related to unsuccessful synthesis.

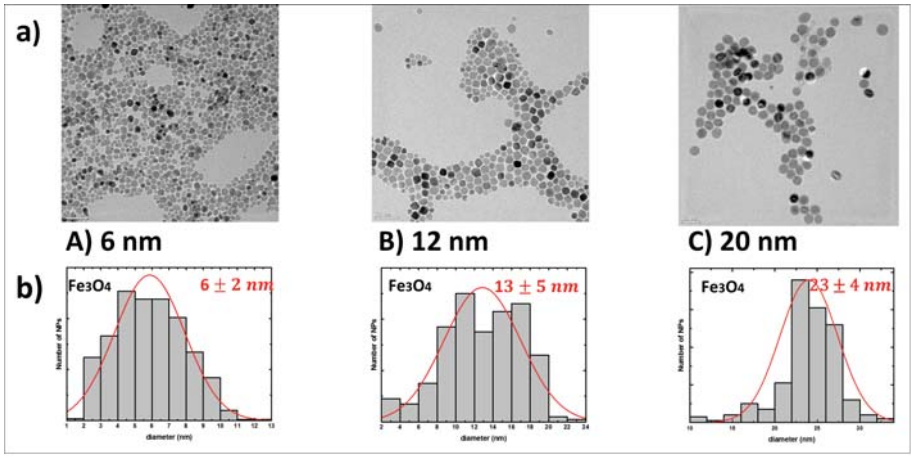

Figure 3.7: a)TEM bright field images for Sample A (6 nm), B (12 nm) and C (20 nm). Fe_3O_4 nanoparticles deposited from their hexane dispersion on an amorphous carbon-coated copper grid and dried at room temperature. The iron oxide NPs use to generate those large aggregates when dispersed with an excess of surfactant. b) Size distribution of iron oxide NPs obtained from a statistical study on TEM images for A), B) and C) Fe_3O_4 NPs.

In Fig. 3.7 b) we show the size distribution of the iron oxide NPs obtained from a counting statistics on images of the Fig. 3.7 a). As expected from chemical procedures, the resulting NPs presents certain size dispersion. For example, Sample A in Fig. 3.7 b) range between 4 and 8 nm (in diameter) with but with non-negligible occurrence probability at other sizes. The diameter dispersion shows a Gaussian profile centered at 6 $\pm$ 2 nm. In counting statistics of Fig. 3.7 b), corresponding to Sample B, we can see how the NP diameters range from 2 to 18 nm. In that case, we have also fitted the dispersion to Gaussian profile centered at 13 $\pm$ 5 nm (even more complicated size distribution could be considered). The huge broadening increase and the possible splitting of the distribution on two size families must be related with the regrowth method. Finally, in Sample C we can found an average size value of 23 $\pm$ 4 nm, with most of the NPs presenting diameters larger than 18 nm. In any case, the size dispersion estimation will be useful to discuss whether the size increase and the dispersion broadening may affect the magnetic properties. The size dispersion estimation will be useful to discuss whether the size increase and the dispersion broadening may affect the magnetic properties.

3.3.2 Magnetic characterization

The applications of our nanoparticles would be mainly determined by their magnetic performance, so it is essential to study their magnetism and possible routes towards tailoring their magnetic properties.
As above mentioned, the magnetite is a ferrimagnet; an ordered material where the spins are antiparallel aligned forming magnetic domains but showing a non-zero spontaneous magnetization because their individual momenta are not totally cancelled. Because the magnetostatic energy increases with the domain size, the bulk magnetite is found forming multi-domain structures. Nevertheless, the energy required to maintain a domain wall into a NP is not compensated by the corresponding magnetostatic decrease, and hence, single superparamagnetic domains are usually observed at the nanometer scale [15]. On the other hand, Fe compounds have got a strong magnetic moment because of the unpaired electrons at $3d$ shell, 4 in the case of Fe^{+2} and 5 in the case of Fe^{3+}. As aforementioned, the combination of both kind on ions allows different collective phenomena, such as ferromagnetism, antiferromagnetism, super-paramagnetism and a range of spin dependent states.
These properties can be observed by studying magnetization dependence on the presence of an external magnetic field [16], as described in Fig. 3.3.

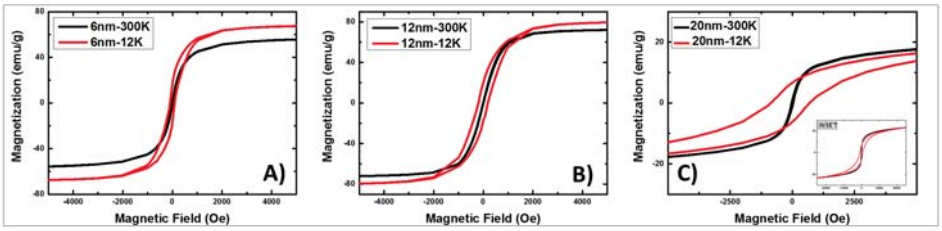

Figure 3.8: Hysteresis loop for samples A, B and C powders measured at 300 K and 12 K. Inset in c): Complete hysteresis loop of sample C to show that saturation in not completed.

In Fig. 3.8 magnetic measurements of our nanoparticles are shown. The magnetization curves are measured at different temperatures by sweeping the external magnetic field from -50000 to 50000 Oe. However, we plot the range between -5000 and 5000 for a better view of the hysteresis loops. In addition for Sample C we have included an inset showing magnetization from -25000 to 25000 in order to show saturation point. Relevant magnetization magnitudes can be observed can be observed by studying magnetization dependence on the presence of an external magnetic field [16], as described in Fig. 3.3. Samples with 8 and 10 nm measurements have been also characterized (not shown) to complete the Table 3.1. Qualitatively, the whole serie presents similar behavior at both, room and

low temperature, even quantitatively we can observe small differences. For example, in most samples M_S presents values of around 75 emu/g at room temperature (and a bit higher at 12 K).

T (K)	Size (nm)	M_S (emu/g)	M_R (emu/g)	M_R/M_S	H_C (Oe)
300	6 ± 2	59.6	0.9	0.015	8
-	8 ± 3	76	1.7	0.022	14.6
-	10 ± 3	74	1.04	0.014	9
-	13 ± 5	75.8	0.5	0.007	5.5
-	23 ± 4	38.5	1.1	0.028	29.1
12	6 ± 2	70	16.4	0.234	92.1
-	8 ± 3	76.6	16.8	0.219	193.5
-	10 ± 3	79.2	16.6	0.210	198
-	13 ± 5	82.6	17	0.206	190
-	23 ± 4	57.4	6.4	0.111	777

Table 3.1: Magnetic data at 300 and 12 K.

Just in case of Samples A and C we found lower values. In the case of Sample C this is because the NPs are not completely saturated at 50000 Oe [see inset in Fig. 3.8 c)]. In the case of Sample A we must look for a different explanation. It is well-known that $M_S = 92$ emu/g for crystalline bulk magnetite at room temperature [17, 18]. A reduction from 92 to 75 is usually found in NP solutions and can be explained by inhomogeneities in the lattice because defects, impurities or poly-crystallinity. However, the higher reduction in Sample A (up to 60 emu/g) might be related with an important variation in the stoichiometry of the sample, as discussed in the next section.

The remanent magnetization (M_R) and coercitive field (H_C) can also be estimated from those plots offering additional information. At the fist sight, $M(H)$ curves suggest that our samples are superparamagnetic at room temperature because of the lack of hysteresis. However, zooming around the low magnetic field we find certain hysteresis, which drives to the values show in Table 3.1. The magnitude of these values, below 30 Oe, can be attributed to dipole-dipole magnetostatic interactions [19], which are rather probable since our measurements have been on NPs. A better insight can be found in the M_R over M_S ratio, since it is well-know that superparamagnetic magnetite present M_R/M_S values below 0.1 [20, 21]. Notice, that AC measurements are usually required for distinguishing with respect to ensemble spin states (such as spin glasses), but in any case the ensemble states must be supported by superparamagnetic NPs. Accordingly, we found values

around 0.01-0.02 for Samples A and B and around 0.04 for sample C. At 12 K the M_R/M_S values points the superparamagnetism inhibition which explains the increase of the hysteresis in this temperature range.
The inhibition of spin fluctuations at the magnetite nanoparticles can be discussed in terms of the Stöner-Wohlfarth model [22]. This consist on numerical calculation of the integrated response of randomly oriented magnets. They assume that superparamagnetic NPs have got an effective magnetic moment with two stable antiparallel orientations that define its easy axis. In the presence of null (or very low) external field, the rotation of the magnetization easy axis is spontaneously induced by the thermal energy. However, fluctuations are prevented when the thermal energy is smaller than that of the barrier between the two stable states, and therefore, the effective magnetic moment remains blocked. This way, the Blocking Temperature (T_B) is associated to this energy barrier. A better estimation is still obtained from the ZFC-FC curves. In $M(T)$ curves we always obtained different behavior if the temperature sweep is done in the absence (ZFC) or in the presence (FC) of an external magnetic field. Importantly, the ZFC and FC fit in the superparamagnetic regime and diverges in the ferromagnetic regime, below the blocking temperature [23]. To observe this diversion point, our samples were cooled from room temperature to 2 K in the absence of magnetic field. Then, an external magnetic field (100 Oe) was applied while the temperature was slowly swept from 2 K to room temperature. The ZFC curve can be acquired by monitoring the magnetization during the warm up. After the room temperature is reached the sample was cooled again, this time maintaining the external field to obtain the FC curve. During the ZFC the superspins were blocked at zero magnetic field (while cooling down), in this situation the magnetic moments at the NPs were oriented along their easy axes. In contrast, in the case of the FC curve the external field was applied from room temperature. Then, the superspins are oriented according to the magnetic field before to be blocked. Then the magnetization can no longer change in the range from the T_B to 2 K, since the cool down does not increase the ordering.

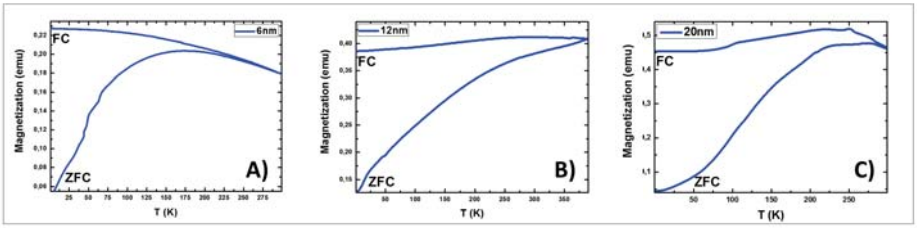

Figure 3.9: FC-ZFC curves for Samples A, B and C-magnetite nanoparticles.

In Fig. 3.9 we show the ZFC-FC curves corresponding to the samples discussed above. The Blocking can be estimated around T_B (Sample A) = 175 K where the ZFC curve exhibits its magnetization maximum. ZFC and the FC should split on such maxima but the curves are actually split at ΔT_D = 52 K the above. This early diversion is usually attributed to the broadening on the NP distribution. The point is that the larger NPs will be "unblocked" at slightly higher temperature. This in mind we can compare results on Table 3.2.

Samples	6 nm	8 nm	10 nm	12 nm	Oleate-20 nm
T_B (K)	175	275	310	-	273
ΔT_D (K)	52	31	31	-	30

Table 3.2: FC-ZFC curves.

As expected the T_B increases with the NP size, indeed, for Sample C we cannot measure it properly because its value is close to 400 K, which is the maximum temperature that we can reach at the SQUID. In the case of ΔT_D we observe a reduction in the case of 8 and 10 nm diameter samples, which presents narrower size distribution. Finally, the data from Sample C break the trend of the rest of the series. Since this sample is prepared using a different procedure, there are three different explanations for this mismatch: i) lower dipole-dipole interaction because a larger content of surfactant in the Sample C; ii) stoichiometry fluctuations in sample C because the different chemical procedure; iii) poly-crystalline facets in the seed mediate NPs. Hypothesis i) is rejected since the larger coercivity in Sample C at room temperature. For this reason, we will carry out Raman measurements in order to give light on this.

3.3.3 Raman Micro-spectroscopy on iron nanoparticles

Raman spectroscopy has proved to be a powerful tool for characterization of lattice dynamics of many compounds. Raman active vibrations are those that produce a change in the polarization of the system, leading to scattering of electromagnetic radiation by the molecules. Due to the high spectral resolution, this method it is very effective for the study of phase transformations. Raman modes from bulk magnetite have been extensively studied [24–27]. In NP powders magnetite can be oxidized to maghemite, and the latter can be thermally promoted hematite. The phase change may occur during the Raman characterization, driving to confusing conclusions. For this reason, the reader sometimes can find controversy in the description of Raman peaks of iron oxides in NP. To simplify our discussion vibrational modes of the three changes observed are listed in Table 3.3. Fortunately vibrational modes on those compounds would

drive to rather different spectra, making easy to identify and distinguish the contribution of similar phases in an inhomogeneous sample [28–30]. This is a clear advantage given the difficulty of the phase distinction by other characterization techniques, such X ray or electron diffraction.

Magnetite: Fe_3O_4	Maghemite: γ-Fe_2O_4	Hematite: α-Fe_2O_3
-	-	226-A_{1g} (strong)
-	-	245-E_g (weak)
-	381 (strong)	292-E_g (strong)
-	486 (weak)	411-E_g (weak)
532 (medium)	670 (weak)	497-A_{1g}(weak)
667-A_{1g} (strong)	718 (strong)	612-E_g (weak)

Table 3.3: Raman wave numbers.

Still most authors coincide on the fact that magnetite gets oxidized when exposed to an open atmosphere. In the case of NPs in solution the capping partially prevents from oxidation, however, the presence maghemite phase is expected. In the case of a relevant maghemite amount we need to rely on the visibility of the low energy peak of maghemite at 381 cm^{-1} since the A_{1g} mode is close in energy for maghemite and magnetite.
On the other hand, transformation of maghemite into hematite is an usual under laser irradiation of magnetite powder samples. Since this is a thermal effect, this phenomenon is highly dependent on the excitation power. For this reason, our Raman measurements have been carried out in a range of excitation powers to observe phase transitions and make the proper peak assignment. At very low excitation power, Sample A presents an inconclusive broad peak centred around 700 cm^{-1} using an excitation wavelength of 532 nm. After increasing at 0.8 mW the excitation power we can distinguish two narrower lines forming this peak, see Fig. 3.10 a), coinciding with A_{1g} modes for magnetite and maghemite. At higher excitation powers, these peaks coexist with the E_g mode of hematite and increasing the temperature to 2.1 mW we can induce many changes in the resulting Raman spectrum, see Fig. 3.10 b). This way we can clearly identify A_{1g}, E_g among other characteristic signatures of hematite. Importantly, during the transition to hematite the modes are shifted pointing out the temperature increase in the lattice. For example, A_{1g} is found at 216 cm^{-1} instead of 226 cm^{-1}. In the case of Sample B the excitation power can be reduced more than one order of magnitude (up to 0.07 mW in Fig. 3.11 a) and still we can obtain more clear Raman spectra. This can be understood as an increase of the scattering cross-section in the case of

larger diameter NPs. In this situation we can induce the presence of the magnetite phase with exciting at 0.78 mW, see Fig. 3.11 b).

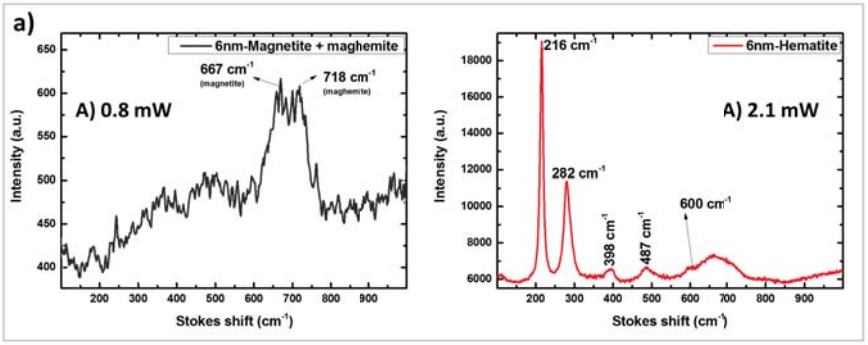

Figure 3.10: illustrates the Raman spectra measured for sample A at 0.8 and 2.1 mW.

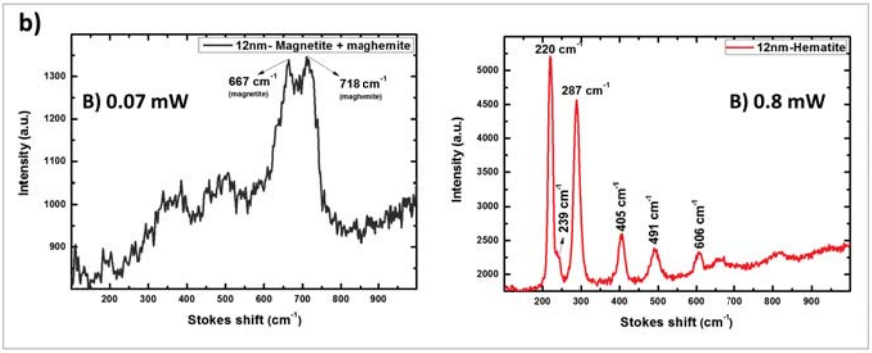

Figure 3.11: illustrates the Raman spectra measured for sample B at 0.07 and 0.8 mW.

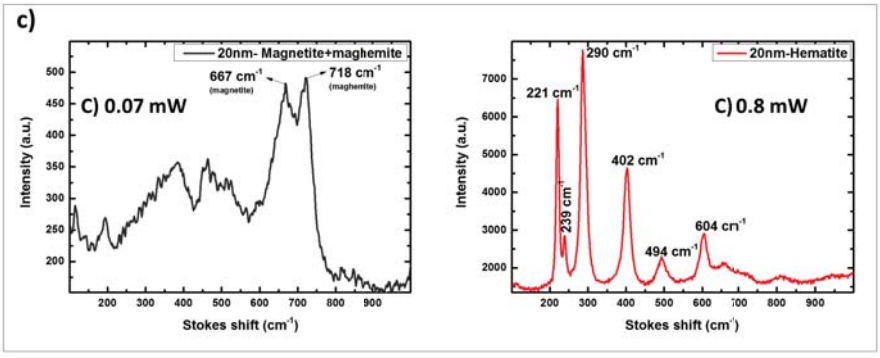

Figure 3.12: illustrates the Raman spectra for sample C at 0.07 and 0.8 mW.

Now, the shift for A_{1g} of hematite is at 221 cm^{-1}, just 4 cm^{-1} below literature values. Then, we can conclude that this is because the temperature sample is not as high as in the case of Sample A at 2.1 mW. Notice that the combination of factors relax the measurement demands. Because of optical scattering increase with the NP diameter, we can find higher signal under lower excitation powers. At the same time, the NP also absorbs in a more efficient way, then, we can force the magnetite to hematite change with lower excitation powers. The situation is even improved in Sample C NPs. See Fig. 3.12 a), at low excitation power we obtain clearer spectra when exciting at 0.07 mW, and new peak arising when exciting at 0.8 mW, see for example the peak about 239 cm^{-1} in Fig. 3.12 b). It is worth to mention, that despite the larger contribution of the hematite under high excitation powers, the maghemite and magnetite phases are still observed in such spectra. Indeed, the phase change is reversible in certain circumstances. This is, when measuring at intermediate power during few seconds we can identify the onset of the hematite contribution and isolate again the magnetite and maghemite peaks by reducing the power. But this phenomenon is not hundred percent reproducible, and sometimes it shows different dynamics by inspecting different points of the sample. As a result, more statistics would be required in order to demonstrate reversibility and control on the phase transition dynamics. In further works, we are planning to perform an study on the Raman evolution as a function of the temperature in order to offer a better description of this phenomenon. For the moment, we just wanted to demonstrate that the Raman measurements are useful to complete structural and magnetic characterization. Structural characterization techniques do not allow to distinguish a maghemite phase in magnetite sample. Just in the case of Sample A we may think about an stoichiometry variation because of the reduction of M_S. However, the magnetite and maghemite X-ray fall on the same spectral location, so both phases just can be distinguished in high resolution electron diffraction patterns when supported by analytical techniques. In addition, just in very crystalline thick samples can give insights in electron diffraction patterns. Thanks to the Raman measurements, we clearly distinguish this phases in our Raman spectra. Still we may not be able to quantify the ration between the magnetite and the maghetite phase, but in combination with the magnetic measures, we can conclude that this ratio would be clearly higher in the case of Sample A. The maghemite phase might be forming a shell of few nm around the magnetite, and accordingly, would result more important in the case of smaller NPs.

3.4 Conclusions

After giving a brief introduction on the iron oxides, we have discussed the processes of synthesis, structural and magnetic characterization of magnetite NPs. This way we could introduce these complex systems while pointing out the differences between bulk materials and nanomagnets. As an usual procedure, we estimate the average diameter and size dispersion using counting statistics before to perform magnetic characterization. We have compared magnetic properties in a series of samples at room and low temperature showing their superparamagnetic character, discussing most relevant magnetic magnitudes and estimating the blocking temperature for the whole series. We also remarked some deviations from our result with respect to literature. After that, the characterization is completed by means of Raman spectroscopy. This way, we demonstrate the presence of a maghemite phase, probably surrounding the magnetite NPs. We also discuss about the controversy usually found in literature regarding the phase change from maghemite to hematite, which sometimes has led to some authors to a wrong Raman peak assignment. The presence of this phase is rather complicated to demonstrate by means of structural characterization, however, explains the reduction of saturation magnetization in the case of small diameter NPs. In the next chapters, during the study of more complicated system where the iron ions play more relevant role, the use of Raman spectroscopy will be essential for the proper characterization of the compounds.

Bibliography

[1] Cornell, R. M. and Schwertmann, U.*The iron oxides.*, Wiley-VCH GmbH Co. KGaA, (2003)

[2] Arora, S.K., Wu, H.C.,Choudhary, R.J.,Shvets, I.V.,Mryasov, O. N.,Yao, H. and Ching, W.Y.*Giant magnetic moment in epitaxial Fe_3O_4 thin films on MgO (100).* Phys. Rev. B 77, 134443, (2008).

[3] Walz, F. *The Verwey transition- a topical review.*, Condens. Matter., 14, R285, (2002).

[4] `https://chemistry.stackexchange.com`

[5] Wu, W., Wu, Z., Yu, T., Jiang, C. and Kim, W.S. *Recent progress on magnetic iron oxide nanoparticles: Synthesis, surface functional strategies and biomedical applications.* Science and Technology of Advanced Materials, 16(2), (2015)

[6] (a) West, A.R. *Basic Solid State Chemistry* John Wiley & Sons: New York, 356-359, (1988). (b) O'Handley, R.C *Modern Magnetic Materials-Principles and Applications* John Wiley & Sons: New York, 126-132, (2000).

[7] Häfeli, U., Schütt, W.,Teller, J. and Zborowski, M.*Scientific and Clinical Applications of Magnetic Carriers.*, Plenum Press: New York, (1997).

[8] Electronic Stack Exchange `https://electronics.stackexchange.com`

[9] Coey, J.M.D. *Magnetism and magnetic materials.* Cambridge University Press, (2010).

[10] Landau, L.D. and Lifshitz, E.M. *Theory of the dispersion of magnetic permeability in ferromagnetic bodies.* Phys. Z. Sowietunion, 8, 153, (1935).

[11] Lu, A.H., Salabas, E.L. and Schuth, F. *Magnetic nanoparticles: synthesis, protection, functionalization, and application.* Angew. Chem. Int. Ed., 46(8), 1222-44, (2007).

[12] Sun, S. and Zeng, H.*Size controlled Synthesis of Magnetite Nanoparticles.* Journal of American Chemistry Society,124, 8204, (2002)

[13] (a)Brown, K.R. and Natan, M.J. *Hydroxylamine Seeding of Colloidal Au Nanoparticles in Solution and on Surfaces.* Langmuir,14, 726, (1998).

[14] Kyoungja W., Jangwon, H., Sungmoon, C.,Hae-Weon, L., Jae-Pyoung, A., Chul, S.K. and Sang, W.L. *Easy Synthesis and Magnetic Properties of Iron Oxide Nanoparticles.* Chem. Mater., 16, 2814-2818, (2004).

[15] Canet-Ferrer, J., Albella, P., Usagre, J.V. and Maier, S.A. *Hybrid magnetite-gold nanoparticles as bifunctional magnetic-plasmonic systems: three representative cases.*, Nanoscale Horizons, 4(2), 205-216, (2017).

[16] Teja, A.S, Koh, P.Y. *Synthesis, properties, and applications of magnetic iron oxide nanoparticles.* Progress in Crystal Growth and Characterization of Materials 55, 22, (2009).

[17] Rosensweig, R.E. *Ferrohydrodynamics.* Dover Publications, (1997).

[18] Thanh, T.K. *Magnetic Nanoparticles: From Fabrication to Clinical Applications.* CRC Press, (2012).

[19] Mørup, S., Hansen, M. F. and Frandsen, C. *Magnetic interactions between nanoparticles.* Beilstein J. Nanotechnol,1, 182-190, (2010).

[20] Goya, G.F., Berquo, T.S., Fonseca, F.C. and Morales, M.P. *Static and dynamic magnetic properties of spherical magnetite nanoparticles* J. Appl. Phys.,94, 3520-3528, (2003).

[21] Yang, T., Shen, C., Li, Z., Zhang, H., Xiao, C., Chen, S., Xu, Z., Shi, D., Li, J. and Gao, H. *Highly Ordered Self-Assembly with Large Area of Fe_3O_4 Nanoparticles and the Magnetic Properties.* J. Phys. Chem. B, 109(49), 23233-23236, (2005).

[22] Stoner, E.C., and Wohlfarth, E. P.*A mechanism of magnetic hysteresis in heterogeneous alloys.* Philosophical Transactions of the Royal Society A: Physical, Mathematical and Engineering Sciences. 240 (826): 599-642, (1948).

[23] Dodson, M.H. and McClelland-Brown,E. *Magnetic blocking temperatures of single-domain grains during slow cooling.* Journal of Geophysical Research, 85(5), 2625-2637, (1980).

[24] Verble, J.L. *temperature-dependent light-scattering studies of the Verwey transition and electronic disorder in magnetite.* Phys. Rev. B, 9, 5236, (1974).

[25] Degiorgi, L., Blatter-Mörke, I. and Watcher, P. *Magnetite: Phonon modes and the Verwey transition.* Phys. Rev. B, 35, 5421, (1987).

[26] Hart, T.R, Adams, S.B and Tempkin, H. *In Proceedings of the 3^{rd} International Conference on Light Scattering in Solids.* edited by Balkansky, M.; Leite, R. and Porto, S. Flammarion, 254, Paris 1976.

[27] Graves, P.R. and Campiello, J.J. *temperature-dependent light-scattering studies of the Verwey transition and electronic disorder in magnetite.* Mater. Res. Bull., 23, 1651, (1988).

[28] Shebanova, O.N. and Lazor, P. *Raman study of magnetite (Fe_3O_4): laser-induced thermal effects and oxidation.* J. Raman Spectrosc., 34, 845,

(2003).

[29] El Mendili, Y., Bardeau, J-F., Randrianantoandro, N. Greneche, J-M. and Grasset, F. *Structural behaviour of laser-irradiated γ-Fe_2O_3 nanocrystals dispersed in porous silica matrix : γ-Fe_2O_3 to α-Fe_2O_3 phase transition and formation of ϵ-Fe_2O_3.* Sci Technol Adv Mater., 17(1),597-609, (2016).

[30] Romdohr, P. *The Ore Minerals and their intergrowths.*, Pergamon Press, Toronto, (1969).

Chapter 4

Combination of magnetite and gold nanoparticles to improve Raman characterization.

Combination of magnetite and gold nanoparticles have been extensively used as bifunctional materials for bio- and nano-technology. The properties of those systems are often assumed to be closely related the geometry of the resulting hetero-structures. This also applies to the the magnetic properties of core-shell, dumbbell-like dimers and chemical cross-linked pairs of magnetite and gold nanoparticles. It was showed how the presence of gold may damp the magnetic response of these systems in certain conditions, and how the system geometry partially prevents such damping. As an advantage, the presence of gold enables surface enhanced Raman characterization of the samples obtaining relevant structural information as a result. The materials have been provided by Prof. A Ribera and J. V. Usagre from UIMM at ICMol.

4.1 Introduction

Nanotechnology is continuously demanding combination of materials to provide multiple functionalities on the same sample. For this reason, over the last years the combination of magnetite with noble metal nanoparticles (NPs) has received a lot of attention [1–3]. Among the different options, magnetite-gold NPs are being developed, because they have shown both multifunctionality and chemical stability [4–6]: Gold NPs support tunable plasmon resonances while magnetite NPs support resonances at GHz frequencies [7, 8]. Both the magnetite and the gold clusters are of interest for photocatalysis enhancement [8,9]. In this work, the magnetic properties of core-shell NPs, dumbbell-like dimers and chemical cross-linked pairs of magnetite and gold NPs are compared. We focus on these because they are representative cases of contact between hetero-structure constituents. Importantly, we have observed that in the core-shell the magnetic response reduced the magnetism of the system. An alternative to avoid such magnetic damping is found on the dumbbell structure. This consist of growing small gold clusters on large magnetite NPs, thus we keep a high magnetite to gold mass ratio. In

the case of the cross-linked structures, the separation between the magnetic and plasmonic NPs partially prevents the diamagnetic effects of gold, and then we can link relatively large gold NPs without hindering the magnetic response of the system. From the comparison between the different systems, we offer an overview of the interaction between magnetic and plasmonic NPs. For readers with particular interest on the plasmonic properties a complete description of the optical properties of the systems will be published elsewhere.

4.2 Experimental section

4.2.1 Synthesis and samples

The synthesis of the nanostructures has been carried out by thermal decomposition of gold and iron oxide precursors under argon environment in organic solution at controlled temperature. More details about the procedures can be found in [10]. We start describing the core-shell structure (Sample A), Figs. 4.1 a) and b).

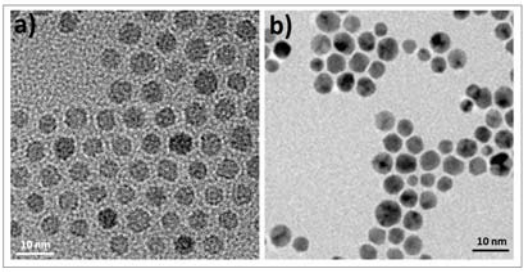

Figure 4.1: TEM micrographs of core a) and the latter core-shell b) NPs. The presence of the shell supposes a slight increase in the average diameter and a higher contrast at the TEM images because of the increase of the electron scattering at the gold shell.

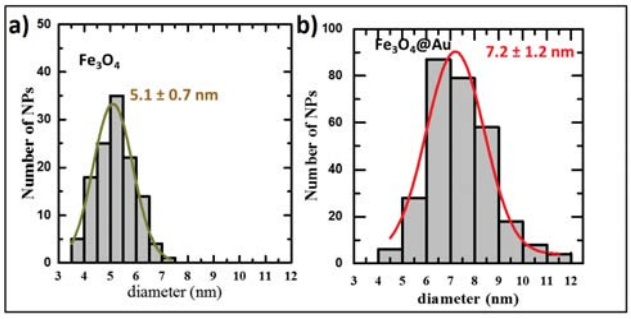

Figure 4.2: Size distribution of iron oxide core a) and core-shell b) NPs obtained from a statistical study on TEM images. The size of the iron oxide NPs ranges between 4 and 6.6 nm being the average size about 5.1 nm while the core-shell NPs range from 5 to 9 nm with an average diameter about 7.2 nm. As a result, an average shell growth of about 2 nm is estimated.

Roughly speaking Sample A was obtained by growing a gold shell by injection of $HAuCl_4 \cdot 3H_2O$ in a solution of previously synthesized Fe_3O_4 NPs (which are used

as nucleation centers). In particular, we are going to show result NPs with an average core diameter of $D_C = 5.1 \pm 0.7$ nm. The diameter of the NP raises up to $D_S = 7.2 \pm 1.2$ nm after the shell growth, then we can estimate an average thick shell of 1 nm (see counting statistics in Fig. 4.2). For the case of the dumbbell, Sample B, the NPs have been synthesized with minor modifications on the procedures in [11]. The synthesis begins with the growth of Fe_3O_4 NPs from $Fe(CO)_5$ precursor, but in this case, $HAuCl_4 \cdot 3H_2O$ is injected before running up the iron oxide precursor. The iron oxide NPs previously grown act as seeds (i.e. nucleation centers) for the gold clusters. A TEM micrograph corresponding to the case of 2.9 ± 0.8 nm gold NPs grown on iron oxide seeds is shown as an example in Fig. 4.3.

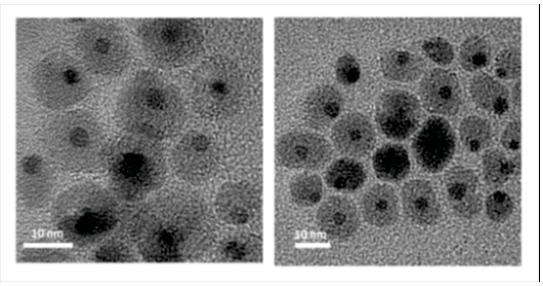

Figure 4.3: Representative TEM micrographs of the dumbbell like NPs studied, Sample B.

The average diameter of the iron oxide is $D_{Fe} = 11 \pm 3$ nm with certain size and shape distribution, see Fig. 4.4.

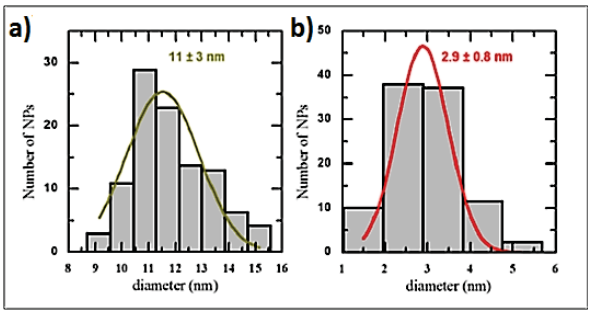

Figure 4.4: Counting statistics obtained from different images for a) the magnetite and b) gold clusters.

Finally, Fe-Au cross-linker pairs are obtained from the chemical cross-linking of magnetic and plasmonic NPs. The strategy is based on previous studies demonstrating that the -NH_2 groups of the capping can be readily substituted by stronger ligands (such as -HS or -COOH) [12]. The result is a diluted solution of cross-linked structures comprising a range of interparticle distances (Fig. 4.5).

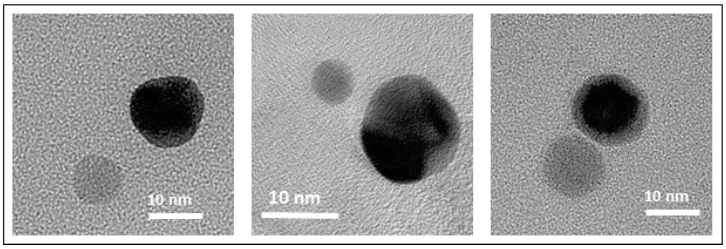

Figure 4.5: Representative TEM micrographs of Sample C showing different interparticle distances.

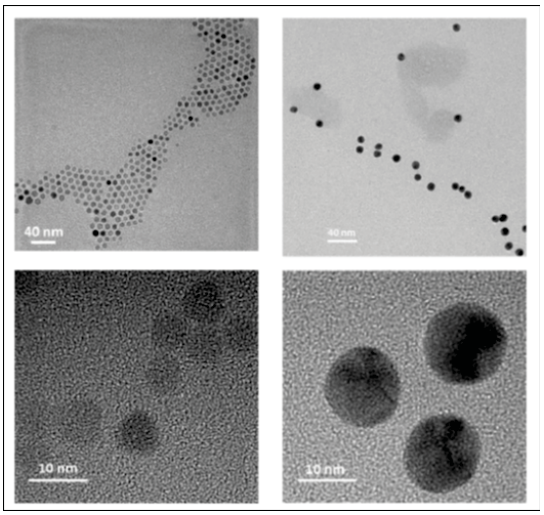

Figure 4.6: Representative TEM micrographs of a) the magnetite and b) gold NPs employed in the linking procedure.

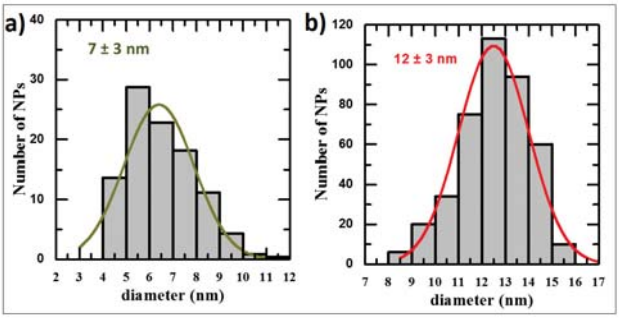

Figure 4.7: Size distribution of a) the iron oxide NPs and b) gold NPs before linking.

In this chapter we combine gold NPs with diameters of $D_{Fe} = 7 \pm 3$ and $D_{Au} = 12 \pm 3$ nm. See Figs. 4.6 and 4.7 for the TEM micrographs and counting statistics respectively. This procedure allows the combination of previously synthesized

gold and iron oxide NPs offering multiple combination possibilities [13]. As an advantage the NP growth does not depend on the relative amount of gold and iron oxide during the synthesis, since they are prepared aside. The procedure include two dialysis steps to remove extra surfactants and remaining reagents to prevent the formation of large aggregates, as confirmed by dynamic light scattering measurements (DLS).

4.3 Results and discussion

4.3.1 Magnetic measurements

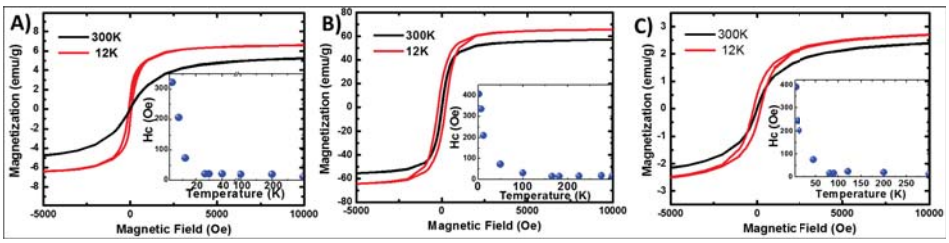

Figure 4.8: Hysteresis plot of Samples A, B and C.

The applications of our hybrid systems are determined by their magnetic properties, hence, it is essential to study their magnetism and how it is affected by the presence of the gold clusters (as we saw in the previous Chapter). The magnetite is a ferrimagnet; an ordered material where the spins are antiparallel aligned forming magnetic domains [14]. The bulk magnetite is found forming multi-domain structures since the magnetostatic energy is increased with the domain size [15,16]. However, the energy required to maintain a domain wall into a NP is not compensated by the corresponding magnetostatic potential decrease, and hence, single superparamagnetic domains are likely observed at the nanometre scale as discussed in Chapter 3. In Fig. 4.8 we show magnetic measurements carried out on our three representative systems. The magnetization curves are measured at different temperatures by sweeping the external magnetic field from 50000 to -50000 Oe. However, we plot the range between 10000 and -5000 for a better view of the hysteresis loops. The magnetization saturation, remanent magnetization and coercive field can be estimated from those plots [17].
The magnetism of the Sample A is studied and compared with the magnetic properties of bare magnetite NPs, specifically the core NPs extracted previously to the gold injection. Since both samples come from the same synthesis the role of noble metal is revealed. At room temperature, the hybrid system presents a coercive field of about $H_C = 12$ Oe with a saturation of $M_S = 5.1$ emu/g at 50000

Oe. The ratio observed between the remanent and the saturation magnetization reveals the superparamagnetism of the hybrid system. As discussed in Chapter 3 superparamagnetic magnetite NPs present $M_R/M_S < 0.1$ [18], while we have observed a value of about $M_R/M_S = 0.01$. On the other hand, the coercivity and the saturation are increased when cooling down to low temperatures. For example, at 12 K we found $H_C = 74$ Oe and $M_S = 6.7$ emu/g. In the reference sample we found similar coercivity but higher saturation values, i.e. $H_C = 60$ Oe and $M_S = 59.2$ emu/g at 12 K as we have seen in Table 4.1. The saturation values from the reference sample coincide with the usually found in magnetite NPs of this size, and they are very close to the values found in magnetite NPs from Chapter 3.

Magnitude	core: Ref. Sample A	Sample A	Sample B	NPs before linking: Ref. Sample C	Sample C
M_S (emu/g) (300 K)	50.8	5.1	60.1	71.7	2.6
M_R (emu/g) (300 K)	0.3	~ 0.04	1.77	0.7	~ 0.02
M_R/M_S (300 K)	< 0.01	~ 0.01	0.03	< 0.01	~ 0.01
H_C (Oe) (300 K)	14	12	15	14	14
M_S (emu/g) (12 K)	59.2	6.7	68.1	79.9	2.9
M_R (emu/g) (12 K)	4.7	1.2	7.69	10.4	0.5
M_R/M_S (12 K)	0.08	0.18	0.29	0.13	0.17
H_C (Oe (12 K)	60	74	210	155	203
T_B (K)	29.5	26.4	165	91.7	81
ΔT_D (K)	6.4	55.3	40	~ 100	~ 140

Table 4.1: Summary of the magnetic measurements: magnetic properties of the three systems under study and reference samples.

In both samples, the coercivity increase at 12 K points an inhibition of superparamagnetism at low temperatures. Notice the lower M_S in Sample A is explained by the relative iron oxide weight reduction in the system; indeed the reference sample values are recovered if the hysteresis loops are properly re-normalized. At room temperature Sample B presents saturation and coercivity in the order of the

core NPs. This is because of the low quantity of gold introduced in that system. We found M_S = 60.1 emu/g and H_C = 15 Oe, but with higher remanence M_R = 1.8 emu/g, see Table 4.1. The increase in the remanent field can be attributed to the shape anisotropy of the iron oxide clusters. At room temperature the ratio M_R/M_S = 0.03 is still into the range of superparamagnetism, however, at low temperatures the coercivity of Sample B NPs is considerable larger than that of Sample A (e.g. H_C = 210 Oe at 12 K). This suggests that in Sample B the superparamagnetism is inhibited at higher temperatures. This will be confirmed by the ZFC-FC curves below. In the case of the cross-linked nano-structures the magnetite NPs before linking are used as reference sample. At room temperature such NPs also present superparamagnetism with magnitudes in the order of the core NPs: M_S = 71.7 emu/g, H_C = 14 Oe and $M_R/M_S < 0.01$. After the linking process the resulting composite maintains the ratio M_R/M_S but with a dramatic reduction of M_S due to the huge presence of gold, M_S = 2.6 emu/g. The evolution of those magnitudes with the temperature are similar to the rest of samples and just quantitative differences are observed. At 12 K, the coercivity of the reference is about H_C = 155 Oe, which is in between those found for the core NPs and Sample B. After cross-linked, the coercivity rises up to H_C = 203 Oe at 12 K, a similar increase if compared to the one observed between the core and the core-shell in that temperature range.

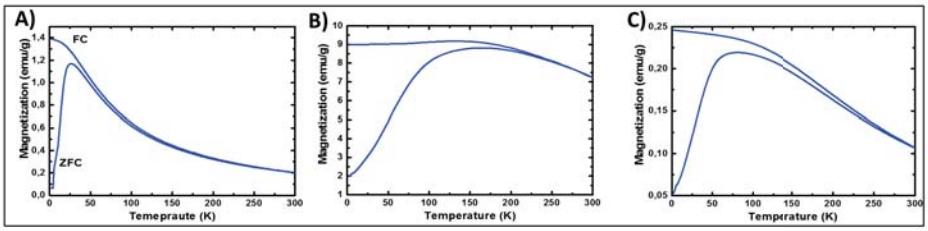

Figure 4.9: ZFC-FC curve of Samples A, B and C respectively.

The inhibition of spin fluctuations can be monitored by studying the H_C evolution with the temperature, see insets on Figs. 4.8 a), b) and c) [19]. The evolution of the coercivity with the temperature gives a first insight about T_B. A better estimation is obtained from the ZFC-FC curves [20]. Remember that the ZFC and FC curves diverge below T_B, and coincide up to that temperature where the spin fluctuations are enabled by thermal energy and magnetization is sensitive to external magnetic field. At Fig. 4.9 a) the ZFC-FC plot of the Sample A is shown. The Blocking temperature is around T_B^{C-S} = 26.4 K where the ZFC curve exhibits its magnetization maximum. This value is close to the one found for the core NPs, T_B^{CORE} = 29.5 K. The divergence of the ZFC and the FC should be

found on such maxima but the curves are actually split at higher temperatures. The origin of this diversion lies in the fact that all NPs are not blocked at the same temperature due to size, shape or composition inhomogeneities [21]. The few Kelvin mismatch observed on the reference core NPs, $\Delta T_B = 6.5$ K, is associated to the broadening of the NP size distribution [22]. Notice this value of ΔT_B is considerable lower than those one found in any of the samples of Chapter 3. Accordingly, we attribute this moderated value to a narrow size distribution. But notice that the core NPs and the magnetite forming the Sample A come from the same synthesis and the same shape and size distribution are expected in both cases. For this reason the larger divergence observed at the hybrid system (T_B^{C-S} = 55 K, i.e about 50 K broadening) must be related with the presence of the gold shell. The reason is that the external magnetic field is partially screened by diamagnetic materials (like gold), such a way the strength of the magnetic field is reduced into the shell. This effective magnetic field reduction will depend on the shell thickness explaining the increase in T_B due to the range of shells observed. In the case of the Sample B we have not found the proper reference sample since the injection of gold during the final steps of the iron oxide synthesis has important consequences on the growth of the magnetic cluster. However, the behavior shown in the dumbbell like NPs [in Fig. 4.9 b)] is qualitatively similar to bare magnetite NPs [15, 23]. Looking for quantitative differences T_B occurs at higher temperatures (when compared with the core for example), $\Delta T_B = 165$ K. The increase on the Blocking Temperature is attributed to the non-spherical geometry found on the iron clusters which drives to higher energy barriers [18]. This value is still lower than the one found for 12 nm of Chapter 3 pointing out the crystalline quality of those NPs. In addition, the range of sizes and shapes observed in the TEM images is consistent with the value of $\Delta T_B = 40$ K and comparable with samples of Chapter 3. In the case of the cross-linked structures, the magnetite before linking can be used as a reference. In this sample T_B is found in the middle of the values of the core-shell and dumbbell NPs, $T_B^{BL} = 92$ K, see Fig. 4.9 c). According to the previous discussion, this is consistent with the NP size distribution since their average diameter is in between those samples. Such value is slightly reduced after linking, $T_B^L = 81$ K, as occurs when comparing the core NPs with Sample A. Hence, it is reasonable to attribute the variations on the magnetic properties to the gold diamagnetism in both cases. About the magnetic damping, the influence of gold seems to be comparable in both systems, despite the gold content is larger in Fe-Au heterostructures (i.e. about a 50 K increase in T_B with respect to the corresponding reference sample). This points that the linker structure is more convenient than the core-shell to maintain the magnetic properties in systems with a significant presence of gold. The reason

is that in Sample A the magnetic cluster is surrounded by the noble metal while in the cross-linked structures the separation between both kinds of NPs prevents from stronger diamagnetic effects. This is important because larger gold NPs will enable capabilities for dark-field imaging, light enhancement in dual imaging of bio-samples.

4.3.2 Raman spectroscopy

As we have seen in the previous chapter Raman spectroscopy offers valuable information for the study of the magnetite NPs. Particularly interesting is the possibility to identify different phases in the same magnetite samples. A priori, we must expect higher resolution from the combination of magnetite with gold because of the SERS effect. In the next, we will demonstrate that the surface Raman enhancement does not result straightforward, and then, additional synthesis efforts must be done to optimize the NP combination. Firstly, we could not obtain Raman signal from our heterostructures in powder, this is, working in an analogous way to the Raman characterization in Chapter 3. After many efforts, we understood that the presence of gold increases the absorption of the iron oxide cluster, heating the sample and avoiding the proper Raman characterization. This fact has been reported for a range of hetero-structures. Indeed, there is a new trend in SERS experiments to substitute plasmonic by dielectric nano-antennas in order to minimize this effect [24]. To avoid this, we have carried out the Raman characterization of the hybrid systems in diluted solution. In these conditions we have been able to characterize Samples A and B, but we could not get signal from Sample C. This makes sense, since we may expect SERS from Samples A and B, but not from sample C due to the large inter-particle distance estimated for DLS measurements.

Before to go in deep on this, we would need to describe the results and the conditions of the Raman measurements. Diluted solutions of A and B ($<$ 1mg/100ml) have been prepared on toluene and dropped in a quartz cuvette. The cuvette is located on the holder of our Raman set-up to be irradiated (consecutively) using three different laser sources at 532, 633 and 785 nm wavelength. In every case, the excitation power was 1 mW using a 20$\times$ microscope objective to focus the light and to collect the backscattering. In the case of Sample A, Fig. 4.10, we have got clear Raman signature from magnetite at 667 cm^{-1} at the three excitation wavelengths studied. The magnetite mode is always accompanied by two strong vibrational modes, exhibiting narrow lines at 257 and 364 cm^{-1}. Notice that those peaks would not fit either with maghemite neither with hematite modes. We can also observe that the intensity ratio among those peak is the same at the three wavelengths studied, and the signal is clearly higher at the visible and maximum

at 633 nm. At those powers we can also observe a relevant contribution of a broader band centered around 800 cm^{-1}. The situation is different in the case of Sample B, see Fig. 4.11. In the dumbbell structures the main signal comes from the band located at 800 cm^{-1}, where now we can distinguish certain structure. Importantly, the magnetite is not present in any spectra and just in the case of 532 nm excitation wavelength we can distinguish that peak at 364 cm^{-1}.

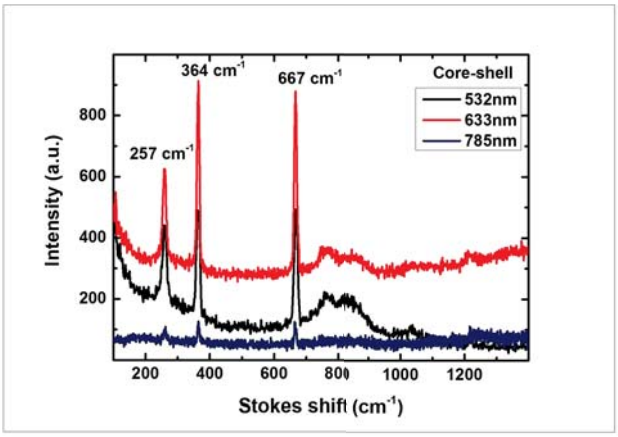

Figure 4.10: Raman signal dependence on excitation wavelength for Sample A.

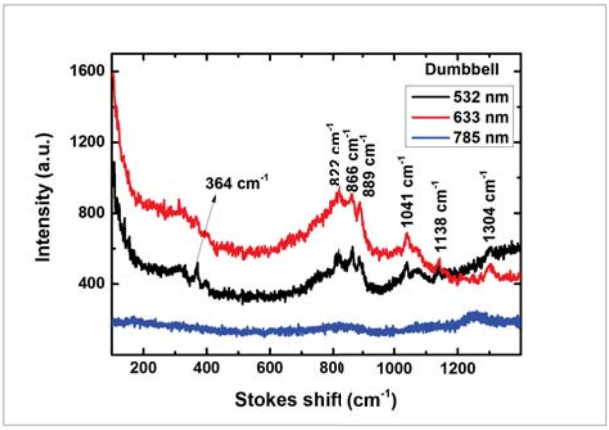

Figure 4.11: Raman signal dependence on excitation wavelength for Sample B.

From the experimental results we can conclude that we have some surface enhancement effect but it must be different for any sample. To give light on this in Fig. 4.12 we plot numerical simulations for the structures under study. Notice that the SERS effect would be proportional to the fourth power of the electrical field increase [24]. In that figure, we compare the increase of a single NP with and

without the gold surrounding. For example, in average the higher enhancement can be expected for Sample A, as can be concluded from the comparison between the core [Fig. 4.12 a)] and the core-shell geometry [Fig. 4.12 b)]. This will explain higher signal in Sample A at the visible, and the corresponding reduction when measuring at 785 nm. Importantly, such enhancement is maximum around the shell, then we can assume that the observed (enhanced) modes correspond to material located around the gold shell. This suggest the presence of another iron oxide phase that would appear around the magnetite during the gold growth. This new phase and the gold shell may be protecting the magnetite from oxidation to maghemite.

The situation on Sample B is a bit different; in this case, the field distribution is similar if we compare the single NP with the dumbbell like structure, see Figs. 4.12 c) and d). No relevant enhancement is expected, just very close to the gold cluster we can distinguish a small hot spot. Probably, for this reason we have got signal from the peak at 364 cm^{-1} but not from the magnetite that would be composing the rest of the sample. We can identify also certain contribution of the peak at 257 cm^{-1}, but we cannot resolve it properly because of broadening. As a result, the new phase associated to these peaks can be related to the gold cluster.

Finally, in the case of the cross-linked structures we can also see certain enhancement, but none hot spot is observed [see Figs. 4.12 e) and f)]. This low enhancement, together with a lower number of NP in solution, would explain the fact that we have not get signal from Sample C. For a more accurate discussion on these results, in further experiments, we are going to work with high concentration samples in order to quantify the SERS effect for the different geometries. It would be useful to get signal from the magnetite peaks at the dumbbell structures to confirm the correlation of the peaks at 364 and 257 cm^{-1} with the gold position. It will be also desirable to check that those peaks are not present at the linker, where the gold does not contact the iron oxide. In combination with analytical techniques, we will try find a better estimation of the system stoichiometry, and disregard the existence of vibrational modes related with the covalent bounding of gold with iron. Before that time consuming experiments, we have looked at the literature and we have found a possible candidate to attribute this vibrational modes [25]. See table 4.2.

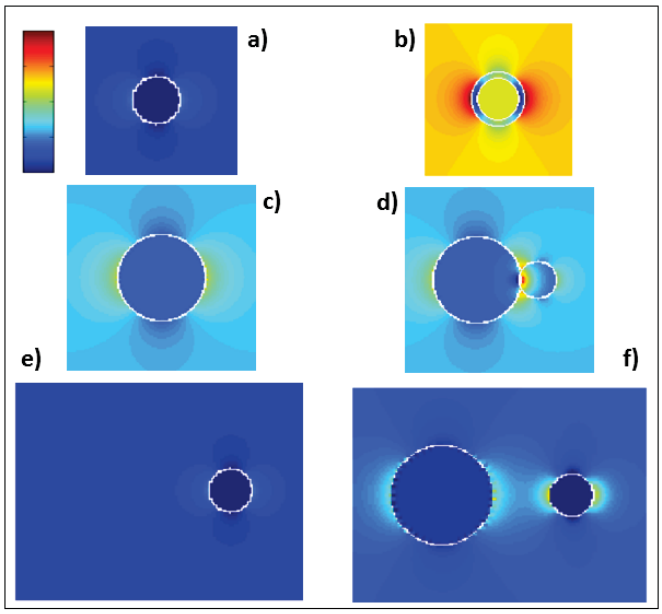

Figure 4.12: Electric field distribution of the three systems under study at 532 nm. Numerical simulation using MNPBEMDIR package for Matlab. a) and b) core vs core-shell structure. c) and d) single NP vs dumbbell dimer. e) and f) single NP vs linker.

Magnetite: Fe_3O_4	Maghemite: γ-Fe_2O_4	Hematite: α-Fe_2O_3	Lepidocrocite
-	-	-	219 (weak)
-	-	226-A_{1g} (strong)	252 (strong)
-	-	245-E_g (weak)	311 (weak)
-	381 (strong)	292-E_g (strong)	349 (weak)
-	486 (weak)	411-E_g (weak)	379 (strong)
532 (medium)	670 (weak)	497-A_{1g}(weak)	528 (weak)
667-A_{1g} (strong)	718 (strong)	612-E_g (weak)	638 (weak)

Table 4.2: Raman wave numbers for iron oxides phases.

The peaks at 257 and 364 cm^{-1} cannot be assigned to the iron oxide phases. In contrast, they are strong peaks in the Raman spectra of lepidocrocite γ-FeOOH [26], which is an iron hydroxide with an orthorhombic crystal structure. This is a common product of iron oxidation mainly composed by trivalent iron oxide.
Then it could be either precursor or product of the maghemite phase usually found in magnetite NPs:

- Lepidocrocite would be grown in the core NP passivating the surface previously to the gold injection. With the presence of the gold shell, the lepidocrocite would become stable. However, it would be transformed into

maghemite in case of exposure to an open atmosphere without shell.

- Other possibility is that the lepidocrocite may be also grown from maghemite phase during the nucleation of the gold clusters by reduction of bivalent iron oxide ions around. This would explain the correlation with gold observed in Sample B.

Unfortunately, we cannot offer a better explanation with the present results. In further experiments we will try to acquire complementary data for a better knowledge of the system. Notice that lepidocrocite in an antiferromagnet, and then, its presence surrounding magnetite NPs would not be desirable in general. Also, it may be relevant thinking about catalytic applications of these NPs. Moreover, the formation of this phase could be related with the gold nucleation on the iron oxide, with relevant consequences for the optimization of synthetic routes of more complex magnetic-plasmonic composites.
Finally, and just to complete the overview, in Table 4.3 we sum up the most usual vibrational modes that we can observe in organic molecules. Some of them fit with peaks at Fig. 4.10 and 4.11.

Measured bands (cm^{-1})	Assignement
822	C-OH, C-CH and O-CH deformations
889	CH_2 rocking
1041	C-C stretching
1138	C-O stretching
1304	CH_2 deformation

Table 4.3: Raman wave numbers observed in the SERS spectra. All features that showed SERS blinking are due to the organic glycol vibration modes.

4.4 Conclusions

Different kinds of heterostructures composed by magnetite and gold NPs have been studied. We choose core-shell, dumbbell like and cross-linked structures because they correspond to different contact degree between the magnetic and the metallic constituent. By comparison between single NPs and the hetero-structures we can distinguish impact of the gold in the magnetic properties. We found insight that points that an excessive presence of gold reduces the magnetic capabilities of the resulting materials, but in good balance, it should not affect to the potential applications. The characterization is completed with SERS experiments which suggests the presence of an lepidocrocite phase. This result, really points out the potential of Raman characterization to identify iron oxide based compounds,

with a clear advantage with respect to conventional characterization techniques. Because of the technological interest on magnetite compounds, in further works, we will go in deep in order to establish the relationship between the lepidocrocite and the maghemite phase observed in conventional NPs.

Bibliography

[1] Morel, A.L.,Nikitenko, S.I., Gionnet, A., Wattiaux, J., Lai-Kee-Him, J., Chevalier, B., Deleris, G., Petibois, C., Brisson, A. and Simonoff, M. *Sonochemical approach to the synthesis of Fe_3O_4@SiO_2 core-Shell nanoparticles with tunable properties.* ACS Nano., 2, 847-856, (2008).

[2] Lim, J. and Majetich, S.A. *Surface modification of magnetite hybrid particles with carbohydrates and gold nanoparticles via 'click' chemistry.* Polym. Chem., 4, 986-995, (2013).

[3] Meledandri, C.J., Stolarczyk, J.K. and Brougham, D.F. *Hierarchical gold-decorated magnetic nanoparticle clusters with controlled size.* ACS Nano., 5, 1747-1755, (2011).

[4] Arenal, R., De Matteis, L.,Custardoy, L., Mayoral, A., Tence, M., Grazu,, V., De La Fuente, J.M., Marquina, C. and Ibarra, M.R. *Spatially-resolved EELS analysis of antibody distribution on biofunctionalized magnetic nanoparticles.* ACS Nano, 7, 4006-4013, (2013).

[5] Molina, M., Asadian-Birjand, L.,Balach, J., Bergueiro, J., Miceli, E. and Calderon, M. *Stimuli-responsive nanogel composites and their application in nanomedicine.* Chem. Soc. Rev., 44, 6161-6186, (2015).

[6] Caminale, M., Anghinolfi, L., Magnano, E., Bondino, F., Canepa, M., Mattera, L. and Bisio, F. *Tuning the magneto-optical response of iron oxide nanocrystals in Au- and Ag-based plasmonic media.* ACS Appl. Mater. Interfaces., 5, 1955-1960, (2013).

[7] Wang, H.X., Zuo, Z.Q.,Du, J.Z., Wang, Y.C., Sun, R., Cao, Z.T., Ye, X.D., Wang, J.L., Leong, K.W. and Wang, J. *Surface charge critically affects tumor penetration and therapeutic efficacy of cancer nanomedicines.* Nano Today, 11, 133-144, (2016).

[8] Abraçado, L.G., Esquivel, D.M.S., Alves, O.C. and Wajnberg, E. *Magnetic material in head, thorax, and abdomen of Solenopsis substituta ants: A ferromagnetic resonance study.* J. Magn. Reson., 175, 309-316, (2005).

[9] Lacava, L.M., Lacava, Z.G.,Da Silva, M.F., Silva, O., Chaves, S.B., Azevedo, R.B., Pelegrini, F., Buske, N., Sabolovic, D. and

Morais, P.C. *Magnetic resonance of a dextran-coated magnetic fluid intravenously administered in mice.* Biophys. J., 80, 2483-2486, (2001).

[10] Wang, L., Luo, J.,Fan, Q., Suzuki, M., Suzuki, I.S., Engelhard, M.H., Lin, Y., Kim, N., Wang, J.Q. and Zhong, C.J. *Monodispersed core-shell Fe_3O_4@Au nanoparticles.* J. Phys. Chem.B., 109, (2005).

[11] Yu, H., Chen, M., Rice, P.M., Wang, S.X., White, R.L. and Sun, S. *Dumbbell-like bifunctional Au-Fe_3O_4 nanoparticles.* Nano Lett., 5, 379-382, (2005).

[12] Xu, Z., Shen, C. ,Hou, Y., Gao, H. and Sun, S. *Oleylamine as both reducing agent and stabilizer in a facile synthesis of magnetite nanoparticles.* Chem. Mater., 21, 1778-1780, (2009).

[13] Wang, M., Wang, C., Young, K.L., Hao, L., Medved, M., Rajh, T., Fry, H.C., Zhu, L., Karczmar, G.S., Watson, C., Jiang, J.S.Markovic, N.M. and Stamenkovic, V.R. *Cross-linked heterogeneous nanoparticles as bifunctional probe.* Chem. Mater., 24, 2423-2425, (2012).

[14] Aharoni, A. *Introduction to the Theory of Ferromagnetism.* second ed., Clarendon Press, New York, (2007).

[15] Sun, S., Zeng, H., Robinson, D.B., Raoux, S., Rice, P.M., Wang, S.X. and Li, G. *Monodisperse MFe_2O_4 (M = Fe, Co, Mn) Nanoparticles.* J. Am. Chem. Soc., 126, 273-279, (2003).

[16] Upadhyay, S., Parekh, K. and Pandey, B. *Influence of crystallite size on the magnetic properties of Fe_3O_4 nanoparticles.* J. Alloys Compd., 678, 478-485, (2016).

[17] Woo, K., Hong, J., Choi, S., Lee, H., Ahn, J., Kim, C.S. and Lee, S.W. *Easy Synthesis and Magnetic Properties of Iron Oxide Nanoparticles.* Chem. Mater., 16, 2814-2818, (2004).

[18] Leslie-Pelecky, D.L. and Rieke, R.D. *Magnetic Properties of Nanostructured Materials.* Chem. Mater., 8, 1770-1783, (1996).

[19] Maity, D., Kale, S.N., Kaul-Ghanekar, R., Xue, J.M. and Ding, J. *Studies of magnetite nanoparticles synthesized by thermal decomposition of iron (III) acetylacetonate in tri(ethylene glycol).* J. Magn. Magn. Mater., 321, 3093-3098, (2009).

[20] Kim,D.K., Zhang, Y., Voit, W., Rao, K.V. and Muhammed, M. *Synthesis and characterization of surfactant-coated superparamagnetic monodispersed iron oxide nanoparticles.* J. Magn. Mater., 225, 30-36, (2001).

[21] Grady, K.O., Blanco-Mantecón, M., O'Grady, K., Quidant, R., Monneret, S., J. Polleux, J. and Rigneault, H. *Grain size and blocking distributions in fine particle iron oxide nanoparticles.* J. Magn. Magn. Mater., 203, 50-53, (1999).

[22] Carrey, J., Mehdaoui, B. and Respaud, M. *Simple models for dynamic hysteresis loop calculations of magnetic single-domain nanoparticles: Application to magnetic hyperthermia optimization.* J. Appl. Phys., 109, (2011).

[23] Goya, G.F., Berquó, T.S., Fonseca, F.C. and Morales, M.P. *Static and dynamic magnetic properties of spherical magnetite nanoparticles.* J. Appl. Phys., 94, 3520-3528, (2003).

[24] Caldarola, M., Albella, P., Cortés, E., Rahmani, M., Roschuk, T., Grinblat, G., Oulton, R.F., Bragas, A.V. and Maier, S.A. *Non-plasmonic nanoantennas for surface enhanced spectroscopies with ultra-low heat conversion.* Nat. Comm. 6, 7915, (2015).

[25] Cornell, R. M. and Schwertmann, U.*The iron oxides*Wiley-VCH GmbH Co. KGaA, (2003).

[26] Faria, D.L., Venancio Silva, S.and Oliveira, M.T., *Raman microescpectroscopy of some Iron Oxides and Oxyhydroxides.* J. Raman Spectrosc., 28, 873-878, (1997).

Chapter 5

Raman spectroscopy for the study of Spin-Crossover in iron Fe^{2+}/Fe^{3+} complexes

Certain metal complexes, under the application of an external perturbation exhibits a spin state variation. This effect is known as spin crossover. Spin crossover in molecular complexes are often induced by a variation of the temperature, pressure or irradiation even an external magnetic field can also produce these spin crossover. In most cases, this effect is assisted by lattice potential variations due to the above mentioned external stimulus. The explanation of the lattice dynamics is found in the energy vs field strength curves, illustrated by means of the Tanabe-Sugano and related diagrams (Fig. 5.1), [1]. In the next we are going to show how to deal with this phenomena in Fe^{2+} based compounds. The samples used for our studies have been provided by the UIMM at ICMol.

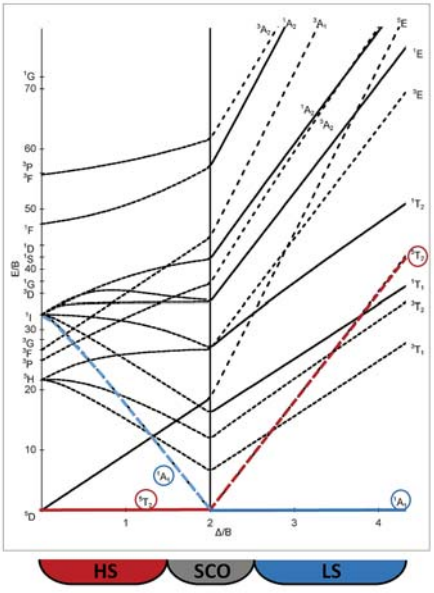

Figure 5.1: Tanabe-Sugano diagram for d^6 ions (Fe^{2+}). The $^5T_{2g}$ and $^1A_{1g}$ spin states shown in red and blue respectively. Figure adapted from [2].

5.1 Introduction

For certain transition metals we can describe the impact of external stimuli on the lattice potential. This way we can figure out the energy splitting on the corresponding d orbitals. In the case of Fe^{2+}, the lattice potential affects to the energy splitting between e_g and t_{2g}. Usually, it is energetically more favorable to obtain d^6 ions (like Fe^{+2}) in the low spin configuration (LS), since this configuration is favored because of the lower pairing energy. This is, thanks to the energy reduction electrons paired the LS state presents a maximum in ligand field [3]. However, in some circumstances, as for example in the case of larger Fe^{2+} ion, ligand fields might be considerable reduced. Then, the energy of the spin pairing cannot compensate the ligand field. In this situation the high spin (HS) configuration becomes more stable.
The energy balance in that kind of complexes can be roughly described by thermodynamic considerations in terms of the enthalpy and Gibbs potential. The crossover if expected to occur when the enthalpy of the LS state (usually the more stable) is varied to favor electronic occupation in the HS configuration, see Fig. 5.2.

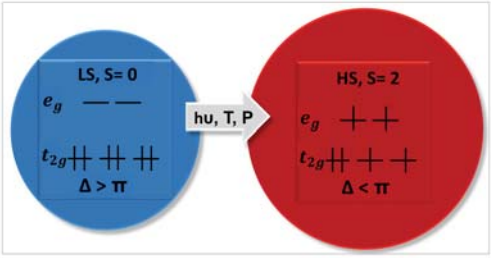

Figure 5.2: Relative volumes of HS and LS states with the $3d^6$ configuration of Fe^{2+} in an octahedral field. The larger HS volume is due to the occupation of antibonding e_g^* orbitals. Electronic transition for ground state T_{2g} to excited state e_g for a d^6 electron configuration (Δ) is the ligand-field splitting and Π is the electron pairing energy).

This is, in front of a temperature increase, the HS state sometimes becomes the thermodynamically stable state. The reason is that, the entropy of the HS state, as depicted in Fig. 5.2, is larger and then statistically favored at high temperatures.

$$\Delta G = \Delta H - T\Delta S < 0 \tag{5.1}$$

In SCO iron compounds the Fe^{2+} ion is located in octahedral configurations, then, the 3d orbitals are splitted. The LS state arises from the close-shell t_{2g}^6 electronic configuration (blue left panel in Fig. 5.2) while the HS state comes from the $t_{2g}^4 e_g^2$ electronic configuration (right red panel in Fig. 5.2). This is, in the HS state the antibonding levels (e_g) are doubly occupied, which results in a

lengthening of the Fe-ligand bonds [1].
Then, the SCO involves transferring electrons from the t_{2g} subshell to the e_g subshell. Because of the SCO is an intrinsic phenomenon, closely related with the lattice potential and with an impact in the electronic orbital filling; the variation of the spin state really affects to the properties of the material. First, we can observe changes in the metal-donor atom distance, as a result of a change in relative occupancies of the t_{2g} and e_g orbitals. This can be clearly observed by means of structural characterization techniques. Also Raman spectroscopy results very useful to identify the spin state in iron compounds. On the other hand, the magnetic and optical properties of those materials present important differences from LS to HS. Magnetism can be monitored at the SQUID, as the change from low to high spin occurs the magnetization is increased. The dynamics should describe an diamagnetic to paramagnetic transition. Also changes in the refractive index or in the absorption spectra of SCO materials have been observed [2].
Spin transition curves are a common representation of SCO phenomenon and they are usually obtained from a plot of high spin fraction χ_{HS}T vs temperature. Optical measurements would be out of the scope of this work. In the experimental data acquired from macroscopic samples, e.g. microcrystals or NP ensembles, we can expect the presence of different phase clusters, aggregates or even magnetic domains. The degree of cooperativity among the different magnetic or crystallographic constituents will determine the nature of the spin transition. Sometimes the system also presents thermal hysteresis. All this features are of technological interest because of it enables the bistability on the system (memory effect). This technological potential of the SCO compounds could be exploited for application in further memory devices [4] and it is the reason of the recent research in the area. Applications will vary depending on the properties of the transition. For example, storage devices will require really stable magnetization states with large hysteresis curves. In contrast, the readout speed in smart displays would require an abrupt sweep from LS to HS state, and viceversa. In a similar way to the coercivity curves, the temperature at which two states (of different spin multiplicity) are present in 50% ($T^{\uparrow}_{1/2}$ and $T^{\downarrow}_{1/2}$) is known as spin transition temperature[1].

[1] If this transition is incomplete, in either the low temperature region (residual HS fraction) or the high temperature region (residual LS fraction), or both, the spin transition temperature can be defined as the temperature at which 50% of the SCO-active complex molecules have changed their spin state.

5.1.1 The electronic structure picture in bivalent iron ions.

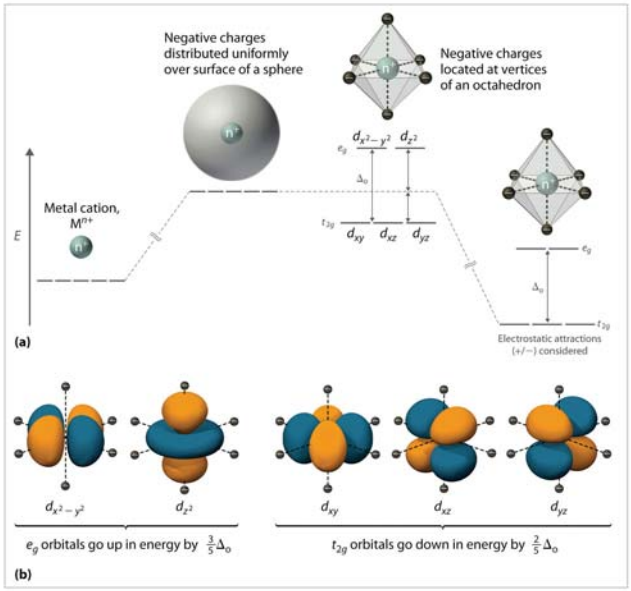

Figure 5.3: (a) Effect on the relative energy of the d orbitals placing a transition metal ion into an octahedral (O_h) ligand field (Δ_{O_h}), (b) Orientation of the d orbitals of a transition metal to a Cartesian coordinate system. Figure extracted from [5].

In an octahedral metal complex, when ligands approaches towards the transition metal, the ion modifies the energy of the orbitals splitting into two subsets irreducible representations: e_g and t_{2g} [6]. When ligands are oriented along the x-, y- and z-axes, the d_{xy}, d_{xz} and d_{yz} orbitals (t_{2g}) decreases in energy, at the same time that the $d_{x^2y^2}$ and d_{z^2} orbitals (e_g) increases in energy because of the electron-electron repulsion (Fig. 5.3 a)). The energy gap between the e_g and t_{2g} subsets is known as ligand field splitting, Δ, and its magnitude depends on the type and oxidation state of the metal as well as the nature of the ligands and on metal-ligand distance [2]. The occupation of the d orbitals is dependent on Δ and the energy released when spin-pairing electrons (Π), the pairing energy mentioned before. When $\Delta < \Pi$, the d orbitals in both t_{2g} and e_g sets will become singly occupied prior to spin-pairing of electrons within the same orbital, according to Hund's Rules. If $\Delta > \Pi$, the electrons will fill the d orbitals according to the Aufbau Principle, which means that the lower energy t_{2g} subset will be completely filled before filling the higher energy e_g levels.
In the Fe^{2+} compounds we can often find the $\Delta \approx \Pi$. For this reason, external perturbations easily can enable switching between the diamagnetic low spin LS ($t_{2g}^6 e_g^0$) and the paramagnetic high spin HS ($t_{2g}^4 e_g^2$) electronic configurations.

In the next sections we are going to show how to monitor this phenomenon by means of Raman spectroscopy or through magnetic susceptibility measurements. During last years, we have studied several SCO systems. In most of them, Raman spectroscopy has been useful to complete material characterization, since it clearly offers relevant information about the spin state by monitoring the evolution of the iron ion bound length. In the next sections, we are going to show two particular cases where the use of Raman spectroscopy have been really valuable. These are molecular NPs and microcrystals. In both cases, characterization techniques available to complete magnetic measurements would require to spend large material amount.

5.2 Triazol nanoparticles (Spin-crossover complex containing Fe^{2+})

5.2.1 Experimental section

In this sections we are going to show how Raman can be used to observe changes in the spectra during the spin crossover. Particularly interesting are triazol based NPs because SCO phenomenon confers them bistability at room temperature and this confers them desirable properties for using as storage or memory devices. Here we present two examples, $[Fe(Htrz)(trz)](ClO_4)$ and $[Fe(Htrz)_2(NH_2trz)](BF_4)$ (from now Sample A and B). We chose these particular examples because we want to study the ligand effect by Raman, being our aim to illustrate how the ligand vibrations affect to the spectra. The NPs have been synthesize by Mónica Giménez-Marqués from the UIMM at ICMol. We will show the spin crossover phenomenon on powders of NPs. Currently, we are reproducing those experiments on a surface. Preliminary results points that the NP aggregates preserve the crossover properties in diluted dispersion. More details about these NPs can be found at [2]. This compound $[Fe(Htrz)_2(trz)](ClO_4)$ (Htrz = 1,2,4-triazole and trz^- = triazolate), belongs to the family of polymeric one-dimensional (1D) SCO compounds of general formula $[Fe(Rtrz)_3](A)_2$ (R = 4-substituted-4H-1,2,4-triazole and A = monovalent anion).
It is particularly interesting, because it presents an abrupt spin transition centered above room temperature ($T^{\uparrow}_{1/2}$ = 391 K and $T^{\downarrow}_{1/2}$ = 349 K) with a remarkable hysteresis loop of $\Delta T = 42$ K, in bulk [7]. Its structure in an octahedral surrounding of the Fe^{2+}, it is formed by two triazole and one triazolate ligands in a C_{2v} symmetry and it is charge balanced with a ClO_4^- anion [7, 8]. Recent X-ray powder diffraction (XRPD) study on $[Fe(Htrz)_2(trz)](ClO_4)$ led to a first structural hypothesis for both the HS and the LS species [9, 10].

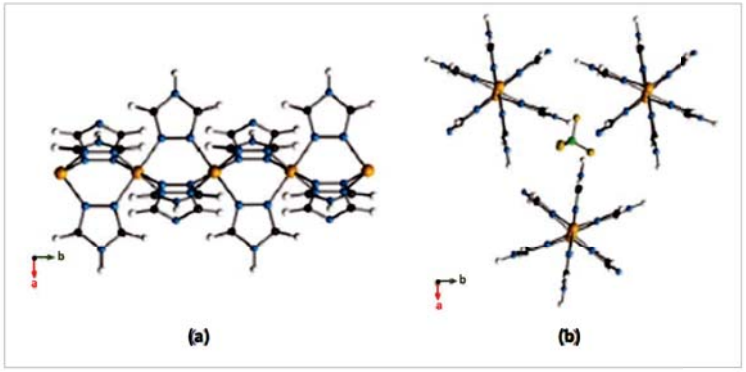

Figure 5.4: (a) Cationic chains of $[Fe(Htrz)_2(trz)](ClO_4)$ with Fe^{2+} aligned parallel along the b axis with the three bridging triazoles in alternating invert positions (ClO_4^- anions are omitted for clarity). (b) BF_4^- anion cavities in the crystal packing of $[Fe(Htrz)_2(trz)](ClO_4)$. Figure courtesy of Mónica Giménez.

Polymeric chains of Fe^{2+} ions situated along the b axis with the three bridging triazoles in alternating invert positions are the base of the crystal structure with two Htrz ligands and one trz^- ligand (Fig. 5.4 a)), giving the formula $[Fe^{2+}(Htrz)_2(trz^-)](ClO_4^-)$ (Pnma space group). It can be found each ClO_4^- ion located in cavities formed by the triazole ligands (Fig. 5.4 b)) and no water molecules are found within the crystal structure. The distance between two next iron centres within a chain is half of the b parameter. Each $[Fe(Htrz)_2(trz)]_n$ chain is surrounded by six identical chains with two different Fe$\cdots$Fe interchain distances [2]. This structural study confirms a chain architecture formed by $[Fe(Htrz)_2(trz)]_n$ chains and connected through short N-H$\cdots$N contacts. Therefore, the unusually abrupt transition and large hysteresis of 40 K above room temperatures is consequently ascribed to this structural characterization. Descriptions and magnetic measurement of this kind of NPs can be found in [11].
Studies carried out by Coronado et al. showed that the magnetic hysteresis of Sample A NPs can be tuned with modifications of the chemical composition [12,13] based on the concept of molecular alloy proposed by Kahn which drives to a family of coordination polymers of general formula $[Fe(Htrz)_{3-3x}(NH_2trz)_{3x}](BF_4)_2$. The resulting compound will show a variable transition temperature in the bulk, depending on the composition [14].
Using this strategy NPS with bi-stability closer to room temperature can be obtained. For example, the ligand can be replaced to promote minor changes in the chemical composition ($0.016 < x < 0.1$). The thermal hysteresis from a series of samples is demonstrated to move to lower temperatures as the ratio of aminotriazole increases.
Raman spectroscopy is of great interest since it allows to reproduce the hysteresis loops ($\chi_M T$ vs T curve) saving a great amount of time. Other advantage

of the Raman spectrocopy is that the crossover can be monitored on really small samples, less than 1 microgram. While magnetic measurements would require few milligrams to obtain trustable data. This will be demonstrated in the next section during the study of microcrystals. Importantly, our results suggest the possibility of characterization of spin states in isolated NPs, as the first step towards the optical readout of single magnet memories.

5.2.2 Results and discussion

Magnetic and optical characterization of the NP under investigation can be found in [2]. Both kinds of NPs present similar behavior with a narrow transition from LS to HS as the temperature is increased, see table 5.1. This data are extracted from the thermal dependence of $\chi_M T$ for both thermal spin transitions are indicated as, $T^{\uparrow}_{1/2}$ and $T^{\downarrow}_{1/2}$ while ΔT represents the hysteresis width that appears in all the spin transitions. It is worth to mention that, for the NPs studied at our group, the crossover properties (e.g. ΔT) does not differ to much from the bulk values. Obviously, the hysteresis and transition temperature can be slightly tuned by changing the NP size but the main control is done through the ligand. For this reason, in this section we did not pay attention to the NP size. Just to complete information we have got average sizes of 4 and 10 nm for Samples A and B respectively.

	Bulk A	Sample A	Bulk B	Sample B
$T^{\uparrow}_{1/2}$	391	373	313	315
$T^{\downarrow}_{1/2}$	349	343	296	305
ΔT	42	30	17	10

Table 5.1: Physical characteristics of the thermal spin transition $T^{\uparrow}_{1/2}$ and $T^{\downarrow}_{1/2}$ for both samples and bulk. Data courtesy of Mónica Giménez

NPs of Sample A exhibit a reduced hysteresis loop of 30 K ($T^{\uparrow}_{1/2}$ = 373 K and $T^{\downarrow}_{1/2}$ = 343 K). Typically for these nanostructured chain compounds it can be ascribed to the different coordination environment of the terminal Fe^{2+} in the chains, coordinated to oxygen atoms from water ligands instead of the nitrogen atoms of the triazole ligand.
In the case of the Sample B the transition is centered closer to room temperature, with a narrower hysteresis of 10 K ($T^{\uparrow}_{1/2}$ = 315 K and $T^{\downarrow}_{1/2}$ = 305 K)).

Raman spectroscopy

As aforementioned, the transition from high to low spin is accompanied by the reduction (for d^6 species a total reduction) of charge in the antibonding e_g orbitals towards t_{2g} orbitals [1]. Vibrational modes will be affected because of the change in the metal-ligand bond distance (M-L) between the HS and LS state. This will also affect the Fe-N streching mode of the Fe^{2+}, as will be shown below. This can be observed in the vibrational spectrum in the region of ~ 250 cm^{-1} (sometimes at ~ 500 cm^{-1}) where the stretching frequencies of transition metal compounds is usually expected [15].
As the temperature is modified, the vibrational bands belonging to the HS and LS species can be easily recognized as relevant vibrational mode signatures decreasing or increasing in intensity, respectively.
Given the structural complexity of the studied systems (i.e. the presence of multiple organic ligands, triply bridging between two metal centers at a time, forming chains of unknown length) complete assignment of their solid-state Raman spectra would be challenging, and sometimes out of the scope of this work. Then, to simplify the problem we focused on the structural changes that occur in the Fe-N_6 coordination sphere during spin transition. Also we identified internal modes of the NH_2-trz and Htrz rings or the modes of the non-coordinating counter anions, however, no special attention is paid to those modes since the thermal hysteresis loop is clearly monitored by the Fe-N stretching modes.
For the characterization we have used the 514.5 nm line of the Ar ion laser. In order to avoid laser heating in our samples, low power has been used during the experiment (7.8 mW) and it has been necessary to wait 1 min between shots. During the temperature sweep we have wait 10 minutes after each temperature step to guaranty the acquisition stability. In Fig. 5.6 we show the evolution of the Raman spectra of the Sample A with the temperature. Roughly speaking, we have observed two peaks (242 and 285 cm^{-1}) that disappears after heating the sample at 383 K. The peaks come back when cooling down the sample, see Fig. 5.7. Raman spectra clearly show the difference between LS and HS states as corroborates previous magnetic measurements.
This feature is a well-known and extensively reported signature of the spin crossover [16]. About the peaks observed they are assigned to the Fe-N stretching and Fe-N-Fe bending vibration modes and therefore related with the state of the Fe^{2+} ion. We can estimate the $T^{\downarrow}_{1/2}$ cooling and $T^{\uparrow}_{1/2}$ heating temperatures as the point where the Raman peak reduces its integrated intensity to a half. This is, $T^{\uparrow}_{1/2}$ heating would be around 353 K while the $T^{\downarrow}_{1/2}$ cooling 333 K. This means a ΔT value of 20 K which is similar to the one extracted from magnetic

measurements [17].

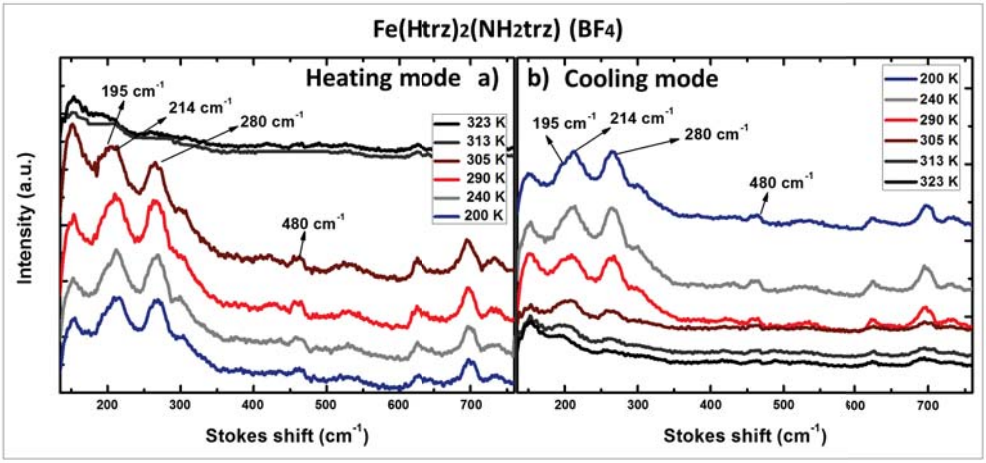

Figure 5.5: a) $[Fe(Htrz)_2(trz)](ClO_4)$ Raman spectra while heating from 150 to 363 K (using 514.5 nm excitation). To avoid laser cooling we waited 1 min between shots; b) $[Fe(Htrz)_2(trz)](ClO_4)$ Raman spectra while cooling the temperature from 353 K to 150 K (using 514.5 nm excitation). To avoid laser heating we waited 1 min between shots.

Even at different temperature and presenting narrower hysteresis the behavior of the Sample B is qualitatively similar. However, Raman spectra suggest that at room temperature this sample is in HS. Then we need to cool the sample down to observe the spin transition. In this sample we have observed the motion of several peaks. Mainly the mode at 195 cm^{-1} can be associated to angle bending, δ(N-Fe-N) of the bridge and modes at 214, 280 cm^{-1} can be associated to de Fe-N stretching modes as Smit et al. proposed for similar compounds [18]. We have also identified the presence of other peaks, for example a weak mode at around 460 cm^{-1}. Even the assign of that modes will be difficult with the structural data in literature, but their correlation with the crossover is clear. This is relevant in the sense that we may monitor the crossover without the need of spending time on the peak assignment. This will be an advantage in the characterization of macromolecular compounds, since we may found spin crossover signatures far from the Fe^{2+} coordination sphere. In a similar way, in the next section we demonstrate the spin state can be monitored via the dynamics of the vibrational modes of the ligand.

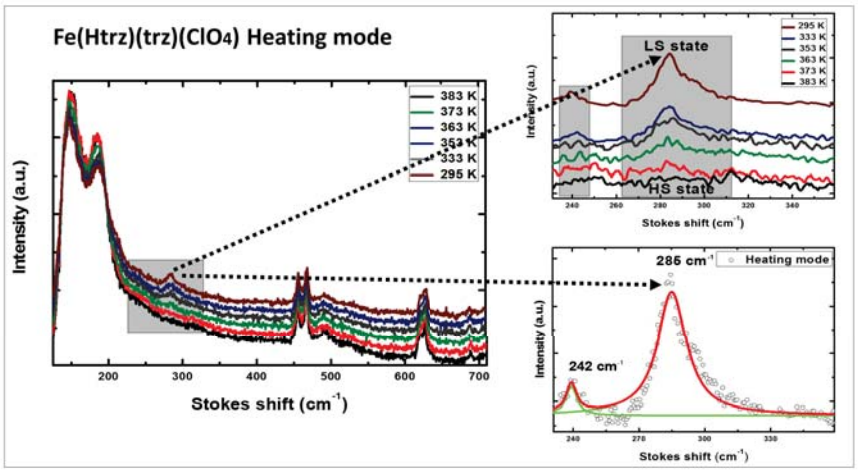

Figure 5.6: $[Fe(Htrz)_2(NH_2trz)](BF_4)$ Raman spectra while heating from to 295 to 383 K (using 514.5 nm excitation), showing the experimentally observed data and the Lorentzian fit for the individual peaks. Full curve: total fitted spectrum, green curves: individual fitted peaks. To avoid laser heating we waited 1 min between shots.

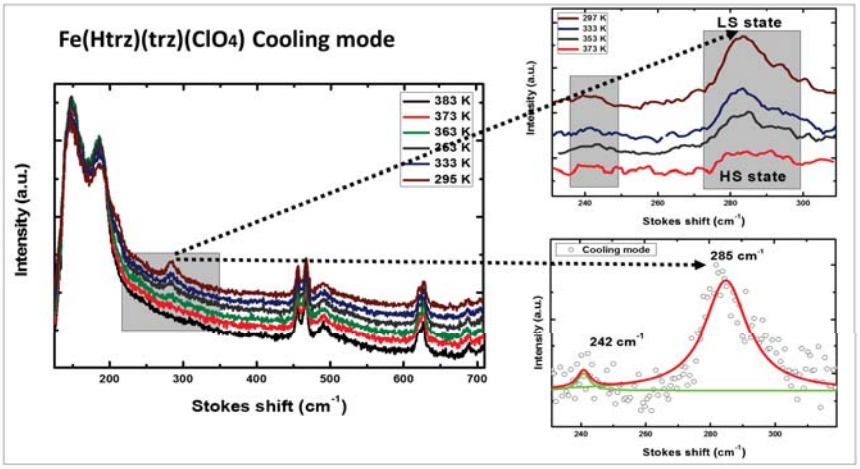

Figure 5.7: $[Fe(Htrz)_2(NH_2trz)](BF_4)$ Raman spectra while cooling the temperature from 383 K to 297 K (using 514.5 nm excitation), showing the experimentally observed data and the Lorentzian fit for the individual peaks. Full curve: total fitted spectrum, green curves: individual fitted peaks. To avoid laser heating we waited 1 min between shots.

5.3 Phase identification in single crystal of Fe^{2+} and Fe^{3+} compounds by means of Raman spectroscopy

In this section we characterize single crystals of $[Fe_3^{3+}(\mu_3\text{-}O)(H_2O)_3[Fe^{2+}(bppCOOH)\ (bppCOO)]_6\text{-}(ClO_4)_{13}\cdot((CH_3)_2CO)_6]\cdot(solvate)$ (2), a secondary product in the synthesis of $[Fe^{2+}((bppCOOH)_2](ClO_4)$ (1) [19].

The bis-chelated iron (II) complexes of the tridentate ligands of the 2,6-bis(pyrazol-1-yl)pyridine(1-bpp) family (Fig. 5.8) have been extensively studied because the spin transitions in these materials are usually very abrupt and take place with a thermal hysteresis close to room temperature [20].

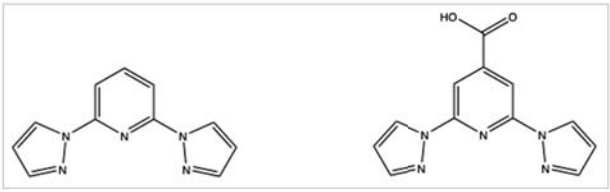

Figure 5.8: Molecular Structures of 1-bpp (Left) and bppCOOH (Right) ligands. Figure extracted from [19].

SCO compounds of $1-bpp$ derivatives with a variety of different functionalities can be found in literature [21–26]. The interest on $[Fe(1\text{-bpp})_2]^{2+}$ salts is motivated by the rich phenomenology found in the corresponding derivated compounds, with demonstrated capabilities such as a light-induced excited spin state trapping (LIESST) effect [27] at high temperatures [28].
In a previous work [19], a carboxylate group was added to this ligand (bppCOOH; see Fig. 5.8) to prepare the mononuclear $[Fe^{+2}(bppCOOH)_2](ClO_4)_2$ (1) compound. This compound showed an abrupt spin transition close to 380 K attributed to the presence of a hydrogen-bonded linear network. $[Fe_3^{3+}(\mu_3\text{-}O)\text{-}(H_2O)_3[Fe^{2+}(bppCOOH)(bppCOO)]_6](ClO_4)_{13}\cdot(CH_3)_2(CO)_6\cdot$ (solvate) (2), is a nonanuclear complex that has been obtained as a secondary product in the synthesis of (1). The single-crystal X-ray diffraction structure of (2) shows that it contains the nonanuclear cluster of the formula $[Fe_3^{3+}(\mu_3\text{-}O)(H_2O)_3[Fe^{2+}((bppCOOH)(bppCOO)]_6]^{13+}$, which is formed by a central $Fe_3^{3+}O$ core coordinated to six partially deprotonated $[Fe^{2+}((bppCOOH)(bppCOO)]^+$ complexes [29]. Raman spectroscopy studies on single crystals of (1) and (2) have been performed to elucidate the spin and oxidation states of iron ions (2). Our studies indicates that most of the Fe^{2+} complexes of (2) remained in the low-spin (LS) state and present a gradual and incomplete spin crossover above 300 K.

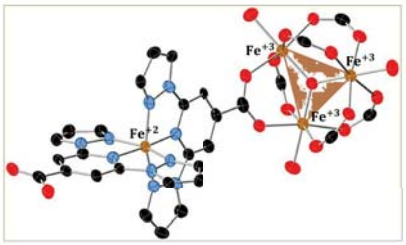

Figure 5.9: Fe^{3+} trimer structure (Fe in yellow), see the triangular zone. More details about the structure can be found in [29].

This conclusions are in agreement with magnetic characterization. On the other hand, the Fe^{3+} trimer showed the expected antiferromagnetic behavior (see Fig. 5.9).

5.3.1 Experimental section

The compound (2) has been synthesized adding a solution of $Fe(ClO_4)_2{\cdot}6H_2O$ in acetone to a solution of bppCOOH in acetone, the mixture has been stirred for 15 min. Crystals suitable for X-ray diffraction has been obtained by the slow diffusion of diethyl ether into this solution. Red prismatic crystals of (1) and red needles of (2) were obtained after a few weeks, collected, and separated manually. The yield of (2) is close to 5%.

	250 K	120 K
formula	$C_{162}H_{138}Cl_8Fe_9N_{60}O_{66}$	$C_{162}H_{138}Cl_8Fe_9N_{60}O_{66}$
M_R	4767.57	4767.57
cryst size/mm	0.25×0.06×0.04	0.25×0.06×0.04
T/K	250	120
cryst system	hexagonal	hexagonal
space group	$P6_3/m$	$P6_3/m$
a/Å	18.1136(10)	18.1644(6)
c/Å	47.919(2)	48.1237(10)
α/deg	90	90
γ/deg	120	120
$V/Å^3$	13616.1(16)	13750.9(10)
Z	2	2
$\rho_{calc}/g.cm^{-3}$	1.163	1.151
$\mu(M_oK\alpha/mm^{-1})$	0.618	0.612
reflns collected	100908	79824
indep reflns	4286	5140
$R1(F)^{\alpha}$, $I < 2\sigma(I)$	0.0891	0.0672
$wR2(F^2)^b$, all data	0.3268	0.2664

Table 5.2: Crystallographic Data for Compound 2 at 120 and 250 K (with ${}^aR = \sum \parallel F_o \mid - \mid F_c \parallel / \sum \mid F_o \mid$ and ${}^bR_w = \{\sum[w(\mid F_o \mid - \mid F_c \mid)]^2 / \sum[w \mid F_o \mid]^2\}^{1/2}$) [29].

For the structural characterization, X-ray data of single crystals of (2) were acquired at 120 and 250 K. A summary of the data collection and structure refinements is provided in table 5.2. The structure of (2) is shown in Fig. 5.10.

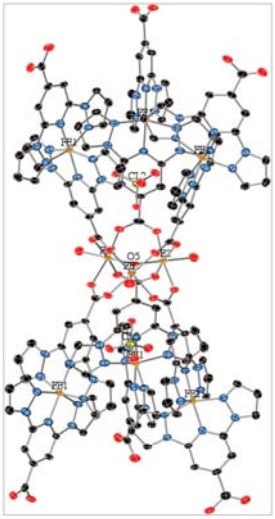

Figure 5.10: X-ray structure of the complex $[Fe_3^{3+}O\text{-}(H_2O)_3(Fe^{2+}(bppCOOH)\ (bppCOO))_6]^{13+}$ in the structure of (2) with ClO_4^- with central atom Cl2. Color code: C, black; N, blue; O, red; Cl, yellow; Fe, brown. H atom have been omitted for clarity.

We can distinguish a nonanuclear cluster with a central $Fe_3^{3+}O$(oxo) coordinated to six $[Fe^{2+}$(bppCOOH)-(bppCOO)$]^+$ complexes. Compound (2) crystallizes in a hexagonal crystal with centrosymmetric space group $P6_3/m$. The structure of a single crystal of (2) was solved at 120 and 250 K [29]. It contains the nonanuclear cluster $[Fe_3^{3+}(\mu_3\text{-O})(H_2O)_3[Fe^{2+}$(bppCOOH)-(bppCOO)$]_6]^{13+}$ surrounded by ClO_4^- anions, acetone, and disordered solvent molecules. This cluster is formed by a central $Fe_3^{3+}O$(oxo) core coordinated to six $[Fe^{3+}$(bppCOOH)-(bppCOO)$]^+$ complexes through the carboxylate groups. The central μ_3-O group lies on a 3-fold axis and the whole molecule presents trigonal symmetry.
The coordination site around Fe^{3+} is a distorted octahedron in which the four equatorial positions are occupied by O atoms from four bridging carboxylate groups, while the two axial positions are occupied by the central μ_3-O group and one terminal water molecule. The Fe-O bond distances to the trifurcated oxo ligand and the bridging carboxylate ligands are within the ranges observed for other triiron (III) derivatives [30]. Bond-valence-sum calculations confirm the +3 oxidation state of the central $Fe_3^{3+}O$(oxo) core [31]. There is one crystallographically independent $[Fe^{2+}$(bppCOOH)(bppCOO)$]^+$ complex with the Fe^{2+} ion (Fe1) coordinated to the central $Fe_3^{3+}(\mu_3\text{-O})(H_2O)_3$ core. They generate the six $[Fe^{2+}$(bppCOOH)(bppCOO)$]^+$ complexes from the cluster through the central C_3 axis. The terminal carboxylate group, which is not coordinated to the Fe^{3+} trimer, presents two 3 different CO distances, corresponding to the carbonyl C=O end and to the alcoholic C-OH end. Furthermore, it forms a hydrogen bond with

the carbonyl group of an acetone molecule. On the contrary, the opposite carboxylate group is coordinated to a Fe^{3+} ion from the central trimer and presents very similar CO distances. This suggests that this carboxylate group is deprotonated, as in other basic carboxylates. The Fe^{2+} ion (Fe1) is coordinated to one bppCOOH ligand and one $bppCOO^-$ ligand with Fe-N bond lengths typical of a LS configuration (in the range of those observed in (1) [19]).

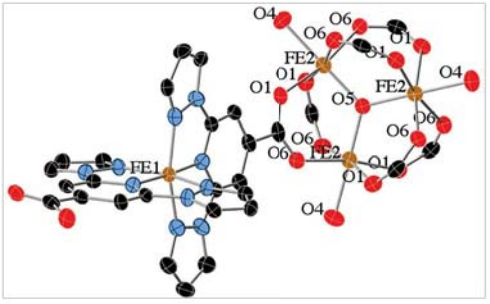

Figure 5.11: X-ray structure of the $[Fe_3^{3+}(\mu_3\text{-}O)(H_2O)_3]^{7+}$ core and one of the six coordinated $[Fe^{2+}(bppCOOH)(bppCOO)]^+$ complexes of the $[Fe_3^{3+}O(H_2O)_3(Fe^{2+}$ (bppCOOH) $(bppCOO))_6]^{13+}$ cluster (2). Color code: C, black; N, blue; O, red; Fe, brown. H atoms have been omitted for clarity.

There are two crystallographically independent ClO_4^- anions. One of them has the central Cl atom (Cl2) placed in the two cavities described by the central Fe_3^{3+} trimer and the three $[Fe^{2+}(bppCOOH)(bppCOO)]^+$ complexes (Fig. 5.10). The second one has the central atom (Cl1) occupying the holes between the $[Fe_3^{3+}(\mu_3\text{-}O)(H_2O)_3[Fe^{+2}(bppCOOH)\text{-}(bppCOO)]_6]^{13+}$ cations. There is one crystallographically independent acetone molecule, which forms a hydrogen bond with the terminal carboxylate groups from the nonanuclear cluster, as mentioned above. Finally, this structure presents several pores that are occupied by disordered ClO_4^- anions and acetone molecules.

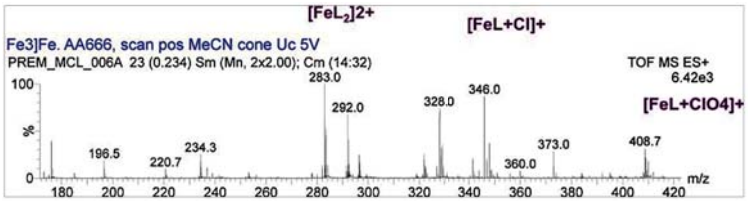

Figure 5.12: ESI-MS of acetonitrile solutions of compound (2) recorded at U_c = 5 V. The assignment of the three most intense peaks is indicated. L is bppCOOH. A total of three scans were collected at room temperature in the 2θ range 5-40°.

Powder X-ray diffraction of (2) shows the presence of broad peaks and important differences with the simulated pattern calculated from the structure at 250 K, not shown. This consistent with the above mentioned loss of solvent molecules and crystallinity. The behavior of the polynuclear Fe9 cationic cluster of (2) in

solution has been characterized by ESI-MS. Fig. 5.12 shows the ESI-MS (positive mode) analysis of a solution of (2) in acetonitrile.
The two most intense peaks appear at values of m/z 283.0 and 565.1, which correspond respectively to species $[Fe^{2+}(bppCOOH)_2]^{2+}$ and $[Fe^{2+}(bppCOOH)(bppCOO)]^{+}$, this means a massive presence of those species in solution where we can conclude that the stability of the cluster is not preserved in solution.

5.3.2 Results and discussion

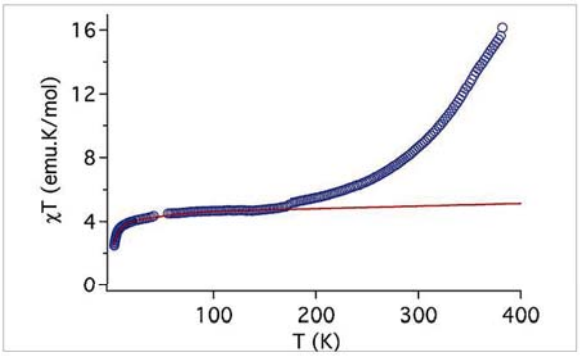

Figure 5.13: Thermal variation of χ_MT for (2). The solid line is the best fit of the 2-200 K data.

We are going to characterize magnetically (2) with the aim to find the thermal dependence of the product of the molar magnetic susceptibility times on the temperature (μ_MT), see Fig. 5.13. It is observed that (μ_MT) rises up from 2 to 300 K, with a sudden increase from 2 to 20 K. The increase continues in a more gradual way from 20 to 250 K. This is reflected in the variation of the μ_MT values at 2 K (1.9 emu·K·mol^{-1}) and at 20 K (3.3 emu·K·mol^{-1}). The curve reduces its slope after 20 K and it looks almost constant above 60 K ($<$ 5 emu·K·mol^{-1} at 200 K).
The evolution of the susceptibility with the temperature is in agreement with the structures solved above. Remember that the Fe-N distances in the structures solved at 120-250 K indicate the six $[Fe^{2+}(bppCOOH)(bppCOO)]^{+}$ and are in the LS state (diamagnetic). The only contribution to the magnetization may come from the $[Fe_3^{3+}(\mu_3\text{-O})(OH_2)_3]^{7+}$ trimer, at 250 K. However, the (μ_MT) value at 250 K (5.4 emu·K·mol^{-1})is significantly lower than that theoretically expected for three noninteracting HS Fe^{3+} ions (13.13 emu·K·mol^{-1}). Clemente et al. [29] attributed this deviation to intratrimer antiferromagnetic interactions between the Fe^{3+} centres linked by μ-O that would give rise to a ground state with S = 1/2. The conclusion is that the observed magnetism can not be due

to this Fe^{3+} trimer. This suggests the presence of a small fraction of Fe^{2+} contributing to the magnetism. An example of this antiferromagnetic contribution in similar complexes can be found in [32, 33]. In those works the authors modeled such magnetic response using the isotropic spin-spin interaction by means of the Heisemberg-Dirac-Van Vleck Hamiltonian H = -$2J_1(S_1 \cdot S_2 + S_1 \cdot S_3)$-$2J_2(S_2 \cdot S_3)$, where $S_1 = S_2 = S_3 = 5/2$ [32, 33]. In our particular case, we must also consider a certain amount of a paramagnetic HS Fe^{2+} impurity (8%), to reproduce the experimental data. The best fit has been obtained with the following parameters: J_1 = -55 cm^{-1}, g = 2.00, and J_2 = -36 cm^{-1}. Red curve in Fig 5.13 which fits with the parameters found in other $Fe^{3+}O$ trimers [33]. No satisfactory fitting has been obtained with $J_1 = J_2$. This could be due to small differences on the geometry of the six $[Fe^{2+}$(bppCOOH)-(bppCOO)$]^+$ units attached to the central $[Fe_3^{3+}(\mu_3$-O)-$(OH_2)_3]^{7+}$ trimer. The same behavior has been observed for similar complexes [32]. A small zero-field-splitting contribution with D = 3 cm^{-1} from the 8% HS Fe^{+2} impurity has been included [19].

Finally, the divergence from the fitting values obtained at temperatures above 200 K could be attributed to partial SCO of the six $[Fe^{+2}$(bppCOOH)(bppCOO)$]^+$ units, in agreement with the Raman results. The difference between the theoretical (μ_MT) curve corresponding to the $[Fe_3^{3+}(\mu_3$-O)-$(OH_2)_3]^{7+}$ trimer and the experimental one is more marked above 300 K. This may be explained as a gradual SCO transition occurring in the 300-400 K temperature range. From the differences observed we can estimate a HS fraction of $\sim$ 20% at 300 K, which increases to $\sim$ 60% at 400 K. By comparison we can conclude that $T_{1/2}$ value of (2) is close to that of (1) (380 K) [19]. At the temperature at which the X-ray measurement has been performed (250 K), this fraction falls down to $\sim$ 7%, and that explains why the HS state is not detected through this technique. Mössbauer spectra would be required for an accurate estimation of the HS and LS fractions of this system. Unfortunately, the small amount of sample available prevents the use of this technique. In this situation, compound (2) results on bench sample for demonstration of the Raman spectroscopy capabilities, demonstrating successful application on reduced volumes of the sample, just a single microcrystal is required [1]. Because of the low amount of sample available, as far as we can see, Raman measurements would be the only way to offer additional information about the oxidation and spin states of iron in (2).

For this purpose, the Raman set up of Fig. 2.2 has been modified to allow the sample temperature control. Variable-temperature Raman spectra of (1) are shown in Figs. 5.14 and 5.15 corresponding to different ranges of the spectra. The spectra have been acquired at 647.1 nm excitation wavelength (from an Ar-Kr ion laser) employing an excitation power of about 7.5 mW.

As Fe is coordinated to the ligand through N atoms we expect to observe the Fe-N vibrations that can be found at 150-600 cm^{-1} region [15]. in parallel, at 1000-1800 cm^{-1} we can observe the M-L vibrations. First, we focus in the Fe-N region because the straightforward relation of this modes with the Fe^{2+} modes. Eventually, we may find relevant information in the M-L modes as described below.

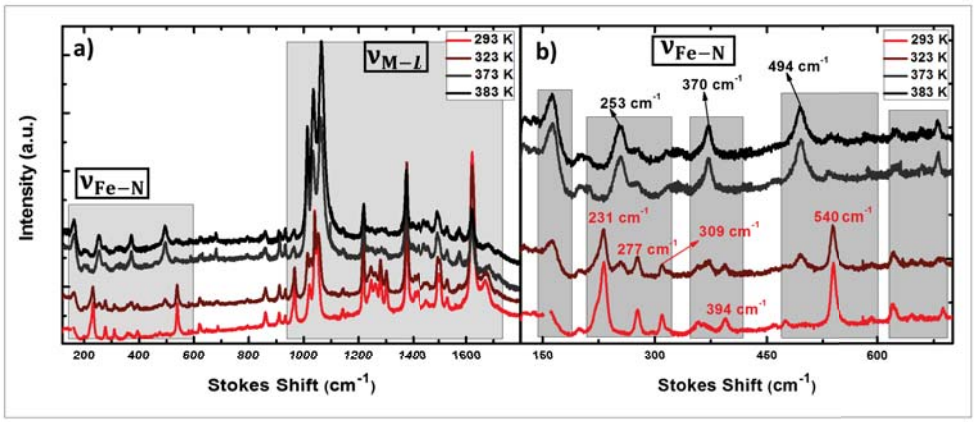

Figure 5.14: Raman spectra of a single crystal of (1) at different temperatures. It can be seen two shaded zones to Fe-N vibrations and M-L vibrations.

Significant changes occur in the Fe-N modes of (1) spectra. The peaks at 231, 277, 309, 394 and 540 cm^{-1}, clearly observed at room temperature, are not present above 380 K. At these temperatures, different peaks appear at 253, 370 and 494 cm^{-1}. These changes could be associated to the Fe-N vibration modes in agreement with calculations and experimental spectra in $[Fe(Phen)_2(NCS)_2]$ (Phen =phenantroline) [35]. A clear signature of the LS→HS transition is the absence of the 231 cm^{-1} peak (observed at room temperature) in favor of the 253 cm^{-1} one (at 383 K) [1]. In a similar way, the peaks at 277, 309, 394 and 540 cm^{-1} disappear with the onset of 370 and 494 cm^{-1}. All this changes, and therefore the spin transition, are correlated with variations in the M-L region where we observe peaks appearing and disappearing and in the range 1000-1300 cm^{-1}. It agrees with the observed SCO transition of Fe^{2+} in compound (1) [19]. In the case of the compound (2) we cannot resolve the Fe-N modes due to the high signal-to-noise ratio. Fortunately, we can trust on those intense peaks at the M-L. To do so, in Fig. 5.15 we compare the temperature evolution of both compounds. As afore mentioned, the compound (1) is at low spin at 293 K and sweeps to high spin at 383 K, see Fig. 5.15 a). The swept can be monitored through the peaks 966, 1245, 1263, 1280 and 1303 cm^{-1} (at room temperature) that disappears at 383 K (HS). Simultaneously, the peaks at 1020, 1040 and 1064 cm^{-1} peaks are shifted, and

their intensity ratios are considerably altered above 380 K. In the HS configuration, a new peak at 1012 cm^{-1} is observed together with two very intense peaks at 1034 and 1064 cm^{-1}. This last one is the most intense in this range. The changes in the intensity of the peaks at 1040 cm^{-1} (LS) and 1012 cm^{-1} (HS) are in agreement with that observed for an Fe^{2+} complex of a 1-bpp derivative. These peaks are assigned to a pyridine ring-breathing mode whose motion is coupled strongly to the Fe-N stretching [36]. The spectrum measured at 363 K after heating to 390 K recovers the peaks observed before heating, confirming the reversibility of the SCO process (Fig. 5.14). This suggests that, these spectra are close to the LS (293 K) and HS spectra (above 380 K), in good agreement with the metal-bond distances and magnetic properties of [19].

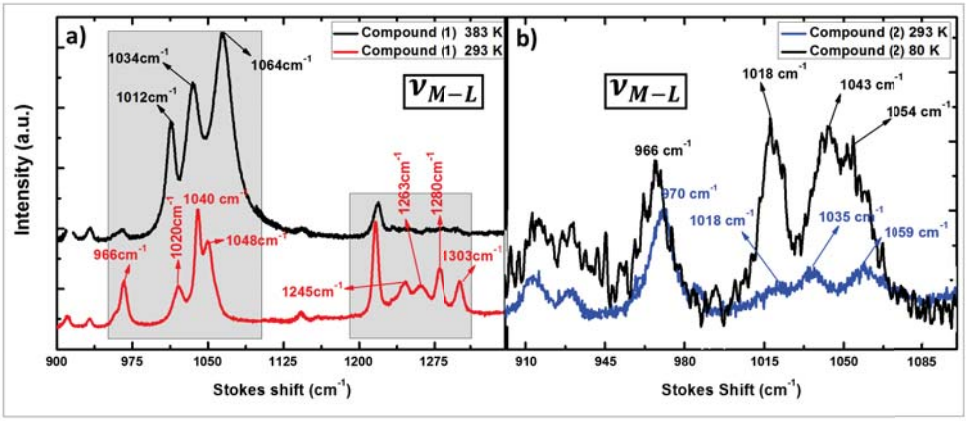

Figure 5.15: Raman spectra of single crystals of (1) and (2) at different temperatures (RT is 293 K).

Fig. 5.15 b) the spectra are acquired at room (293 K) and low temperature (80 K) to compare with the corresponding magnetic measurements. At room temperature we can distinguish some peak related with the Fe^{2+} in the LS configuration. We reduce the temperature in order to obtain more clear spectra (see, blue line in Fig. 5.15 b)). Here, we can distinguish peaks at 1018, 1043, and 1054 cm^{-1}. The coincidence with the LS of Fe^{2+} is pretty clear. It is also worth to mention the high contribution of the 966 mode at cm^{-1}. This mode associated to M-L vibration also disappears in compound (1) in the LS and disappears during the sweep to HS configuration. Then, it makes sense to associate it to the presence of Fe^{2+}. The positions of the other peaks are similar to those of (1) at 300 K. We may also point the presence of a very weak peak at 1018 cm^{-1}. The higher relative intensities of this peaks with respect to its neighbors located at 1043 and 1054 cm^{-1} could indicate a small fraction of HS Fe^{2+} at room temperature. Moreover, the intensity ratio between these peaks shows a certain

dependence with temperature. However, we cannot not confirm this hypothesis in the current state of our research. Still, this fraction would be too low to be detected by the X-ray measurements performed at 250 K.

5.4 Conclusions

In this chapter we have used Raman spectroscopy to illustrate the SCO. We have worked in two different kind of samples, in both cases, we may want to characterize using the less amount of material the best. In the first part, molecular SCO nanoparticles have been measured demonstrating that the thermal hysteresis χT vs T curve) can be monitored by consecutive acquisition of Raman spectra as the temperature is increased. The experiments are simultaneously carried out in two similar NP systems: $[Fe(Htrz)_2(trz)](ClO_4)$ and $[Fe(Htrz)_2(NH_2trz)]_2(BF_4)$. In both cases, Raman spectra have shown a clear signature of the LS→HS transition, in agreement with previous magnetic measurements. This consists of the vanishing of the Fe-N stretching mode. This vibrational mode is really active in the LS state resulting on a narrow peak around 250 cm^{-1} in most triazole based compounds, as extensively reported in literature.
In the second part we have characterized micro-crystals formed by coordination of complexes. The synthesis of the micro-crystals is based on the substitution of the 1-bpp ligand with a carboxylate group in the bppCOOH ligand for the preparation of polynuclear complexes based on the $[Fe^{2+}bpp)_2]^{2+}$. One of the products is the nonanuclear cluster, compound (2). Comparison of Raman spectroscopy of (2) confirmed the presence of Fe^{2+}. It is worth to mention that (2) represents the first SCO compound in which the bppCOOH ligand is coordinated to a magnetic ion to give rise to polynuclear species. The synthesis and crystallization of those macromolecular complexes would result of great interest given the multifunctional capabilities of the resulting materials. However, the low yield expected in the procedures might be a constraint for conventional structural characterization techniques. In this chapter we have demonstrated the potential of Raman measurements to complete characterization of macromolecular compounds. As a clear advantage, minor material quantities are required.

Bibliography

[1] Gütlich, P. and Goodwin, H.A. *Spin Crossover-An overall Perspective.* Topics in current chemistry Springer, Verlag, Berlin-Heidelberg-New York, 233-235, (2004). See for general reviews.

[2] Giménez-Marqués, M. *Stimuli-responsive magnetic coordination polimers: from crystals to nanoparticles.* Tesis Universidad de Valencia, (2013).

[3] König, E. and kremer, S. *Exact spin-pairing energies at the crossovers in octahedral d^4, d^5, d^6, and d^7 transition metal complexes*, Theor. Chim. Acta 23:12, (1971).

[4] Kahn, O. and Martínez, C.J. *Spin-Transition Polymers: From Molecular Materials Toward Memory Devices.* Science, 279, 5347, 44-48, (1988).

[5] *www.chem.libretexts.org/Core/InorganicChemistry/CrystalFieldTheory/Introductionto*

[6] Shriver, D. F., Atkins, P. W. and Langford, C.H. *Inorganic chemistry.* Oxford University Press: Oxford, (1999).

[7] Kröber, J., Audière, J.P., Claude, R., Codjovi, E., Kahn, O., Hasnoot,J.G., Grolière,F., Jay,C., Bousseksou,A., Linarés,J., Varret,F. and Gonthier-Vassal, A. *Spin Transitions and Thermal Hysteresis in the Molecular-Based Materials $[Fe(Htrz)_2(trz)](BF_4)$ and $[Fe(Htrz)_3](BF_4)2{\cdot}H_2O$ (Htrz = 1,2,4-4H-triazole; trz = 1,2,4-triazolato).* Chem.Mat., 6(8), 1404-1412, (1994).

[8] Hasnoot, J.G., Vos, G., and Groeneveld, W.L. *1,2,4-Triazole Complexes, III: Complexes of Transition Metal(II) Nitrates and Fluoroborates.* Z. Naturforsch, 32b, 1421, (1977).

[9] Urakawa, A., Beek, W. V., Monrabal-Capilla, M., Galán-Mascarós, J. R., Palin, L. and Milanesio, M. J. *Combined, Modulation Enhanced X-ray Powder Diffraction and Raman Spectroscopic Study of Structural Transitions in the Spin Crossover Material $[Fe(Htrz)_2(trz)](BF_4)$.* J. Phys. Chem. C., 115(4), 1323-1329, (2011).

[10] Grosjean, A., Daro, N., Kauffmann, B., Kaiba, A., Mondieig, D., Pechev, S., Lebraud, E., Létard, J.F. and Guionneau, P. *The 1-D polymeric structure of the $[Fe(NH_2trz)_3](NO_3)_2{\cdot}nH_2O$ (with n = 2) spin*

crossover compound proven by single crystal investigations. Chem. Commun., 47, 12382, (2011).

[11] Coronado, E., Galán-Mascarós, J. R., Monrabal-Capilla, M., García-Martínez, J., Pardo-Ibáñez, P. *Bistable Spin-Crossover Nanoparticles Showing Magnetic Thermal Hysteresis near Room Temperature.* Adv. Mater., 19, 1359, (2007).

[12] Kahn, O. and Martinez, C.J. *Spin-Transition Polymers: From Molecular Materials Toward Memory Devices.* Science, 279, 5347, 44-48, (1988).

[13] Galán-Mascarós, J. R., Coronado, E., Forment-Aliaga, A., Monrabal-Capilla, M., Pinilla-Cienfuegos, E. and Ceolin, M. *Tuning Size and Thermal Hysteresis in Bistable Spin Crossover Nanoparticles.* Inorg. Chem., 49(12), 5706-5714, (2010).

[14] Krober, J., Codjovi, E., Kahn, O., Groliere, F. and Jay, C. *A spin transition system with a thermal hysteresis at room temperature.*J. Am. Chem. Soc., 115(21), 9810-9811, (1993).

[15] (a) Takemoto, J.H., Hutchinson, B. *Effect of magnetic crossover on the low-frequency IR spectrum of [Fe(1,10-phenanthroline)$_2$(NCS)$_2$].* Inor. Nucl. Chem. Lett. 8(9), 769-772, (1972); (b) *Low-frequency infrared spectra of complexes which exhibit magnetic crossover. I. Iron(II) complexes of 1,10-phenanthroline and 2,2'-bipyridine.* Inorg. Chem. 12(3), 705-708, (1973); (c) Takemoto, J.H., Streusand, B., Hutchinson, B., *Far-infrared spectra of some Fe(1,10-phenanthroline)$_2X_2$ complexes.*Spectrochim. Acta A 30(3), 827-834,(1974).

[16] Moussa, N., Ostrovskii,D., Martínez-García, V., Molná, G., Tanaka, K., Gaspar, A.B., Real,J.A.and Bousseksou, A. *Bidirectional photo-switching of the spin state of iron(II) ions in a triazol based spin crossover complex within the thermal hysteresis loop.* Chemical Physics Letters, 477, 156-159, (2009).

[17] Smit, E., Manoun, B. and de Waal, D. *Low-wavenumber Raman spectra of the spin-transition complexes [Fe(NH$_2$ trz)$_3$](ClO$_4$)$_2$ and [Fe(Htrz)$_3$](ClO$_4$)$_2$.* J. Raman Spectrosc. 32 (5), 339-344, (2001).

[18] Smit, E., de Waal, D. and Heyns, A.M*Spin-transition complexes [Fe(Htrz)$_3$](ClO$_4$)$_2$ and [Fe(NH$_2$trz)$_3$](ClO$_4$)$_2$. FT-IR spectra of a low pressure and a low temperature phase transition.* Materials Research Bulletin 35, 1697-1707, (2000).

[19] Abhervé, A., Clemente-León, M., Coronado, E., Gómez-García, C.J. and López-Jordà, M. *A spin-crossover complex based on a 2,6-bis(pyrazol-1-yl)pyridine(1-bpp) ligand functionalized with a carboxylate group.* Dalton Transactions, 43,9406,(2014).

[20] Halcrow, M.A.*The synthesis and coordination chemistry of 2,6-bis(pyrazolyl)pyrimidines and related ligands-Versatile terpyridine analogues*, Coordination Chemistry Review, 249, 2880, (2005).

[21] Rajadurai, C.,Fuhr, O.,Kruk, R.,Ghafari, M.,Hahn, H. and Ruben, M.*Above room temperature spin transition in a metallo-supramolecular coordination oligomer/polymer* Chemical Communication, 2636, (2007).

[22] Tovee, C.,Kilner, C.A.,Barrett, S.A.,Thomas, J.A., and Halcrow, M.A.*A Back-to-Back Ligand with Dipyrazolylpyridine and Dipicolylamine Metal-binding Domains.* European Journal of Inorganic Chemystry, 2010, 1007, (2010).

[23] González-Prieto, R.,Fleury, B.,Scharamm, F.,Zoppellaro, G., Chandrasekar, R., Fuhr, O.,Zlebedkin, S., Kappes, M. and Ruben, M.*Tunning the spin-transition properties of pyrene-decorated 2,6-bispyrazolylpyridine based Fe(II) complexes.* Dalton transactions, 40, 7564, (2011).

[24] Halcrow, M.A.*Recent advances in the synthesis and applications of 2,6-bispyrazolylpyridine derivatives and their complexes.* New Journal of Chemistry, 38, 1868, (2014).

[25] Kershaw Cook,L.J.,Shepherd, H.J.,Comyn, T.P.,Baldé, C., Céspedes, O., Catanet, G. and Halcrow, M.A.*Decoupled Spin Crossover and Structural Phase Transition in a Molecular Iron(II) Complex.* Chemical European Journal, 21, 4805, (2015).

[26] Kershaw Cook,L.J.,Kulmaczewski, R.,Mohammed, R.,Dudley, S., Barett, S.A., Little, M.A., Deeth, R.J. and Halcrow, M.A.*A unified Treatment of the Relationship Between Ligand Substituents and Spin State in a Family of Iron(II) Complexes.* Angewandte Chemical International Edition, 55, 4327, (2016).

[27] Decurtins, S.,Gütlich, P.,Köhler, C.P.,Spiering, H. and Hauser, A.*A Light-induced excited spin state trapping in a transition-metal complex: The hexa-1-1propiyltetrazole-iron(II) tetrafluoroborate spin-crossover system.* Chemical Physical letters, 105, 1, (1984).

[28] Buchen, T.,Gütlich, P.,Sugiyarto, K.H. and Goodwin, H.A. *High-Spin→Low-Spin Relaxation in $[Fe(bpp)_2](CF_3SO_3)_2H_2O$ after LIESST and Thermal Spin-State Trapping. Dynamics of Phase Transition.*, Chemical European Journal, 2, 1134, (1996).

[29] Abhervé, A., Recio-Carretero, M.J., López-Jordà, M., Clemente-Juan, J.M., Canet-Ferrer, J., Cantarero, A., Clemente-León, M. and Coronado, E. *Nonanuclear Spin-Crossover Complex Containing Iron(II) and Iron(III) Based on a 2,6-Bis(pyrazol-1-*

yl)pyridine Ligand Functionalied with a Carboxylate Group. Inorg. Chem., 55 (18), pp 9361-9367, (2016).

[30] Ogrin, D. and Barron, A.R. *Synthesis and Structure of [$Fe_3O(O_2CCH_2OMe)_6(H_2O)_3$][$FeCl_4$].* J. Chem. Crystallogr., 39, 68, (2009).

[31] Liu, W., Thorp, H.H.*Bond valence sum analysis of metal-ligand bond lengths in metalloenzymes and model complexes. Refined distances and other enzymes.* Inorganic Chemistry, 32, 4102, (1993).

[32] Raptopulou, C.P, Tangoulis, V., Phycharis, V.*Synthesis and structural characterization of (NH_4)-[$Fe_3(\mu_3$-$OH)(H_2L)_3(HL)_3$] H_3L=Orotic Acid Present Two Novel Metal-Binding Modes of the Orotate Ligand: The Case of a Spin-Frustrated System.* Inorganic Chemistry, 39, 4452, (2000).

[33] Boudalis, A.K., Sanakis, Y., Dahan, F., Hendrich, M. and Tuchagues, J.P. *An Octanuclear Complex Containing the Fe_3^{7+} Metal Core: Structural Magnetic, Mösbauer and Electron Paramagnetic Resonance Studies.* Inorganic Chemistry, 45, 443, (2006).

[34] Craig, G.A., Sánchez-Costa, J., Roubeau, O., Teat, S.J.,Shepherd, H.J.,Lopes, M., Molnar, G., Bousseksou, A. and Aromí, G. *High-temperature photo-induced switching and pressure-induced transition in a cooperative molecular spin-crossover material.* Dalton Transactions, 43, 729, (2014).

[35] Bousseksou, A., McGarvey, J.J., Varret, F., Real, J.A., Tuchagues, J.P. and Boillote, M.L. *Raman spectroscopy of the high- and low-spin states of the spin crossover complex Fe($phen_2$($NCS)_2$: an initial approach to estimation of vibrational contributions to the associated entropy change.* Chemical Physics Letters, 318, 4-5, 409-416, (2000).

[36] Cavallini, M., Bergenti, L., Milita, S., Kengne, J.C.,Gentili, D.,Ruani, G., Salitros, I., Meded, V. and Ruben, M. *Thin Deposits and Patterning of Room-Temperature-Switchable One-Dimensional Spin-Crossover Compounds.* Langmuir, 27, 4076,(2011).

Chapter 6

Surface-Enhanced Raman Scattering in III-V nanowires functionalized by gold nanoparticles

6.1 Introduction

The study of the interaction between electromagnetic field and free electrons in a metal is known as "Plasmonics". In order to have collective oscillations, free electrons in the metal can be excited by the electric component of light. When such oscillations are restricted to a metal-dielectric interface and light interacts with particles that are much smaller than its wavelength, a local charge oscillation around the particle is produced, which is known as localized surface plasmon resonance (LSPR) [1].

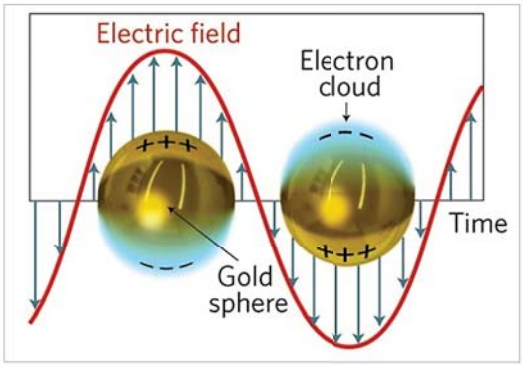

Figure 6.1: Collective oscillation of electrons with the incident electromagnetic field in a gold nanoparticle (LSPR). Figure extracted from [2].

Despite the wide range of existing plasmonic materials, the noble metals gold and silver are the most often utilized. Even if the preparation of monodispersed Au spherical nanoparticles is well known since the mid 20th century [3], the progress achieved during the last decade in the synthesis of AuNPs with anisotropic morphologies is huge [4, 5]. Due to their structural, optical and catalytic properties, anisotropic AuNPs are of special interest because of the high electric field enhancements that they present at sharp edges and tips, making them highly attractive

as plasmonic enhancers for surface enhanced Raman scattering [4]. This means that they are very interesting for several applications because of their plasmon tunability into the near infrared (NIR) region and the multiple hot-spots generated at their branches [6]. The intense local electric field enhances not only the scattering of molecules nearby the surface [7], but also their photoluminescence properties [8]. In this context, this Chapter is focused on the use of gold nanorods, nanotriangles and nanostars as SERS nanoparticles for studying III-V nanowires.

6.1.1 The Electromagnetic Mechanism of Surface-Enhanced Raman Scattering

Collective oscillation of conduction electrons, resulting from the interaction with electromagnetic radiation, are responsible for the optical properties of small metal NPs. Due to the presence of free conduction electrons, these properties can be observed in Au, Ag, and Cu, mainly. A dipole is formed in the nanoparticle, induced by the electric field of the incoming radiation. A unique resonance wavelength results as a restoring force in the nanoparticle, trying to compensate the dipole. The oscillation wavelength depends on a number of factors, such as particle size and shape, as well as the nature of the surrounding medium, as the most importants [9].

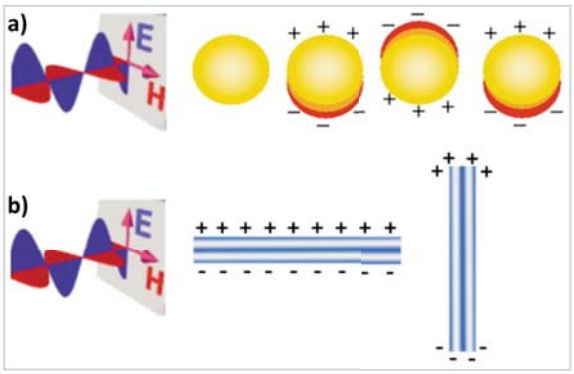

Figure 6.2: a) Schematic drawing of the interaction of an electromagnetic radiation with a metal nanosphere. A dipole is induced, which oscillates with the electric field of the incoming light. b) Transverse and longitudinal oscillation of electrons in a metal nanorod. Figure extracted from [10].

The resonance wavelength for nonspherical particles such as rods, depends on the orientation of the electric field, in which two oscillations, transverse and longitudinal, are possible (Fig. 6.2 b)). In addition, when nanoparticles are close enough, neighboring interactions between particles arise, so that the models for isolated particles do not hold. As an example to understand SPR and SERS we use a small gold nanosphere with molecules adsorbed on the surface [11, 12]. If the radius of a metallic sphere, a is much smaller than the wavelength of the incident light

($a/\lambda < 0.1$), the response of the sphere to the external field can be simplified as an induced dipole p

$$p = \varepsilon_0 \varepsilon_m g_0 E_0 \tag{6.1}$$

where ε_0 is the vacuum permittivity, ε_m is the dielectric constant of the surrounding medium, E_0 is the incident electric field in frequency ω_0 and g_0 can be expressed as

$$g_0 = \frac{\varepsilon(\omega_0) - \varepsilon_m}{\varepsilon(\omega_0) + 2\varepsilon_m} \tag{6.2}$$

The electric field strength inside E_{in} and outside E_{out} of the Au nanosphere are

$$E_{in} = \frac{3\varepsilon_m}{\varepsilon\omega_0 + 2\varepsilon_m} E_0 \tag{6.3}$$

$$E_{out} = E_0 \frac{3\hat{n}(\hat{n} \cdot p) - p}{4\pi\varepsilon_0 \varepsilon_m r^3} \tag{6.4}$$

As we can see, g_0, E_{in} and E_{out} can reach their maxima as long as the denominator term $\varepsilon(\omega_0) + 2\varepsilon_m$ gets close to 0,

$$Re[\varepsilon] + 2\varepsilon_m \to 0 \qquad \text{and} \qquad Im[\varepsilon] \to 0 \tag{6.5}$$

In this way, the real part of dielectric function of the metal, $Re[\varepsilon]$, should be negative and close to $-2\varepsilon_m$, whereas the imaginary part, $Im[\varepsilon]$, should be positive but very small. Fortunately, free-electron metals, such as Ag, Au and Cu, fulfil these conditions well in the visible regime, whereas transition metals do not [13]. At resonant conditions, the conduction band electrons can be coherently excited and collectively oscillating around the background ion cores in the presence of interfacial metal-dielectric nanostructured boundaries. This collective electron motion can be quantized as surface plasmon [14,15]. Also at resonant conditions, the molecules are directly adsorbed on, or get very close to, the nanostructured surfaces, which will be polarized by the enhanced local optical field, and create an induced dipole oscillating in the Raman-shifted frequency ω_R ($\omega_R = \omega_0 - \omega_k$, where ω_k is the vibrational frequency of the k^{th} normal mode), which will further polarize the Au NPs. Au NPs will finally re-irradiate into far field (at frequency ω_R) where the detector is located. According to the optical reciprocal theorem, the re-irradiation process will win the second enhancement at the Raman-shifted frequency. Therefore, the total enhancement in the small particle approximation is $\sim 4 \mid g_0 \mid^2 \mid g \mid^2$ [16].

$$G = G(\omega_0)G'(\omega_R) \approx \frac{\mid E_{loc}(\omega_0) \mid^2}{\mid E_0(\omega_0) \mid^2} \frac{\mid E(\omega_R) \mid^2}{\mid E_0(\omega_R) \mid^2} \tag{6.6}$$

is the enhancement factor for SERS, where

$$g = \frac{\varepsilon(\omega_R) - \varepsilon_m}{\varepsilon(\omega_R) + 2\varepsilon_m} \quad . \tag{6.7}$$

Usually, for low-frequency vibrational normal modes of adsorbed molecules, $\omega_0 \sim \omega_R$, $g \sim g_0$, and the total enhancement factor (EF) can be further approximated to be $4 \mid g_0 \mid^4$. That is why G can be approximated as

$$G = G(\omega_0)G'(\omega_R) \approx \frac{\mid E_{loc}(\omega_0) \mid^4}{\mid E_0(\omega_0) \mid^4} \tag{6.8}$$

In summary, there are two steps of enhancement during the process of SERS. The first step is the enhancement of the incident local field because of the excitation of SPR. Here, the Au NP works as a receiving optical antenna to transform far field (in frequency ω_0) to near field. The second step is the enhancement of far field in certain range of solid angles. Here, the Au NP works as a transmitting optical antenna to transform near field in the Raman-shifted frequency ω_R to far field, and SERS enhancement is achieved when incoming and outgoing fields are in resonance with the LSPR of the NP [16]. Since molecular vibration frequencies ω_{vib} are small compared to the excitation frequency ω_0, the shift ($\omega_0 - \omega_{vib} = \omega_r \approx \omega_0$) of the outgoing field is also small and the enhancement factor (EF) can be approximated to the fourth power of the local EM field enhancement at NP surface [17]. SERS enhancement factors (EF) were calculated by means of the frequently used equation, [19]

$$EF = \frac{I_{SERS}}{N_{SERS}} \cdot \frac{I_{NRS}}{N_{NRS}} \tag{6.9}$$

where I_{SERS} and I_{NRS} are the SERS and normal Raman scattering intensities, respectively, and N_{SERS} and N_{NRS} are the number of molecules contributing to the scattering intensity. In the case of a NP dimer, owing to the strong coupling of two dipolar plasmons, the optical local field in the gap between two NPs will be extremely intense in contrast to single NP detection. Overall, SERS is the effect of plasmon-enhanced Raman scattering and any nanostructure possessing the features of exciting SPR in the visible and near-IR regimes can support SERS as well. Optimization of the key factors of SPR and Raman will help us to optimize the conditions of SERS. The most interesting aspects of metal nanoparticles are those for which their optical properties depend strongly on the particle size and shape.

6.2 Experimental section

We used three different types of gold nanoparticles in order to compare the enhancement for several III-V nanowires with the aim of studying the transversal phonon SO of several nitrides.

6.2.1 Synthesis of Nanoparticles

Seed-mediated growth methods developed for synthesizing large spherical and non spherical gold nanoparticles (AuNPs) [18], allows controlling the nucleation and grown processes, thereby obtaining improved monodispersity. This method comprises two steps:

- synthesis of the small spherical nanoparticles, called seeds,
- addition to a "growth solution" containing Au^{3+} ions, surfactants and a chemical reducing agent to induce anisotropic growth.

In this section gold NPs are obtained through seed-mediated growth by reduction with a solution containing a milder reducing agent (ascorbic acid, AA) of a strong reducing agent (sodium borhydride, BH_4). The metal salt is reduced to an intermediate state in order to catalyze the reduction only on the nanoparticle surface, avoiding the nucleation of new particles in the solution. With this method, size, shape and surface properties are controlled by the amount and nature of the reducing agent and the stabilizer, as well as by their ratio to the Au precursor.

Gold Nanorods (NRs)

Nanorods (NRs) and nanowires (NWs) are nanostructures with one dimension longer than the other two. The term nanorods is commonly referred to relatively short elongated particles (length over 100 nm), while nanowires are longer, not always perfectly straight, typically with aspect ratio (AR) above 10 and length up to 5 μm [17].

The synthesis of small metal NPs (seeds) is necessary so then they can be overgrown into larger particles with different shapes by reduction of a metal salt in the presence of a surfactant. Thus, nucleation and growth must be temporally separated, giving uniformity and precise control over particle size and aspect ratio.

LSPR wavelengths in NRs can be easily tuned, by varying the AR (Fig. 6.3). Typical UV-Vis spectra presents two plasmon bands, corresponding to transverse and longitudinal modes. The intensity of the transverse LSPR band is low and almost independent of the AR, the longitudinal LSPR is much more intense and strongly dependent on AR [20].

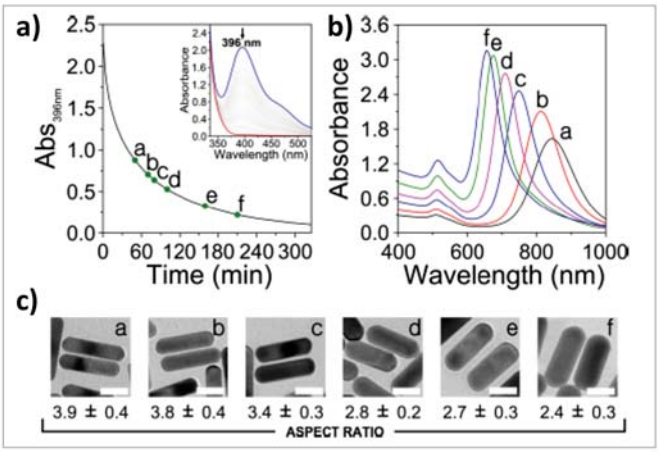

Figure 6.3: The of prereduction by 5-BrSA affects to the AR and the amount of reduced gold too. a) Kinetic study of the prereduction step (inset: full UV-vis spectra). b) UV-vis-NIR spectra of the various NR colloids obtained by changing the prereduction time. Abs_{369nm}: 0.88; 0.71; 0.64; 0.53; 0.33); 0.22 (UV-vis spectra were multiplied by the corresponding dilution factor). c) Representative TEM images of NRs obtained with different prereduction times (the labels correspond to those on the spectra in b). Scale bars: 20 nm. Figure extracted from [21].

According to Ligand Field Theory, the complexation strength of Au(III) with halide ions follows the series. I^{-}>Br^{-}>Cl− and with CTAB the chloride ligands in $[AuCl_4]^{-}$ are going to be replaced by bromide ions from the surfactant:

$$[AuCl_4]^{-} \rightleftharpoons [AuCl_3Br]^{-} \rightleftharpoons [AuCl_2Br_2]^{-} \rightleftharpoons [AuClBr_3]^{-} \rightleftharpoons [AuBr_4]^{-} \quad (6.10)$$

So the use of a weak reduction agent, Ascorbic Acid (AA) in this case, is one of the key points in the seeded growth method. This reductant is used in order to the gold reduction takes place only on existing nuclei solution which also acts as catalysts. Upon addition of AA to a growth solution containing a mixture of $HAuCl_4$ and CTAB, the reduction of Au(III) and to Au(I) takes place and the solution turns colorless which means that the ligand-to-metal charge transfer band disappears for a d^{10} metal center as Au(I).

$$Au^{3+}(precursor) + 2Au^{0} \rightleftharpoons 3Au^{+}(intermediate) \quad (6.11)$$

It is very important that the reducing agent cannot complete the reduction of Au(I) into Au(0), i.e. secondary nucleation during the growth step is prevented. In fact, the seeds act as catalyst for the final reduction step inducing the reduction of the Au(I) precursor on their surface only.
Another important issue about the reductant is the reduction-yield. In order to measure the reduction-yield in a more convenient way, it is useful to employ a simple spectroscopic analytical method based on the absorbance of light with a wavelength of 400 nm, which can be measured with a UV-vis spectrometer. It

is selected a wavelength where the main contribution to absorbance comes from absorption related to interband transitions in metallic gold which would be used to determine the amount of gold precursor being reduced. Liz-Marzán's group has found that a value of 1.2 for the absorbance at 400 nm corresponds to an Au(0) concentration of 0.5 mM. An absorbance at 400 nm below the expected value indicate that part of the gold precursor remained in solution as Au(I) which results in slow reshaping and spectral blueshift when nanorods are aged for long periods of time. A simple centrifugation step can be used to remove the excess of reagents and enhance the long term stability of gold nanorods (even for years).
The NRs are synthesized following the method of Scarabelli et al [21]. Starting with seeds synthesis 4.7 mL of CTAB 0.1 M is added to 25 μL 50 mM and low stirring during 5 min for complex formation. Then 300 μL of a freshly prepared $NaBH_4$ 10 mM solution are injected rapidly under vigorous stirring (>1400 rpm). After 10-20 s of vigorous stirring, the solution is left under mild stirring (400 rpm) before use until it turned light brown color).
The next step, pre-reduction, is calculated for final values of 50 mL. Adding 45 mg of 5-BrSA to 50 mL solution CTAB 0.05 M, once the Salicylic Acid is completely dissolved, 480 μL of $AgNO_3$ 10 mM solution are added under mild stirring. After 15 min 500 μL of $HAuCl_4$ 50 mM solution are added to the mixture under mild stirring. The pre-reduction of Au(III) to Au(I) by Salicylic Acid starts immediately after the addition. It is important to consider that this reduction is highly sensitive to temperature, so the solution must be at room temperature before adding the gold salts.
The Pre-reduction can be easily followed by UV-vis because the $[AuBr_4]^-$ complex is orange, with a maximum absorbance at 396 nm, whereas $[AuBr_2]^-$ is colorless, hence a reduction in absorbance at 396 nm means that more Au(III) precursor is being reduced to Au(I).
The final step is the growth is calculated for values of 50 mL too. The aspect ratio (AR) of the NRs can be controlled through pre-reduction time since the more Au(III) is reduced by 5-BrSA the lower final AR you are going to obtain. In Fig. 6.3 we observe that, as a reference, an absorbance of 396 nm between 0.8 and 0.85 will result in a longitudinal plasmon band centered around 800 nm (NR growth was monitored by UV-vis-NIR spectroscopy after reached the selected absorbance). Immediately after reached that value, the stirring speed is increased above 1000 rpm and 130 μL of AA 100 mM solution is added to the growth solution. In few seconds we observe that the mixture turns colorless and after stirring for 30 s, a volume of 80 μL of seed solution is added in order to start growth. After 30 s stirring the solution is detained and left undisturbed for 4 hours.

Gold Nanotriangles (NTs)

Nanoplates are nanomaterials in which one of the dimensions is much smaller than the other two. With triangular bases, NTs are very interesting nanoparticles because of their inherent sharp corners and edges, which can confine EM fields and therefore exhibit strong enhancements. High EM field enhancement at the tips corresponds to a dipolar plasmon mode, but at higher energies other modes present the highest enhancement at the edges and at the center of the NT [17]. NTs exhibit tunable plasmon resonances and can be selected by changing the AR (edge/thickness). In Fig. 6.4 a) it is observed that an increase in AR produces a red-shift in the dipolar LSPR. Additionally, NTs may present different degrees of truncation, depending on the selected synthetic method and preparation conditions. Truncation can also be used to tune the dipolar LSPR, leading to a blue-shift in the spectrum as the snip size of the missing corner is increased (Fig. 6.4 b) [17]).

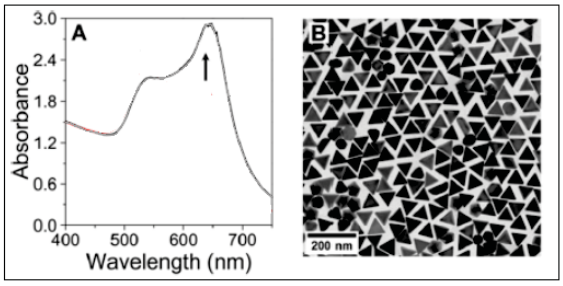

Figure 6.4: a) Synthesis of Au NTs. A) UV-vis spectra of NTs obtained with fast addition. Notice the different intensity ratio between the byproduct band (isotropic nanoparticles, maximum around 520-530 nm) and the band corresponding to the NTs (around 650 nm). B) TEM images of Au NTs prepared with fast addition. Figure extracted from [24].

It seems that wavy edges generated an additional enhancement with respect to straight ones, which is probably due to LSPR band broadening, thus a better match is obtained between incident laser and LSPR. The selection of NPs with LSPRs that match the excitation laser is therefore critical [17].
AuNTs are noticeable for their optical and plasmonic properties with LSPR values from 630 to 740 nm. However, the quality of AuNTs available is far from that can be found for AuNRs [23].
Gold nanotriangles (AuNTs) used in this experiment were synthesized by the group of Liz Marzán to absorbe in 647 nm range [24]. The synthesis of AuNTs is based on the seed-mediated growth originally proposed by Mirkin and co-workers [25]. The initial Au Seed@CTAC are prepared by the standard CTAC/$NaBH_4$

procedure, adding 25 μL of a 0.05 M $HAuCl_4$ solution to 4.7 mL of 0.1 M CTAC solution, 300 μL of a freshly prepared 0.01 M $NaBH_4$ solution is then injected under vigorous stirring. Excess borohydride is consumed by keeping the seed solution for 2 h at room temperature prior to use.
In a typical synthesis of 40 mL of a Au NT solution the following two growth solutions are prepared: (1) 1.6 mL of a 0.1 M CTAC solution is added to 8 mL of Milli-Q water, followed by 40 μL of 0.05 M $HAuCl_4$ solution and 15 μL of a 0.01 M NaI solution; (2) 500 μL of a 0.05 M $HAuCl_4$ solution is added to 40 mL of 0.05 M CTAC, followed by 300 μL of a 0.01 M NaI solution. The first solution is used to grow the CTAC capped seed into larger nanoparticles, while the second solution is used as the NT growth batch. Before proceeding, the initial seed@CTAC solution was diluted 10× in a 0.1 M CTAC solution. Subsequently, 40 and 400 μL of 0.1 M AA solution are added to solutions 1 and 2, respectively, and both solutions are manually stirred until the complete transparency of the solutions is achieved, indicating Au^{III} to Au^{I} reduction. Finally, 100 μL of diluted seed@CTAC solution is added to solution 1 (and manually stirred for 1 s), and immediately 3.2 mL of this solution is added to solution 2 (and manually stirred for a few seconds). The Au NT dispersion is left undisturbed at room temperature for at least 1 h.
Purification of the Au NTs is necessary. After spectroscopic characterization, the Au NT dispersion is purified by addition of a selected amount of 25 wt% CTAC solution. Flocculation of the Au NTs is completed overnight, the supernatant is then removed, and the precipitated particles are redispersed in 5 mL of 0.1 M CTAC solution. Typically the concentration in Au^0 of the purified sample is around 1.75 mM (estimated using the absorbance at 400 nm [21, 26]).

Gold Nanostars (NSs)

Gold nanostructures with star-like shapes are particularly exotic. Branched NPs - also called nanostars (NSs), nanoflowers or multipods - are NPs formed by a central body and several arms or tips protuding from it. These branches can be distributed symmetrically and NPs are referred to by the more general term nanostars if tips are randomly shaped and oriented. In some cases, the tips are not only irregular but can even be hyperbranched forming dendritic shapes and increasing the number of arms in non-radial directions [17]. The UV-Vis-NIR spectra of AuNSs typically feature a plasmon band in the 600-1200 nm region, corresponding to plasmon modes confined at the tips, as well as a smaller band/shoulder around 500-600 nm, related to a mode localized at the central body [17].
LSPR in AuNSs can be tuned through changes in the tips sharpness and/or AR.

Red-shifts are observed when the tip AR increases, similar to NRs [27].

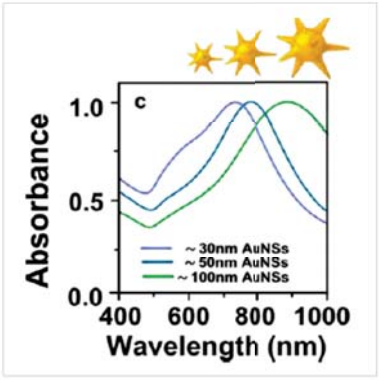

Figure 6.5: UV-vis-NIR spectra of AuNSs of different sizes. Figure extracted from [28].

In general, larger NSs show off an increased number and longer tips, which is correlated with an LSPR red-shift as the size increases. EELS mapping of AuNS together with BEM simulations revealed an extremely high EM field enhancement at the tips, corresponding to a low energy dipolar plasmon mode [27]. On the basis of single particle UV-Vis spectroscopy and FDTD calculations, Nordlander and co-workers [29] proposed that plasmon modes in NSs actually arise from hybridized modes from coupling between the tips and the central body (Fig. 6.6).

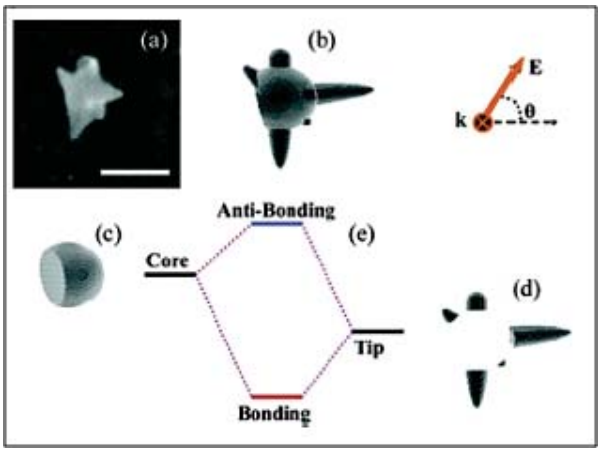

Figure 6.6: SEM image of a AuNS and the corresponding model (scale bar: 100 nm). Plasmon mode hybridization is sketched in the scheme and calculated EM field enhancements (FDTD), are shown as a function of polarization and wavelength of the excitation light. Figure extracted from [29].

Such a plasmon mode hybridization produces an antenna effect resulting in EM field enhancement of up to 4 times more than if only are produced by the tips.

The polydispersity in tip shape and orientation is traduced in broader plasmon bands from AuNSs, facilitating the use of Raman excitation lasers that do not match the absorbance maximun but still are on-resonance with a proportion of plasmon modes. In addition, due to the polydispersity in tip shape and orientation, plasmon bands from AuNS colloids are usually broader than those for NRs, thereby facilitating the use of Raman excitation lasers that do not precisely match the absorbance maximum, but are still on-resonance with a significant proportion of plasmon modes [17].
Branched nanoparticles display particularly high EFs at the resonance wavelength, even higher than those for rod or sphere dimers. One of first the methods developed for the synthesis of branched gold nanoparticles was inspired by the seeded-growth process described [30]. Different capping agents have been studied, including surfactants and polymers. The preferential adsorption of the capping molecules on certain crystalline facets of the metal seed surface has been suggested to trigger the anisotropic growth process, by modifying the growth rates along specific crystallographic directions. The influence of additives such as $AgNO_3$ has been also reported to affect the growth of AuNSs, so that a higher degree of control on the nanoparticle star-shape can be achieved by the addition of silver ions at different stages of the growth process [31]. The reducing agent also plays a significant role on the resulting shape of the nanoparticles. High yield production of monodisperse branched nanoparticles from 15 nm PVP-coated Au seeds was obtained when $HAuCl_4$ was reduced using N,N-dimethylformamide (DMF) in combination with poly(vinylpyrrolidone) (PVP) as stabilizer. The reduction kinetics of $AuCl_4^-$ on the Au seed surface can be controlled using the combined reducing ability of DMF and PVP, which also plays a role in the anisotropic growth. When intermediate concentrations of PVP were used, much more uniform nanoparticles were obtained compared to those nanoparticles obtained with a high concentration of PVP. Therefore, a rapid, kinetically controlled and preferential growth along various crystal faces that enables the formation of nanoparticles with stable star/flower-like shapes (Fig. 6.7) was proposed. This synthetic procedure also allows tuning both the size and the optical properties of the obtained nanostars. With decreasing $[HAuCl_4]/[Au_{seed}]$ ratio the obtained nanoparticles get smaller with shorter and lower number of spikes. The same method has also been employed to grow tips on other nanostructures such as AuNRs, as templates.
Gold seed nanoparticles were prepared by adding 12.5 ml of 1% citrate solution to 2.5 ml of boiling 50 mM $HAuCl_4$ solution under vigorous stirring. After 15 min boiling the solution was cooled down to room temperature and then stored at 4°C for long-term storage [27].
Gold PVP coated seeds are prepared by adding 0.122 g of PVP in 6 mL of water.

After 15 min sonicating 50 mL of citrate seeds are added and is stirred at room temperature during 24 h. After that it centrifuge during 90 min at 6000 rpm and redisperse in EtOH. In a typical synthesis, 54.6 μL of an aqueous solution of 50 mM $HAuCl_4$ is mixed with of 1.0 mL of 10 mM PVP (MW 10000) solution in 10 mL of DMF. After complete disappearance of the Au^{+3} 28.6 μL of the PVP coated seeds are added to the solution. In order to obtain middle size (mAuNS$\sim$ 50nm) of PVP-NSs, 500 μL are added to the solution with LSPR bands at 790 nm.
It must be cleaned at least five times to eliminate the excess of PVP for Raman measurements.

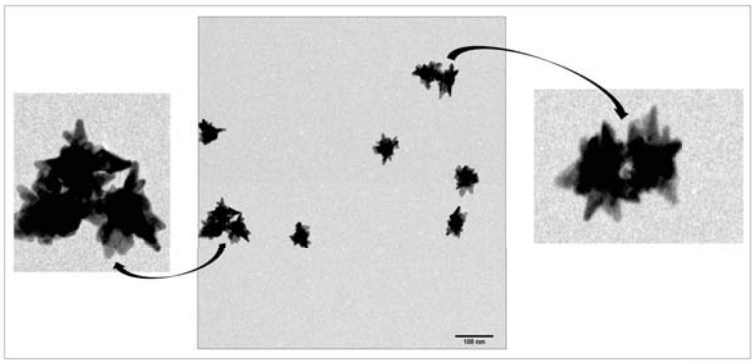

Figure 6.7: TEM image of surfactant PVP gold nanoparticles of $\approx$ 55 nm

6.3 Results and discussion

It is well-know that the enhancement factor (EF) in the surface enhannced Raman Scattering (SERS) is proportional to the fourth power of the electric field [17]. Experimentaly, this field enhancement can be estimated by means of the expresion to estimate the signal enhancement that might be expected from a given geometry [19], see eq. 6.9. Then, roughly speaking we can say that the figure of merit of the SERS signal is a question of field enhancement and number of molecules contribution to the enhancement. In order to calculate the enhancement factor it is necessary to normalize the number of nano-antennas but for simplicity we take the lower bound so the EF should be higher for single NPs.

6.3.1 Surface-Enhanced Raman Scattering in III-V semiconductors

In order to study the surface optical (SO) modes in III-V nanowires we use three different gold nanoparticles to enhance the Raman modes. The expected usual modes, for the studied semiconductors, are summed up in Table 6.1:

	E_{2L}	A_1(TO)	E_1(TO)	E_{2H}	A_1(LO)	E_1(LO)
GaN	144.0	531.8	558.8	567.6	734.0	741.0
InN	87	447	476	490.1	585.4	593
InP		302.1	302.4	306.4	341.9	not observed

Table 6.1: Raman phonon modes for GaN, InN and InP in (cm^{-1}). Data extracted from [36, 37].

The atomic amplitudes in SO phonons are confined to the near-surface region of the material and decay exponentially with distance. Depending on the penetration depths it can be distinguished macroscopic and microscopic SO phonon modes [32]. Macroscopic SO modes, are classified as optical (e.g. Fuchs-Kliewer [33]) and acoustic (e.g. Rayleigh) SO phonon frequencies.

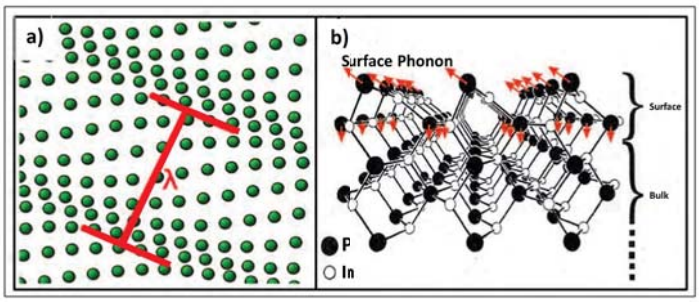

Figure 6.8: Schematic representation of: a) atomic motion in a phonon mode and b) SO phonon mode. The atomic displacement of SO phonons are confined to the top atomic layers Figure extracted from [32].

Acoustic SO modes in isotropic elastic media are propagated along the surface/interface and are displaced in the normal plane to the surface and the direction of propagation [34] and that is the reason to prefer lied down NWs. Contrary to an acoustic mode optical phonon is connected to a macroscopic electric field [33]. The frequency of an optical phonon can be determined and it is found to lie in between the frequency of the transverse optical (TO) and longitudinal optical (LO) bulk phonon. The representation of the atomic motion in a phonon mode has been illustrated in Fig. 6.8. Along this work we have shown that Raman spectroscopy is an essential tool to study vibrational modes of molecules and solids. Thanks to the weak interaction of photons with matter the penetration depth of photons is no less than approximately fifty atomic layers This is a huge advantage with respect to other the techniques, to study surface vibration modes. This is important since the vibrational frequencies of SO phonons are different from those of the bulk. Also, the energies of electronic states corresponding to the surface are different from bulk states and so the resonance condition of SO

phonons is different from that of bulk phonons.
The range of vibrational modes is extended at the nano-scale. There is a range of vibrational modes that we cannot find in bulk, that appear (or get larger importance) in nano-structures materials. For example, geometry and size-related phonons appearing in nano-structures solids such as nanowires and nanoparticles. This would be the case of SO and breathing modes arising from acoustic confinement. In case of nanowires, its cross-sectional shape make possible the SO phonon dispersion and it is usually observed that the TO and the LO modes have a position in energy close to the bulk. In case of variations, the size and the dimensionality of the structures decrease, the position can change appearing new Raman modes due to breakdown of translational symmetry in the finite size. On the other hand, the existence of boundary conditions at the nanoscale could generate electric and polarization forces and with an impact in the phonon dispersion. Several works have reported the presence SO modes in Raman spectra of semiconductor nanowires which have been assigned to SO phonons [32, 35]. Those phonons, when, generated at the interface between different materials, are propagated along the interface. This mode is activated by breakdown of the translational symmetry of the SO potential, which in the case of the nanowire can be due to the presence of roughness, saw tooth faceting on the nanowire sidewall or to a diameter oscillation along the nanowire length [35].

InN Nanowires with gold NTs

In order to study the surface optical phonon, InN nanowires are deposited over a glass substrate to suspend the NWs on top to allow the study of the surface optical phonon. This samples are characterized at 647 nm excitation wavelength. With that purpose, NTs has been provided by Leonardo Scarabelli and Dorleta Jiménez de Aberasturi from the Bionanoplasmonics Lab at CIC BiomaGUNE.

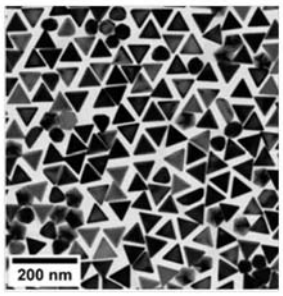

Figure 6.9: TEM image of NTs (≈ 70 nm). Figure extracted from [24].

According to literature (see table 6.1), we can expect the usual values to the transverse-optic (TO) phonon modes at 447 cm^{-1} for the A_1(TO) and 476 cm^{-1} for the E_1(TO), the peak at 490.1 cm^{-1} for the E_{2H} and the longitudinal optical (LO) phonon modes at 585.4 cm^{-1} for the A_1(LO) and 593 cm^{-1} for the E_1(LO). Two additional peaks at 528 and 560 cm^{-1} may be originated from surface disorder induced surface optical (SO) modes [32].

InN NW	Calculated SO modes	Experimental SO modes
A_1	528	526.1
E_1	560	558.1

Table 6.2: Optical SO phonon modes for InN NW in (cm^{-1}) [36]. Calculated and experimental values.

In Fig. 6.10 a), using NTs for enhancing the signal we found a broad band composed by an ensemble of phonon peaks of different nature. We have identified most of these peaks which are labelled at Fig. 6.10 b) [36]. Based on [32], the modes around 528-560 cm^{-1} have been assigned to SO modes with A_1 and E_1 characters, respectively. The spread in SO phonon essentially arises due to the wide range of diameter and dimension of the nanostructures. Together with this peaks we can identify E_1(TO), A_1(TO) transversal modes, A_1(LO) longitudinal mode and E_{2H} this peaks are in agreement with [36,37]. But we can also observed the SO phonon modes [32].

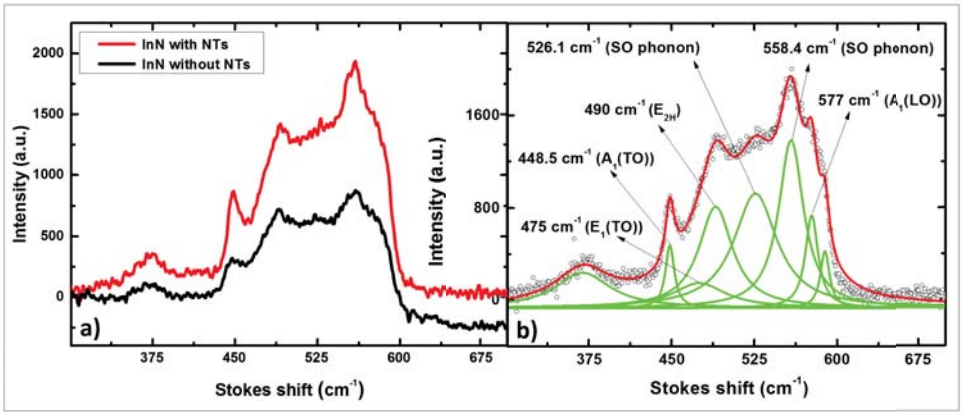

Figure 6.10: a) In black InN raman spectra without the NTsIn red SERS spectra with NTs. Raman spectra of InN with 647 nm excitation wavelength. b) Room-temperature Raman-scattering spectra of InN nanowires showing the experimentally observed data and the Lorentzian fit for the individual peaks. Room-temperature SERS spectra of InN nanowires (with NTs $\approx$ 55 nm) showing the experimentally observed data and the Lorentzian fit for the individual peaks. Full curve: total fitted spectrum, green curves: individual fitted peaks.

The advantage of NTs is that NWs are functionalized with them showing an

enhancement of 2.5 and they allow us to work with the 647 nm wavelength where the semiconductor NWs have the optimal absorbance. It is also remarkable that we observe both A_1 (TO) and (LO) mode when that usually we only see one of them because they only appear when are perpendicular to the direction of the measurement.

InP Nanowires with gold NSs

Gold NTs does not work with InP, so we decide to change NTs for NSs resulting a EF = 4. In this case, a glass substrate has been used to suspend InP nanowires in order to be decorated with gold NSs.

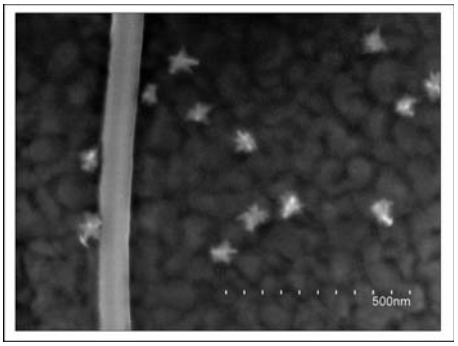

Figure 6.11: Gold NSs over InP nanowire.

The NSs has been prepared in collaboration with CICbiomaGUNE with an average size of $\approx$ 55 nm, exhibiting a maximum absorption around 760 nm and we use the 647 nm excitation wavelength In the case of the NSs we can slightly detune the excitation of the laser from the maximum and still obtain surface enhancement. This is because of , the polydispersity in tip shape and orientation which drive to an unhomogeneous broadening of the resonance [17]. The usual phonon modes for InP are shown in Table 6.3.

InP NW	Calculated modes	Experimental modes
A_1(TO)	305.3	302.1
E_1(TO)	306.3	302.4
E_{2h}	313.0	306.4
A_1(LO)	346.4	341.9
E_1(LO)	347.3	not observed

Table 6.3: Optical phonon modes for InP NW in (cm^{-1}) [37].

In this case we could not find calculated or measured SO for InP in the literature. So we focus on the characterization of the usual modes. As we have seen in NTs

case, it is remarkable that we can observe the A_1(TO) at 301.5 cm^{-1} and A_1(LO) at 341 cm^{-1} modes at the same time when usually we only observe one of them.

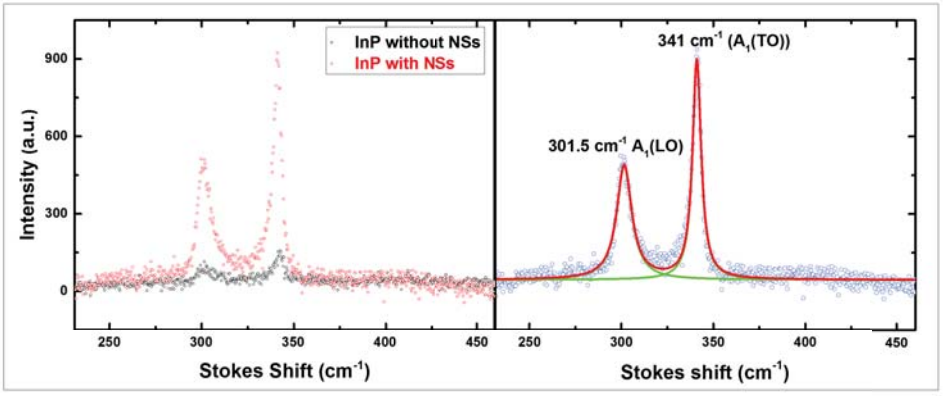

Figure 6.12: a) Raman spectra of InP with 647 nm excitation. b) SERS spectra of InP nanowires (with NSs ≈ 55 nm) showing the experimentally observed data and the Lorentzian fit for the individual peaks. Full curve: total fitted spectrum, green curves: individual fitted peaks.

After Raman characterization we have acquired a Raman mapping. The mapping has been also acquired exciting the sample at 632 nm wavelength. As a result we have resolved spatially the Raman signal around an area of 25×50 micron square. The image is composed by 2n×n pixels arising from the same amount of spectra. In any of this pixels we represent the intensity of the spectra at the band of 541 cm^{-1} coinciding with the mode A_1(TO).

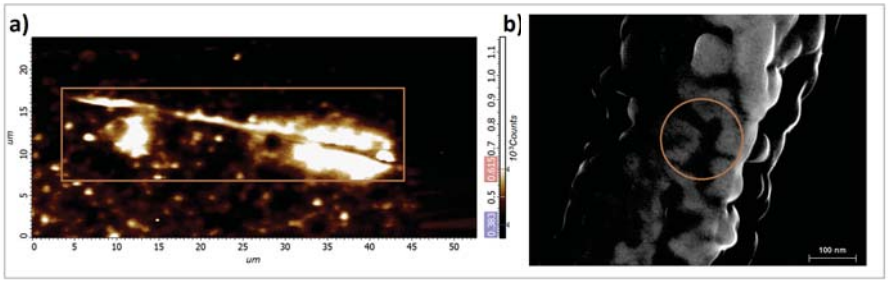

Figure 6.13: a) Raman mapping of a single InP nanowire measured. It can be observed the bright zone where the NSs are fixed to the NW. b) SEM image manipulated with DigitalMicrograph program to remark the zone of interaction among the NSs over the single NW.

In Fig. 6.13 a) we can see different contrast zones, mainly at the borders of the NWs where we use to found the larger amount of NSs and in Fig. 6.13 b) we observe the zone of interaction between the NSs where the enhancement is bigger.

GaN Nanowires with gold NRs

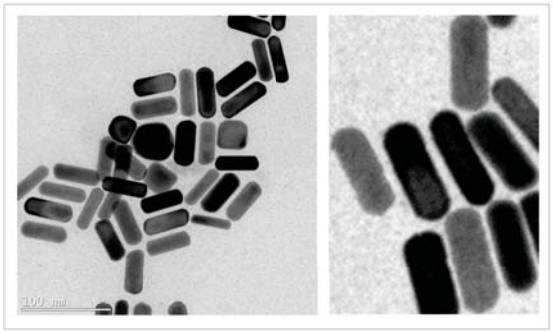

Figure 6.14: TEM images of NRs (≈ 55 nm).

GaN nanowires, grown epitaxially over Si substrates, are studied to show that any NP can be used to enhance the signal. The signal of these NWs is enhanced by means of gold NRs (≈ 55 nm) obtaining the SERS spectra with a EF ≈ 60. The NWs orientation is perpendicular to the Si substrate.

GaN NW	Calculated SO modes	Experimental SO modes
A_1	654	-
E_1	688	-

Table 6.4: Calculated and experimental SO phonon modes for GaN NW in (cm^{-1}) [32].

For SO phonon modes in GaN we can find calculated SO phonons, associated with $A_1(TO)$ at 533 cm^{-1}, $E_1(TO)$ at 560 cm^{-1}, E_{2H} at 567.6 cm^{-1} and reported peaks for SO phonon modes around 654 and 688 cm^{-1} [32].
We observe a clear enhancement difficult to quantify, due to the presence of the large peak of Si substrate, that we estimate around 60. Also, usual peaks (see table 6.1) are more defined and its relative intensity are bigger than without the NRs, but we do not observe SO phonons or (LO) modes with the (TO) modes as in the previous cases. We observe the transverse-optical modes $A_1(TO) = 532$ cm^{-1} and $E_1(TO) = 558.8$ cm^{-1} and the mode $E_{2H} = 567$ cm^{-1} and, as we can see in table 6.1, they are not shifted. Due to the different resonance wavelength depending on the orientation (more intense longitudinal LSPR band) of the electric field and the difficult to get the NRs fixed along its longitudinal oscillation, we have obtained enhancement but it is not possible to see any other peaks. We can think that, in this case, NRs are situated transversal to the NWs and that is the reason why we only observe (TO) modes. In the region where the SO phonon modes should

be (654 and 688 cm^{-1}), we can observe a very wide band but it is not possible to distinguish any peak. The problem of getting NRs aligned to the NWs make this NPs not suitable to make measurements in lied down NWs but the enhancement is bigger than in the other cases.

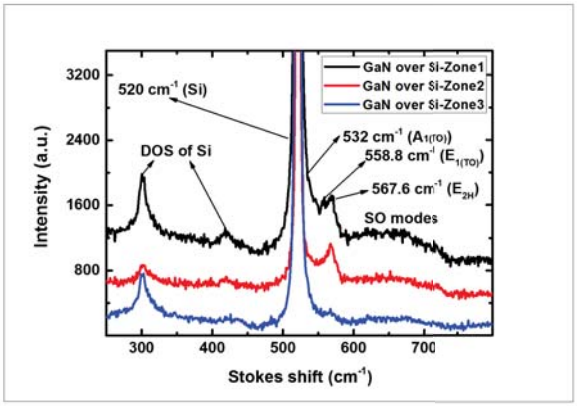

Figure 6.15: SERS in GaN nanowires with NRs (≈ 55nm). Raman spectra of GaN with 785 nm excitation.

6.4 Conclusions

In this chapter gold NP of different sizes and shapes were used to enhance the signal of semiconductor nanowires. Even when we are still working on the optimization of this kind of experiments, we have found in this approach a good option to study SO phonons in isolated NW.
The use of NP for the characterization of NWs is not just a question of surface enhancement. The most remarkable result is that, with NTs and NSs, we have obtain the (TO) and (LO) modes at the same time. which could not be found together in usual conditions.
Definitely gold NSs, with EF around 4, seems to be the candidate for characterization of NWs. In addition, NSs allow to use different excitation wavelengths without varying the size NPs. This result quite convenient in the characterization of III-V semiconductors which Raman signal is in addition favored using excitation wavelengths under 650 nm. So even when larger NSs absorbs between 800-900 nm it is advisable to use larger NSs to take advantage of the bigger EM field enhancement produced by the tips.

Bibliography

[1] Craig F. and Bohren, D. R. H. *Absorption and Scattering of Light by Small Particles.* Wiley-VCH Verlag GmbH, 1998.

[2] Juan, L.M., Righini, M. and Quidant, R. *Plasmon nano-optical tweezers.* Nature Photonics 5, 349-356, (2011).

[3] Turkevich, J., Stevenson, P. C. and Hillier, J. *A study of the nucleation and growth processes in the synthesis of colloidal gold.* Discuss. Faraday Soc. 11, 55-75, (1951).

[4] Li, N., Zhao, P., and Astruc, D.*Anisotropic Gold Nanoparticles: Synthesis, Properties, Applications, and Toxicity.* Angew. Chem. Int. Ed. 53, 1756-1789 (2014).

[5] Grzelczak, M., Pérez-Juste, J., Mulvaney, P. and Liz-Marzán, L.M. *Shape control in gold nanoparticle synthesis.* Chem. Soc. Rev. 37, 1783-1791, (2008).

[6] Yuan, H., Fales, A. M., Khoury, C. G., Liu, J. and Vo-Dinh, T. *Spectral characterization and intracellular detection of Surface-Enhanced Raman Scattering (SERS)-encoded plasmonic gold nanostars.* J. Raman Spectrosc. 44, 234-239 (2013).

[7] Kneipp ,K., Moskovits, M., and Kneipp, H. *Surface-Enhanced Raman Scattering.* 103, Springer Berlin Heidelberg, (2006).

[8] Aslan, K., Wu, M.,Lakowicz, J.R. and Geddes, C.D. *Metal Enhanced Fluorescence Solution-based Sensing Platform 2: Fluorescent Core-Shell $Ag@SiO_2$ Nanoballs.* J. Fluoresc. 17, 127-131, (2007).

[9] Mulvaney, P. *Surface Plasmon Spectroscopy of Nanosized Metal Particles.* Langmuir, 12, 788-800, (1996).

[10] Henglein, A. *Physicochemical properties of small metal particles in solution: 'microelectrode' reactions, chemisorption, composite metal particles, and the atom-to-metal transition.* J. Phys. Chem. 97, 5457-5471, (1993).

[11] Le Ru, E.C. and Etchegoin, P.G. *Principles of Surface-Enhanced Raman Spectroscopy and Related Plasmonic Effects.* 1st edition, Elsevier, Amsterdam, (2009).

[12] Maier, S. *Plasmonics: Fundamentals and Applications.* 1st edition,

Springer, New York, (2007).

[13] Zeman, E.J. and Schatz, G.C. *An Accurate Electromagnetic Theory Study of Surface Enhancement Factors for Silver, Gold, Copper, Lithium, Sodium, Aluminum, Gallium, Indium, Zinc, and Cadmium.* J. Phys. Chem., 91, 634-643, (1987).

[14] Ritchie, R.H., Arakawa, E.T., Cowan, J.J. and Hamm, R.N. *Surface-Plasmon Resonance Effect in Grating Diffraction.* Phys. Rev. Lett., 21, 1530, (1968).

[15] Kreibig, U. and Zacharias, P. *Surface Plasma Resonances in Small Spherical Silver and Gold Particles.* Z. fur Phys. A, 231, 128-143 (1970).

[16] Yoshida, K.I., Itoh, T., Tamaru, H., Biju, V., Ishikawa, M. and Ozaki, Y. *Quantitative Evaluation of Electromagnetic Enhancement in Surface-enhanced Resonance Raman Scattering from Plasmonic Properties and Morphologies of Individual Ag Nanostructures.* Phys. Rev.B, 81, 115406, (2010).

[17] Reguera, J., Langer, J., Jiménez de Aberasturi, D. and Liz-Marzán, L.M. *Anisotropic metal nanoparticles for surface enhanced Raman scattering.* Chem. Soc. Rev., Advance Article, (2017).

[18] Murphy, C.J., Sau, T.K.,Gole,A. M., Orendorff, C.J., Gao, J., Gou, L.. Hunyadi, S.E. and Li, T. *Anisotropic Metal Nanoparticles: Synthesis, Assembly, and Optical Applications.* J. Phys. Chem. B 109(29), 13857-13870, (2005).

[19] Cai, W.B., Ren, B., Li, X.Q., She, C.X., Liu, F.M., Cai, X.W. and Tian, Z.Q. *Investigation of surface-enhanced Raman scattering from platinum electrodes using a confocal Raman microscope: dependence of surface roughening pretreatment.* Surf. Sci. 406, 9-22 (1998).

[20] Wang, S., Xi, W.,Cai, F., Zhao, X., Xu, Z., Qian, J. and He, S. *Three-Photon Luminescence of Gold Nanorods and Its Applications for High Contrast Tissue and Deep In Vivo Brain Imaging.* Theranostics, 2015, 5, 251-266.

[21] Scarabelli, L., Grzelczak, M. and Liz-Marzán, L. M. *Tuning Gold Nanorod Synthesis through Prereduction with Salicylic Acid.* Chem. Mater. 25, 4232-4238 (2013).

[22] Kelly, K.L., Coronado, E. and Zhao, L.L. *The Optical Properties of Metal Nanoparticles: The Influence of Size, Shape, and Dielectric Environment.* J. Phys. Chem. B, 107, 668-677, (2003).

[23] Langille, M.R., Personick, M. L,Zhang, J. and Mirkin, C. A. *Defining Rules for the Shape Evolution of Gold Nanoparticles.* J. Am. Chem. Soc., 134, 14542-14554, (2012).

[24] Scarabelli, L., Coronado-Puchau, M.,Giner-Casares, J.J.,

Langer, J. and Liz-Marzán, L.M. *Monodisperse Gold Nanotriangles: Size Control, Large-Scale Self-Assembly, and Performance in Surface-Enhanced Raman Scattering.* ACS Nano, 8 (6), 5833-5842, (2014).

[25] Lim, B. and Xia, Y. *Metal nanocrystals with highly branched morphologies.* Angew.Chem. Int.Ed., 50(1), 76-85, (2011).

[26] Rodríguez-Fernández, J., Pérez-Juste, J.,Mulvaney, P. and Liz-Marzán, L.M. *Spatially-Directed Oxidation of Gold Nano-particles by Au(III)-CTAB Complexes.* J.Phys.Chem.B, 109 , 14257-1426, (2005).

[27] Yuan, H., Khoury, C.G.,Hwang, H. and Vo-Dinh, T. *Gold nanostars: surfactant-free synthesis, 3D modelling, and two-photon photoluminescence imaging.* Nanotechnology 23, 075102, (2012).

[28] Serrano-Montes, A.B. *Gold Nanostars: Synthesis, stabilization and applications as Surface-Enhanced Raman Scattering tags (PHD thesis).* Universidad de Vigo, (2015).

[29] Hao, F., Nehl, C. L., Hafner, J. H. and Nordlander, P. *Plasmon Resonances of a Gold Nanostar.* Nano Lett., 7, 729-732, (2007).

[30] Nikoobakht, B. and El-Sayed, M. A. *Preparation and Growth Mechanism of Gold Nanorods (NRs) Using Seed-Mediated Growth Method.*, Chem. Mater. 15, 1957-1962, (2003).

[31] Nehl, C. L., Liao, H. and Hafner, J. H. *Optical Properties of Star-Shaped Gold Nanoparticles.* Nano Lett. 6, 683-688, (2006).

[32] Sahoo, P., Dharaa, D., Dash, S., Tyagi, A.K., Raj, B.,Chandramohan, C.R. and Srinivasan, M.P. *Surface Optical Modes in Semiconductor Nanowires* Nanotechnology and Nanomaterials: Nanowires - Implementations and Applications, Ed. by Abbass Hashim, (2011).

[33] Fuchs, F. and Kliewer, K.L. *Optical Modes of Vibration in an Ionic Crystal.* Phys. Rev. 140, A2076, (1965).

[34] Wallis, R.F. *Surface phonons: theoretical developments.* Surface Science, 299-300, 612-627, (1994).

[35] Gupta, R., Xiong, Q., Mahan, G.D. and Eklund, P.C. *Surface Optical Phonons in Gallium Phosphide Nanowires.* Nano Letters, 3 (12), 1745-1750, (2003).

[36] Garro, N., Cros, A.,García-Cristóbal, A. and Cantarero, A. *A Handbook of Self Assembled Semiconductor Nanostructures for Novel Devices in Photonics and Electronics - Optical and Vibrational Properties of Self-assembled GaN Quantum Dots.* Eds: Henini, M., Elsevier Science, (2008).

[37] Gadret, E.G., Chiaramonte, T., Cotta, M.A., Iikawa, F. de Lima, M.M. and Cantarero, A. *Optical phonon modes of wurtzite InP.* View

Affiliations Appl. Phys. Lett. 102, 122101, (2013).

[38] Adu, K.W., Xiong, Q., Gutierrez, H.R. Chen, G. and Eklund, P.C. *Raman scattering as a probe of phonon confinement and surface optical modes in semiconducting nanowires.* Applied Physics A, 85:287, (2006).

Conclusions

In this Thesis, Raman spectroscopy has probed to be a very useful technique to study new materials and their properties.
Magnetite nanoparticles of different sizes was studied in order to know their behavior before their gold treatment in the next chapter. Thanks to the observation of the FC-ZFC curves we can say that all nanoparticles were superparamagnetic at room temperature.
Raman spectroscopy has probed to be very helpful to discriminate the different phases of the iron oxides. Raman spectra sometimes are misinterpreted due to the degradation under laser intense illumination so special care is needed to distinguish the different phases.
Hybrid magnetite-gold nanoparticles were studied, as representative cases of different coupling degree between magnetic and plasmonic NP. The Raman experiments confirm that the NP surrounding the plasmonic constituents presents certain SERS effect.
SCO phenomena was observed with Raman spectroscopy. Focused on the changes in the bands, due to the LS-HS state, it was possible to follow this changes with temperature.
In the case of the nonanuclear cluster, due to the small quantity of the sample obtained, Raman spectroscopy and magnetic measurement allowed us to elucidate the probable structure of this cluster. This study was published in Inorganic Chemistry (2016).
Finally, gold nanoparticles, synthesised during my stay in in the group of Bio-Nanoplasmonics led by Prof. Dr. Liz-Marzán in CIC biomaGUNE, Donosti,, were used with SERS purposes with III-V nitrides (GaN, InN and InP) with very good results. Lot of work is still needed but we are very hopeful with this project.
In this Thesis we have tried to dig into possibilities and applications of Raman spectroscopy that rise according to the emergence of new materials. Thus, Raman spectroscopy is appearing an emerging technique to keep in mind whenever we are studying a new nanomaterial.

Resumen en español

Esta tesis está enfocada a la aplicación de la espectroscopía Raman para la caraterización de nuevos materiales y su uso en diversas aplicaciones basadas en la espectroscopía Raman amplificada en superficie (SERS). Como ventaja con respecto a otras técnicas, la espectroscopía Raman puede ofrecer información óptica, estructural, estequiométrica y magnética de los compuestos utilizando únicamente cantidades de muestra muy pequeñas (por debajo de un microgramo). Ésta es la motivación del trabajo aquí descrito, así como la intención de explorar nuevas aplicaciones de las propiedades magnéticas, tales como entrecruzamiento de spin (spin-crossover, SCO) y a través de ellos tener conocimiento del comportamiento dinámico.

Los resultados se tratan en tres áreas diferentes según las propiedades analizadas. Así, el manuscrito está dividido en tres partes: La primera estudia las nanopartículas de magnetita y los sistemas híbridos de oro-magnetita; en la segunda parte se estudian los compuestos SCO [basados en Fe(II)]; para concluir con el estudio de nanohilos semiconductores de los grupos III-V funcionalizados con oro en la tercera parte. El nexo de unión entre las tres partes (bastante diferentes a primera vista) es la utilización de la espectroscopía Raman para su caracterización. De igual manera para cualquier sistema, la superficie y el material a su alrededor está diseñado para aumentar la información extraída de los espectros Raman en un único cristal, NPs aisladas o grupos de NP.

Además de la introducción general de este resumen (o del **Capítulo 1**), podemos encontrar una introducción específica de cada sistema al principio de cada capítulo. De esta manera se tratan los detalles fundamentales y particulares de los diferentes materiales en estudio de manera que resulte más fácil de leer.

En el **Capítulo 2** se presentan los fundamentos y técnicas experimentales. Éste incluye una descripción de cada técnica experimental utilizada. El magnetismo del óxido de hierro está descrito en el **Capítulo 3**. Nos centramos en la magnetita por el enorme potencial de aplicaciones que se le atribuyen a este material. En el **Capítulo 4** se compararon distintas rutas sintéticas en relación con compuestos magneto-plasmónicos basados en heteroestructuras híbridas de oro-magnetita. En resumen, se ha demostrado que la presencia de magnetita mejora las propiedades

ópticas de la estructura híbrida, mientras que los grandes grupos plasmónicos podrían afectar a la respuesta magnética debido al diamagnetismo del oro.

El fenómeno del entrecruzamiento de espín (SCO) se estudió por espectroscopía Raman en el **Capítulo 5**. Merece la pena mencionar la correlación entre los estados de espín y la señal Raman, que permitió identificar estados magnéticos de microscristales y NPs de compuestos de Fe(II). Para reproducir los resultados fiables de caracterizaciones magnéticas en sistemas diluidos, tales como SQUID, no se necesitó más de unos pocos mg. La reducción de la cantidad de material necesario posibilita las aplicaciones de estos compuestos en superficie, donde la transición SCO puede ser monitorizada por Raman localmente.

Por último, el problema de la señal débil que normalmente obtenemos en nanohilos de semiconductores aislados se trata en el **Capítulo 6**. Para ello, los nanohilos se funcionalizaron con nanopartículas de oro de tamaño y forma adecuados. En este capítulo se ofrece un breve resumen de la variedad de nanopartículas de oro disponibles así como algunos detalles de las estrategias de funcionalización empleadas. A continuación, se discute la magnitud del incremento de señal Raman observado. De especial interés son las conclusiones sobre el papel que juega el substrato en el estudio de fonones ópticos en nanohilos aislados.

List of Publications

Delgado, E., Hernández, E., Nievas, A., Martín, A. and Recio, M.J. *Formation of multifunctional ligands by nucleophilic addition of alcohols and thiols to the alkyne groups in compound* $C_5H_5FeC_5H_4C{\equiv}CSC{\equiv}CH$, Journal of Organometallic Chemistry, 695(3), 446-452, (2010).

Mendoza-Pérez, R., Contreras-Puente, G., López-López, M., Santana-Rodríguez, G., Aguilar-Hernández, J.,Hernández-Cruz, E., Campos Rivera, N., Mayahuel, O., Sánchez, V., Cantarero-Sáez, A. and Recio-Carretero, M.J. and Jones, K. , 37th IEEE PHOTOVOLTAIC SPECIALISTS CONFERENCE, Washington (USA, June,19-24, 2011).

Contreras-Puente, G., Cantarero-Sáez, A. and Recio-Carretero, M.J., de Melo, O., Campos Rivera, N., Hernández-Cruz, E., Mendoza-Pérez, R., Santana-Rodríguez, G., Aguilar-Hernández, J., López-López, M. and Zamora, L. *Raman measurements on GaN thin films for PV-purposes.*, 38th IEEE PHOTOVOLTAIC SPECIALISTS CONFERENCE, Austin, Texas (USA, June, 3-8, 2012).

Abhervé, A.*, Recio-Carretero, M.J.*, López-Jordá, M., Clemente-Juan, J. M., Canet-Ferrer, J., Cantarero-Sáez, A., Clemente-León, M. and Coronado, E. *Nonanuclear Spin-Crossover complex containing Iron(II) and Iron (III) based on a 2,6-Bis(pyrazol-1-yl)pyridine Ligand funcionalized with a carboxilate group.*, Inorganic Chemistry, 55(3),9361-9367, (2016).

Agradecimientos

Esta es para mí, la parte más difícil de escribir porque han sido muchas la personas que me han acompañado durante estos años. Para empezar me gustaría agradecer a Andrés la oportunidad de trabajar en su grupo, por ayudarme, enseñarme y estar siempre que he necesitado su ayuda. Agradecer también a Josep que, aunque se incorporó más tarde a este proyecto, ha sido una pieza fundamental del trabajo final, con su lluvia de ideas, su disposición para ayudarme siempre y su impulso constante durante la escritura de la tesis.
Durante estos años muchas personas me ha acompañado en este viaje, primero en el ICMUV y luego en el ICMol y de una u otra forma también han contribuido. Nuria, Ana y Mauricio siempre han estado dispuestos a echarme una mano y guiarme cuando los he necesitado. Jose, Antonio, Víctor y Eleonora que fueron los primeros amigos que tuve en el instituto, con los que he tenido las conversaciones más curiosas y con los que más cafés he tomado. Sandra que ha sido mi compañera y amiga durante éstos años y que seguirá siéndolo por muchos más, BFF. Hemos pasado por muchas cosas juntas en los últimos años y ha sido muy importante que estuvieras ahí. Julián y Pascual, los testigos de Jehová de los almuerzos, que me introdujeron en el mundo del mal a través de los almuerzos de los viernes y que van captando cada vez más adeptos de todos los institutos. También utilizan el truco de la torrá incluyendo a las familia para atraerte más hacia el mal. Muchas gracias por resolver todos mis problemas en el laboratorio con tanta profesionalidad y buen rollo. A mi Carlitos de mis amores porque me has hecho reir más que nadie, por ser tan especial y porque eres un gran hombre en un cuerpo tan pequeñico. A Hannan por enseñarme tanto de su cultura y traerme dulces de su país. A los almorzadores con los que he compartido los mejores almuerzos del Lasmi. Especialmente a Jose Usagre que ha sintetizado las nanopartículas de magnetita y que simepre ha estado dispuesto a echarme una mano y explicarme todas las dudas que he tenido. Ya no tendrás que huir cuando me veas por los pasillos.
No puedo dejar de agradecer a todas las personas que conocí en mi estancia en Donosti, especialmente a Ana, Dorleta y Ada que me acogieron en el grupo y me enseñaron a hacer las nanopartículas de oro y a todo el grupo del biomaGUNE

porque son el grupo más increíble y divertido que he conocido. Gracias enseñarme lo que es un pintxo-pote y por hacerme la estancia tan agradable y especial. Gracias también a Liz-Marzán por darme la increíble oportunidad de hacer una estancia en su grupo.
Un cambio fundamental a mi vida ha sido conocer a las "chungas" que me han acogido en Cullera pese a ser una "madriles". Gracias por cambiar mi vida a mejor.
Las últimas palabras son para mi familia (Gloria, Ana, Santi, Amparo, Fernando, Irene, Angela y Diana) que me apoya siempre, que está conmigo y me acompaña en todo lo que hago. A mi madre por apoyarme y creer en mí siempre y a mi padre porque no pasa un día sin que te eche de menos. Graciela y Elvira también vais en el apartado de familia junto con piapa y miama, porque para mi sois familia. A Luis que me ha acompañado y apoyado en este viaje, de varios años, por Valencia y a Rafa que ha nacido y crecido junto con esta tesis, gracias por existir.
Gracias a toda la gente que me ha compañado durante mis estudios de doctorado y a los expertos que han evaluado la tesis.

M.J. Recio-Carretero
Valencia, septiembre 2017